The Dissertation Committee for Hyung Taek Ahn
certifies that this is the approved version of the following dissertation:

A New Incompressible Navier-Stokes Method with General Hybrid Meshes and Its Application to Flow/Structure Interactions

Committee:

Clinton N. Dawson, Supervisor

Yannis Kallinderis, Supervisor

Graham F. Carey

Ronald O. Stearman

Spyridon A. Kinnas

A New Incompressible Navier-Stokes Method with General Hybrid Meshes and Its Application to Flow/Structure Interactions

by

Hyung Taek Ahn, B.Eng., M.S.

Dissertation

Presented to the Faculty of the Graduate School of

The University of Texas at Austin

in Partial Fulfillment

of the Requirements

for the Degree of

Doctor of Philosophy

The University of Texas at Austin

May 2005

To my parents, Young Ok Ahn and Tae Hwa Noh

Acknowledgments

I would like to express my profound gratitude to my advisor, Professor Yannis Kallinderis, for his advices, comments, and encouragement during my dissertation research. I am also grateful to him for asking questions that helped me consolidating my ideas and giving me considerable freedom to follow my own paths in research. His good sense of humor also has been invaluable to me while I was struggling with research.

I would like to express my sincere appreciation to the members of my dissertation committee. I am extremely indebted to Professor Clinton Dawson, my co-advisor, for his comments and advices about my work as well as hosting me at the Institute of Computational Engineering and Sciences (ICES) and providing the excellent parallel computing resources of the Center for Subsurface Modeling (CSM) at ICES. My heartfelt gratitude must be expressed to Professor Graham Carey for his advices both in academics and life. Prof. Carey brought me a perspective view of my dissertation, and helped me to identify important parts and less important parts. I wish to thank Professor Spyridon Kinnas for giving me a chance to present my work at the Offshore Technology Research Center (OTRC) and reading my dissertation. I would like to thank Professor Ronald Stearman for helpful discussions about aeroelasticity. Also, I wish to thank Professors David Goldstein and Laxminarayan Raja for serving in my oral qualifying exam committee.

I wish to thank my friends and staffs in ASE/EM department, ICES, and

OTRC. My special gratitude has to be expressed to Christos Kavouklis for our friendship. Our late night discussions (sometimes lasting over the weekend) about various topics have always been a pleasure to me. I also like to express my appreciation to the Rotary Foundation, the Rotary International, for their scholarships which actually enabled me to come to the UT for my graduate studies.

I am always thankful to the schools where I studied and the faculty members who built my academic foundations. Especially, I wish to thank Professors Boung-Duk Lim and Joung-Youb Sah at Yeungnam University and Professor Hoon Hur at the Korea Advanced Institute of Science and Technology (KAIST).

Finally, I would like to express my deepest appreciation to my family. I wish to thank my father, mother, and sister for their endless love and support. I would like to thank my fiancée, Mikyung Jung, who stood on my side providing me courage and support.

The present work has been partially supported by the Offshore Technology Research Center and the Minerals Management Service and its Industry Consortium[1], as well as by a Joint Industry Project through the University of Texas at Austin.

HYUNG TAEK AHN

The University of Texas at Austin
May 2005

---

[1] Disclaimer: "The views and conclusions contained in this document are those of the authors and should not be interpreted as representing the opinions or policies of the U.S. Government. Mention of trade names or commercial products does not constitute their endorsement by the U.S. Government".

A New Incompressible Navier-Stokes Method with General Hybrid Meshes and Its Application to Flow/Structure Interactions

Publication No. ____________________

Hyung Taek Ahn, Ph.D.
The University of Texas at Austin, 2005

Supervisors: Clinton N. Dawson, Yannis Kallinderis

A new incompressible Navier-Stokes method is developed for unstructured general hybrid meshes which contain all four types of elements in a single computational domain, namely tetrahedra, pyramids, prisms, and hexahedra. Various types of general hybrid meshes are utilized and appropriate numerical flux computation schemes are presented. The artificial compressibility method with a dual time-stepping scheme is used for the time-accurate solution of the incompressible Navier-Stokes equations. The Spalart-Allmaras turbulence model is also presented in the dual time-stepping form and is solved in a strongly coupled manner with the incompressible Navier-Stokes equations. The developed scheme is applied to the study of the inflow turbulence effect on the hydrodynamic forces exerted on a circular cylinder. In order to accommodate possible structural and mesh motion, the method is extended to the arbitrary Lagrangian-Eulerian (ALE) frame of reference.

The geometric conservation law is satisfied with the proposed ALE scheme in moving mesh simulations. The developed ALE scheme is applied to the vortex induced vibration of a cylinder. A strong coupling of fluid and structure interaction based on the predictor-corrector method is presented. The superior stability property of the strong coupling is demonstrated by a comparison with the weak coupling. Finally, the developed methods are parallelized for distributed memory machines using partitioned general hybrid meshes and an efficient parallel communication scheme to minimize CPU time.

Contents

List of Tables

List of Figures

Chapter 1

Introduction

Numerical solutions for the incompressible Navier-Stokes equations have been of great interest because of their wide range of applications. The incompressible Navier-Stokes equations can be applied to low Mach number aerodynamics, bio-fluid flows, convective heat transfer problems, or hydrodynamics. Even with the high interest in incompressible flows, the incompressibility requirement has always been an obstacle in solving the equations in a straight forward manner. Since there is no time-evolution term in the continuity equation, the standard time marching schemes developed for solving the compressible Navier-Stokes equations cannot be applied directly, and the continuity equation imposes a constraint which the momentum equations have to satisfy.

The main solution approaches for solving the incompressible Navier-Stokes equations can be classified into three main categories as follows [26, 25]

1. stream function-vorticity method
2. pressure-correction method
3. artificial compressibility method

The first category (stream function-vorticity) calculates the values of the stream function and vorticity, and determines the velocity and pressure fields afterwards. The other two categories, pressure correction and artificial compressibility, both use the primitive variables (pressure and velocity) as unknowns but are completely different in formulation.

The vorticity based formulation completely decouples the velocity and pressure calculations. In two-dimensional computations, the governing equations are formulated in terms of a stream function and vorticity [9, 33]. Direct extension of this method to three dimensions is not possible. However, different formulations have been used in three dimensions, such as the vorticity-velocity approach [57], the vector-potential approach [90], and the vector stream function approach [75]. The selection of boundary conditions is quite challenging for these methods.

The second class of algorithms, called the pressure correction method, uses a Poisson equation for the pressure field [27, 60]. The usual computational procedure is to assume an initial pressure field, and then an iterative process is applied until the continuity equation is satisfied. Even though this method has matured and been successfully applied to a variety of applications [10, 79], the solution accuracy and performance is highly dependent on the performance of the pressure Poisson equation solver, and this can be very expensive for time accurate simulations of flows over complex geometries.

The last category of methods, artificial compressibility, proposed by Chorin [13], introduces a pseudo time-derivative of pressure into the continuity equation. This pseudo term changes the mathematical character of the continuity equation from elliptic to hyperbolic, and enables the system of equations to be solved with a variety of time-marching schemes developed for compressible flow solvers.

1.1 The artificial compressibility method

The original form of the artificial compressibility method, introduced by Chorin [13], was presented in a steady state form. The continuity equation is changed by adding an artificial time derivative of pressure, and the true time-derivatives in the momentum equations are also changed to the artificial time-serivatives as follows

$$\frac{1}{\beta}\frac{\partial p}{\partial t^*} + \frac{\partial u_i}{\partial x_i} = 0 \tag{1.1}$$

$$\frac{\partial u_i}{\partial t^*} + \frac{\partial}{\partial x_j}\left(u_i u_j\right) = -\frac{\partial p}{\partial x_i} + \frac{\partial \tau_{ij}}{\partial x_j} \tag{1.2}$$

where t^* indicates the artificial time, and β is called the artificial compressibility parameter due to the anology that may be drawn between the above equations and the equations of metion for compressible fluid whose equation of state is given by $p = \beta\rho$. The parameter β has the dimensions of a velocity squared so $\sqrt{\beta}$ represents an artificial-speed of sound of the transformed system.

The time accurate formulation of the artificial compressibity method can be written as follows

$$\frac{1}{\beta}\frac{\partial p}{\partial t^*} + \frac{\partial u_i}{\partial x_i} = 0 \tag{1.3}$$

$$\frac{\partial u_i}{\partial t^*} + \frac{\partial u_i}{\partial t} + \frac{\partial}{\partial x_j}\left(u_i u_j\right) = -\frac{\partial p}{\partial x_i} + \frac{\partial \tau_{ij}}{\partial x_j} \tag{1.4}$$

As shown in the above equations, in the momentum equations, there are true time-evolution terms as well as the added artificial time-derivative terms. This time accurate formulation was first presented by Peyret [63]. The true time derivatives were discretized by first order backward difference scheme and the system of equations was iterated to the steady state in artificial time. Rogers and Kwak [72, 73, 71] applied the artificial compressibility method to unsteady problems with an implicit line-relaxation procedure using the finite difference method. They first tried a central difference scheme with artificial dissipation [76], and later switched to a higher order upwind scheme based on Roe's flux-difference splitting [71].

Belov [6] first applied Jameson's dual time-stepping scheme [31] to a time accurate formulation of the artificial compressibility method. The dual time-stepping scheme is basically solving a sequence of steady state problems in pseudo-time by using a well established explicit multi-stage scheme. Hence, even if the formulation is implicit in true-time, the actual time advancement is driven by the explicit multi-stage scheme in pseudo-time.

The dual time-stepping time accurate formulation can also be used for the turbulent eddy viscosity transport equation. In a time accurate formulation of RANS (Reynolds-averaged Navier-Stokes) equations, the turbulent model equation should also be in a consistent form with the mean flow (Navier-Stokes) equations. Hence, for the current turbulent flow simulations, the dual time-stepping scheme is also applied to the eddy viscosity transport equation and is solved concurrently with the incompressible Navier-Stokes equations.

The application of the artificial compressibility to the unstructured meshes is relatively recent. Lin [42] applied the dual time-stepping time accurate artificial compressibility method to adaptive unstructured meshes in two dimensions. Anderson [4] applied the artificial compressibility method with Roe's flux-difference splitting scheme on two-dimensional unstructured meshes.

Even with the successful applications of the artificial compressibility method, most of the previous simulations are with structured meshes [63, 72, 73, 6], and applications on unstructured meshes are relatively recent and limited in two dimensions [42, 4]. Furthermore, the applications of the artificial compressibility method on unstructured meshes are only with simplicial elements (triangles in two dimensions, tetrahedra in three dimensions) and no result has been reported yet about general hybrid meshes containing all four types of elements in three dimensions (hexahedra, prisms, pyramids, and tetrahedra), which is one of the major topics of the current research.

1.2 General hybrid meshes

Hybrid meshes refer to unstructured meshes including different types of elements within a single computational domain. For viscous flow simulations, the superiority of the hybrid meshes over the structured or conventional unstructured meshes composed of simplexes (tetrahedra in three dimensions and triangles in two dimensions) only has been advocated by many researchers [34, 36, 35, 89, 64, 80]. This is because hybrid meshes have the merits of good viscous layer capturing ability owed to structured meshes and the flexibility of dealing with complex geometries borrowed from unstructured meshes.

The merits of hybrid meshes can be further enhanced by introducing additional element types (hexahedra and pyramids) into the conventional hybrid meshes, which are composed of only prisms and tetrahedra. We call the meshes consisting of all four types of elements as general hybrid meshes (GHM) as compared to the conventional hybrid meshes.

By locating local hexahedra in the viscous and wake regions where fine mesh resolution is required, the connectivity (the number of edges) can be considerably reduced and this directly leads to saving in overall computational time and memory storage. In addition to the improvement of computational efficiency, local hexahedra can be used in dealing with more complex geometries and in capturing more anisotropic flow features. For example, flows around the leading edge of a wing are pretty much unidirectional, and the gradient of solution is very small in the spanwise direction compared to the normal and tangential directions. For such cases, local hexahedra can be used to capture development of the boundary layer with the minimum computational cost compared to prisms or tetrahedra. Typical examples of conventional and general hybrid meshes used for flow simulation around a circular cylinder are presented in Figures 1.1 and 1.2.

In summary, the extended capabilities by the introduction of general hybrid meshes are:

- more flexibility in dealing with complex geometries
- more flexibility in capturing various anisotropic flow features
- less computational cost compared to conventional tetrahedral meshes or prismatic/tetrahedral hybrid meshes
- less restriction to adaptive mesh refinement

Furthermore, the solution algorithms for general hybrid meshes, presented in this research, are general enough to handle all types of meshes, and those are

- general hybrid meshes with all four kinds of element types
- conventional unstructured meshes
- blocked structured meshes
- meshes with locally refined regions where heterogeneous element types are introduced

The key issue of the general hybrid mesh simulations presented here is how to evaluate the numerical fluxes through the mixture of different cell topologies, which may inhibit the correct evaluation of numerical fluxes. When a mesh includes different types of elements, mesh regularity may be deteriorated more easily. This is especially happening at the interfaces of different types of elements, such as the interfaces between the prismatic or hexahedral layers and tetrahedral or pyramidal

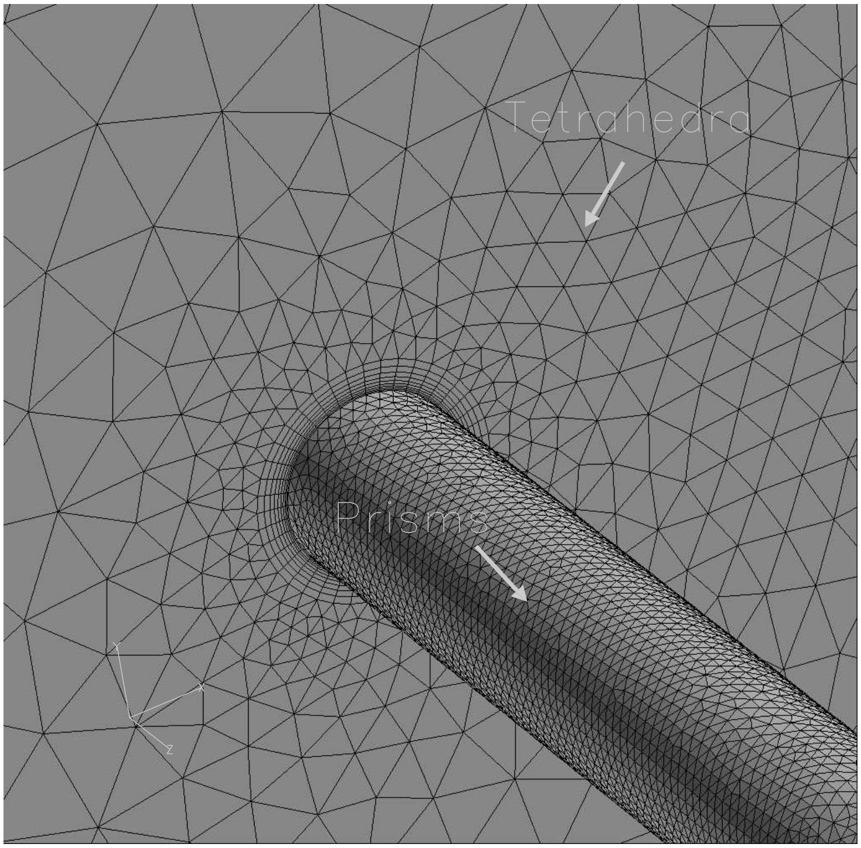

Figure 1.1: A typical example of a conventional hybrid mesh around a circular cylinder. Prisms are located in the viscous region around the cylinder and tetrahedra are used for the rest of computational domain.

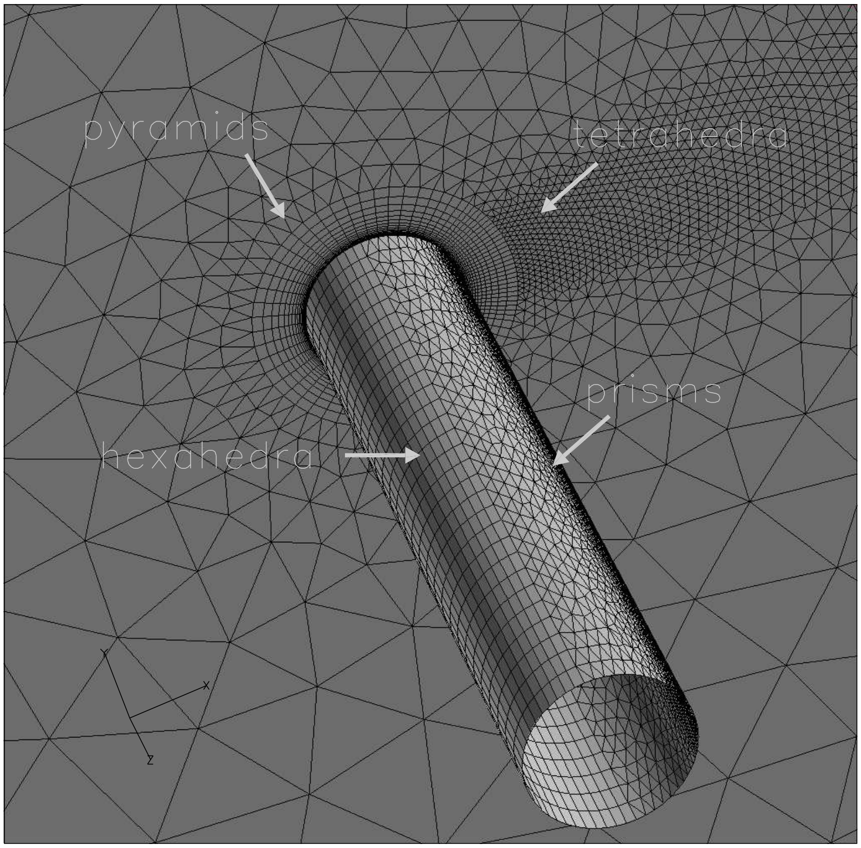

Figure 1.2: A typical example of a general hybrid mesh around a circular cylinder. Hexahedra are located in the frontal half of the viscous region around the cylinder, prisms are located in the rear half of the viscous region around the cylinder, pyramids are used at the interfaces between the hexahedral and tetrahedral region, and tetrahedra are used for the rest of computational domain including the wake region.

regions. Furthermore, the prismatic/hexahedral cells located in the viscous region have typically very high aspect and stretching ratios along the direction normal to the viscous wall. These kinds of mesh irregularity can be further increased by multiple levels of adaptive mesh refinement or mesh deformation. Comparisons between high order upwind schemes and central difference schemes with different artificial dissipation models are presented in terms of solution accuracy as well as computational efficiency on general hybrid meshes.

When the computational grid includes more types of elements, mesh irregularity increases and this may prohibit direct extension of a serial algorithm to a parallel one. A mesh transparent graph partitioning strategy is used as the method of domain partitioning. A grid-transparent mesh data structure which enables parallel inter-processor communications is presented. A single-loop communication algorithm, which does not require any *a priori* communication schedule, is presented for efficient parallel inter-processor communications. The efficiency of the proposed parallelization algorithm is presented with plots of scalability measured on a massively-parallel machine with distributed memory architecture.

1.3 Moving mesh simulations and flow/structure interactions

Moving mesh problems in computational fluid dynamics (CFD) have become of great interest due to their wide area of applications. Blood flow through the arteries or human heart, airfoil oscillation, wing fluttering, free surface flows, and many kinds of flow and structure interaction problems can be classified in this category.

In order to simulate the fluid dynamics problem with moving mesh and boundaries, several approaches have been proposed, such as the arbitrary Lagrangian-Eulerian (ALE) scheme [29], the space-time approach [86, 87], and the immersed boundary method [62, 61, 99].

The ALE formulation is based on the description of the flow field on an arbitrarily moving frame of reference which is typically attached to the moving meshes. Hence, the mesh velocity appears in the convective flux term of the formulation. The space-time approach is based on a finite element formulation of the governing equations which is written over a sequence of space-time slabs. In this formulation, the finite element interpolation polynomials are functions of both space and time. Lastly, in the immersed boundary method, a body in the flow field is considered as a kind of momentum forcing in the Navier-Stokes equations rather than a real body. In the method, the choice of accurate interpolation schemes satisfying the no-slip condition on the immersed body is crucial because the mesh does not generally follows the interface of immersed boundary. Among the aforementioned approaches, the ALE scheme is the most popular method within the CFD community and has been chosen for the current study.

For the stable and accurate ALE solution on moving meshes, the time integration scheme should be developed and verified, such that it preserves the stability and accuracy of its fixed mesh counterpart. Furthermore, the motion of mesh should not deteriorate the stability or accuracy, and should be capable of preserving the uniform flow solution regardless of mesh motion, which the geometric conservation law (GCL) accounts for.

In the development of stable and accurate ALE schemes and identification of the role of GCL in terms of accuracy and stability, there have been considerable research efforts, especially by Farhat's research group [41, 39, 19, 18]. Essentially, the ALE time integration schemes developed by Farhat are based on either time-averaging of fluxes evaluated on different mesh configurations or evaluation of fluxes on a time-averaged mesh configuration [20]. Such schemes present formal second order accuracy with GCL obeying property, but time-averaging among multiple mesh configurations can be a demanding computational task.

A more concise approach has been used by others [79, 43, 11], namely the ALE formulation with a moving mesh source term. Even though such a formulation has produced reasonable results for moving mesh simulations, there was neither a clear derivation of the source term nor discussion of its significance. To be certain about the validity of the ALE formulation with a moving mesh source term, we have to be able to derive it from the original conservation laws, and address its significance in moving mesh simulations. One of the main topics of the moving mesh study is the derivation and validation of the ALE scheme with a moving mesh source term, and its application to flow and structure interaction problems involving mesh motion.

Once a stable and accurate ALE scheme is developed for moving mesh simulations, the developed flow solver has to be coupled with a structural solver. Basically two different coupling methods can be devised, namely weak and strong coupling, depending on how the information is communicated between the two solvers. In weak coupling, the two solvers are lagged by one true time step, but in strong coupling the two different solvers are converged simultaneously. Weak coupling can be a reasonable choice for very small time steps typically employed for explicit time-stepping schemes. However, since an implicit scheme is used for the current flow simulations, the time step is relatively large compared to an explicit scheme, hence the strong coupling method is preferred to the weak coupling. A predictor-corrector method is used for the strong coupling of flow and structural fields.

1.4 Motivation of the present research

Based on the survey about the previous research efforts in hybrid mesh methods for flow simulations and fluid/structure interaction problems, the initial motivations of the current research can be listed as follows.

1. generalization of hybrid meshes
2. a new solution algorithm for utilizing general hybrid meshes
3. more stable and accurate simulation of flow/structure interactions

First of all, the generalization of hybrid meshes for flow simulations was the first goal of this research. The conventional hybrid mesh methods have been investigated for compressible and incompressible Navier-Stokes equations in prior studies by Dr. Kallinderis and his students [59, 53, 78]. The first objective of this research is generalizing the conventional hybrid meshes to general hybrid meshes which utilizing all four types of elements in a single computational domain. The utility and effectiveness of general hybrid meshes for flow simulations had not been reported and was needed to be investigated in the present research.

Second, a new solution algorithm for utilizing general hybrid meshes was needed to be investigated. By the nature of severe mixing of element types in general hybrid meshes, the solution algorithm should be more robust and accurate than that of structured or simple unstructured meshes. A pressure-correction type method has been used for incompressible Navier-Stokes equations [78]. This method was shown to give reasonable results for incompressible Navier-Stokes solutions. However, the performance of the solution algorithm is highly depends on the pressure-Poisson solver, which can be expensive for large scale problems with complex geometries. Therefore, a new solution method (with parallel execution capability) for incompressible Navier-Stokes equations is needed in order to utilize the general hybrid meshes.

Third, a more stable and accurate solution algorithm for flow/structure interactions on hybrid meshes was needed. In the past, pressure-correction type incompressible Navier-Stokes method was applied to the flow/structure interaction problems with hybrid meshes [78, 79]. In their work, the structure is modeled with rigid body, and no relative motion in the computational mesh was allowed. The coupling method between the fluidic and structural solver was also in a weak manner which may be called weak(loose)-coupling. In the weak coupling, the interaction can be unstable as time step becomes large. Hence, a more stable and accurate solution algorithm is needed which possibly incorporating flexible structural model with mesh motion and strong coupling between the structural and fluidic solvers.

1.5 Contributions of the current research

The main research contributions made in this dissertation can be classified into two parts; first the development of an incompressible Navier-Stokes equations solver for general hybrid meshes, and second its application to moving mesh simulations of flow/structure interactions.

1.5.1 A new incompressible Navier-Stokes method for general hybrid meshes

In the first part of the development of the incompressible Navier-Stokes method, the original contributions of the current research can be listed as follows

1. first introduction of general hybrid meshes to incompressible flow simulations
2. first application of the artificial compressibility method with hybrid meshes
3. a computationally efficient *face-and-edge* algorithm for viscous flux computations
4. inflow turbulence effect study by using the developed solution algorithm
5. parallelization of the solution algorithm on general hybrid meshes

General hybrid meshes are first introduced for simulations of the incompressible Navier-Stokes equations. There have been a few trials of conventional hybrid meshes (prismatic/tetrahedral) for flow simulations [79, 10], but no general hybrid meshes have been utilized so far. In this research, the various kinds of general hybrid meshes are introduced and they are used for the investigation of more accurate and effective flow solution algorithms. The method of artificial compressibility is used for solving the incompressible Navier-Stokes equations on general hybrid meshes, which is also the first application of the method to the hybrid meshes.

A new grid transparent algorithm is presented which is well suited for general hybrid meshes. Especially for the viscous flux computations, a computationally efficient *face-and-edge* algorithm is presented. This face-and-edge algorithm is composed of a first loop of face-wise operations for the surface integrals over edge-duals, and a second loop of edge-wise computations of velocity gradients and viscous fluxes.

A dual time-stepping backward difference scheme is used for the time accurate formulation of the artificial compressibility method, and is also applied to the turbulence equation so that the two sets of equations (incompressible Navier-Stokes equations and turbulence equation) are solved in a strongly coupled fashion. As an application study of the developed solution method, the effect of inflow turbulence on the hydrodynamic forces on a cylinder is investigated. A two-dimensional local mesh refinement study is also performed to identify the effect of local mesh resolution in capturing the inflow turbulent eddies. Lastly, the proposed algorithm is parallelized on a distributed memory system by using message passing interface (MPI) library functions.

1.5.2 Geometrically conservative ALE scheme for flow/structure interactions

In the second part of this research, the developed solution algorithm is further extended to moving mesh simulations, and the original contributions are as follows

1. derivation of a geometrically conservative finite volume ALE scheme
2. presentation of the temporal accuracy of the proposed ALE scheme
3. presentation of the strong coupling of flow/structure interaction based on a predictor-corrector method

An ALE finite volume formulation with a moving mesh source term is derived from the original conservation laws and the geometric conservation law. The significance of moving mesh source is emphasized by presenting the moving mesh source effect on moving mesh simulations in terms of the uniform flow preserving capability. In order to be sure about the temporal accuracy of the proposed ALE scheme, a time step refinement study is performed and its order of accuracy is confirmed on moving mesh configurations by comparisons with a reference solution.

Furthermore, the ALE scheme is applied to the vortex induced vibration (VIV) of a flexible cylinder. Beam elements are used for modeling the flexural vibration of the cylinder, and then the equation of motion for the cylinder is nondimensionalized by using the same reference parameters as those of the flow governing equations. The superior stability of strong coupling as opposed to weak coupling is emphasized by a comparison between the two coupling methods.

1.6 Overview

The outline of the dissertation is as follows; in chapter 2, the governing equations for fluid flow are introduced and the turbulent eddy transport equation is also presented.

In chapter 3, the discretization and numerical integration schemes are discussed. In chapter 4, a two-dimensional verification and validation study is presented. A simple error analysis on a uniformly stretched mesh is investigated in one dimension. In chapter 5, the inflow turbulence effect is studied by using the developed and validated flow solution algorithms of the previous chapters. In chapter 6, three-dimensional verification and validation study is presented. Flows around a sphere and a cylinder are simulated for various orders of Reynolds number; $Re = 10 \sim 1,000,000$. The transition of the boundary layer from laminar to turbulent is predicted by using a one-equation turbulence model.

In chapter 7, the equation of motion for a vibrating cylinder is presented. It is nondimensionalized by using the same reference parameters as those for the flow governing equations. Two different coupling methods are discussed for the flow/structure interaction simulations; weak coupling and strong coupling. The improved stability of strong coupling is emphasized by a comparison between the two methods. In chapter 8, the verification study of the presented ALE scheme is carried out. Lastly, the presented moving mesh method is applied to the vortex induced vibration of a cylinder. The result of the current simulation is compared with other computational results in literature.

In chapter 9, a parallelization of the proposed numerical scheme is introduced. Different domain partitioning schemes are discussed. A mesh-transparent interprocessor communication algorithm is presented. Scalability of the implemented parallel algorithm is also demonstrated.

In chapter 10, the last chapter, results of the current research and their significance are summarized. Finally, recommendations for future investigations and research efforts are made.

Chapter 2

Governing Equations

In this chapter, the incompressible Navier-Stokes equations in an arbitrary Lagrangian Eulerian (ALE) frame of reference are derived from the conservation laws for an arbitrarily moving control volume using Reynolds' transport theorem. A moving mesh source term is derived from the physical conservation laws and the geometric conservation law. The significance of the moving mesh source term and its relation to the geometric conservative property are discussed. The governing equations are nondimensionalized by using free stream flow qunatities and the characteristic length scale. A time accurate artificial compressibility method is introduced for unsteady simulation of incompressible viscous flow. The Spalart-Allmaras eddy viscosity transport equation is introduced for turbulence modeling, and its time-accurate formulation is presented in a consistent form with that of the mean flow equations.

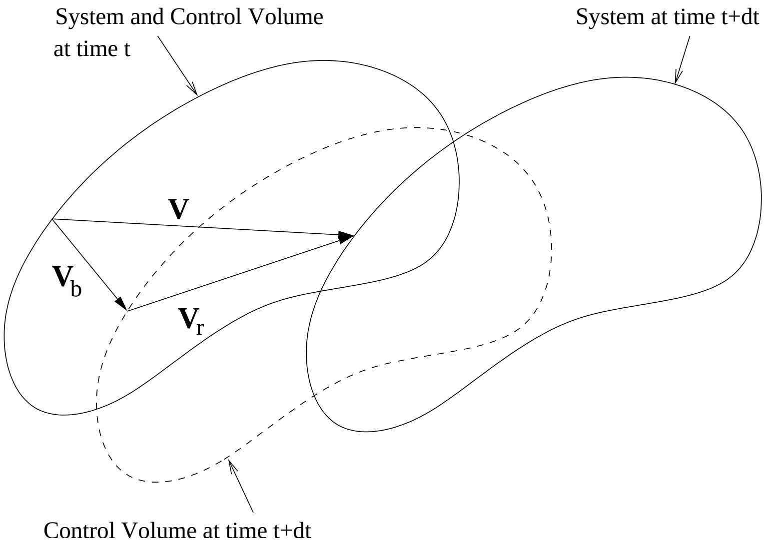

Figure 2.1: Deforming control volume

2.1 Reynolds' Transport Theorem

In order to express the conservation laws for a control volume, a conversion rule needs to be introduced between time derivatives of a system (material or fluid) to time derivatives of the control volume. The system, often called the control mass, is defined as an arbitrary quantity of mass of fixed identity. Everything external to this system is term the surroundings, and the system is separated from its surroundings by its boundaries.

In order to express the conservation laws for a control volume (the control volume may be moving and deforming), we need a conversion relation transforming the system analysis to the control volume analysis. Reynolds' transport theorem relates the time derivatives of a system to the time derivatives of a control volume. Let B be any property of fluid (mass, momentum or energy), and let $\beta = dB/dm$ be the intensive value of B. Those two are related by

$$B_{CV} = \int\limits_{V(t)} \beta\rho dV$$

where the subscript CV stands for the control volume V. Applying the Reynolds' transport theorem to an arbitrarily moving and deforming control volume yields

$$\frac{d}{dt}\left(B_{system}\right) = \frac{d}{dt}\int\limits_{V(t)} \beta\rho dV + \oint\limits_{S(t)} \beta\rho\left(\mathbf{V}_r \cdot \mathbf{n}\right) dS \tag{2.1}$$

Here $\mathbf{V}_r$ is the relative velocity of fluid with respect to the boundary surface of the arbitrarily moving and deforming control volume, and is defined as follows

$$\mathbf{V}_r\left(\mathbf{x}, t\right) = \mathbf{V}\left(\mathbf{x}, t\right) - \mathbf{V}_b\left(\mathbf{x}, t\right)$$

where $\mathbf{V}$ is absolute velocity of fluid and $\mathbf{V}_b$ is absolute velocity of control volume boundary. The Lagrangian description corresponds to the case $\mathbf{V}_r = 0$, and the Eulerian description corresponds to the case $\mathbf{V}_r = \mathbf{V}$. The arbitrary Eulerian-Lagrangian (ALE) description corresponds to a situation between the two extreme cases, such as that of an arbitrarily moving and deforming control volume with $\mathbf{V}_r \neq 0$ and $\mathbf{V}_b \neq 0$.

The time derivative of the first term on the right hand side (RHS) of equation 2.1 is outside of the volume integral. Hence, when the control volume deforms, the time derivative for the deforming control volume integral is not necessarily zero even with a uniform steady flow field.

2.2 Conservation of Mass

By using Reynolds' transport theorem, the law of mass conservation can be derived as follows. In equation (2.1), the property of interest is mass. Hence $B = m$ and the intensive property of mass is $\beta = 1$. Since mass is neither generated nor destructed, we have

$$\frac{dm_{sys}}{dt} = 0$$

and the final form of the mass conservation law for an arbitrarily moving control volume can be expressed as follows

$$\frac{d}{dt} \int\limits_{V(t)} \rho dV + \oint\limits_{S(t)} \rho \left(\mathbf{V} - \mathbf{V}_b \right) \cdot \hat{\mathbf{n}} dS = 0 \tag{2.2}$$

where ρ is fluid density, $\mathbf{V}$ is fluid velocity and $\mathbf{V}_b$ is the velocity of the control volume boundary. If $\mathbf{V}$ is equal to $\mathbf{V}_b$, the flux term vanishes and the formulation becomes identical with that of the Lagrangian frame of reference.

2.3 Conservation of Momentum

In a similar fashion, the conservation of momentum equations may be derived by an application of Reynolds' transport theorem. In this case, the property of interest is linear momentum $B = m\mathbf{V}$ and the intensive property of linear momentum is $\beta = \mathbf{V}$. The rate of change of linear momentum is equal to the sum of external forces

$$\frac{d}{dt} \left(m\mathbf{V} \right)_{sys} = \sum \mathbf{F} = \oint\limits_{S(t)} \sigma \cdot \hat{\mathbf{n}} dS + \int\limits_{V(t)} \rho \mathbf{f} dV$$

Substituting the above relations in Reynolds' transport theorem, the law of momentum conservation for an arbitrarily moving control volume is derived as follows

$$\frac{d}{dt}\int\limits_{V(t)} \rho \mathbf{V} dV + \oint\limits_{S(t)} \rho \mathbf{V}\left(\mathbf{V} - \mathbf{V}_b\right) \cdot \hat{\mathbf{n}} dS = \oint\limits_{S(t)} \sigma \cdot \hat{\mathbf{n}} dS + \int\limits_{V(t)} \rho \mathbf{f} dV \tag{2.3}$$

The two terms on the RHS of equation (2.3) represent surface and body forces respectively, which are acting on the material contained within the control volume V. The stress tensor σ is composed of a normal stress part representing hydrostatic pressure and a shear stress part, and is defined by

$$\sigma_{ij} = -p\delta_{ij} + \tau_{ij}$$

where p is the pressure, τ_{ij} is the shear stress tensor, and δ_{ij} is the Kronecker delta. For Newtonian fluids, the shear stress is linearly related to the rate of strain (deformation) tensor, and is expressed by

$$\tau_{ij} = \lambda \delta_{ij} \frac{\partial u_k}{\partial x_k} + \mu \left(\frac{\partial u_i}{\partial x_j} + \frac{\partial u_j}{\partial x_i} \right)$$

where λ is the coefficient of bulk viscosity and μ is the coefficient of molecular viscosity. For incompressible flows, density is constant everywhere regardless of the pressure field. For those kinds of flows, the first term of the shear stress tensor vanishes because of the continuity equation, and the shear stress tensor reduces to the following form

$$\tau_{ij} = \mu \left(\frac{\partial u_i}{\partial x_j} + \frac{\partial u_j}{\partial x_i} \right)$$

2.4 Incompressible Navier-Stokes Equations

The incompressible Navier-Stokes equations without a body force term are expressed in integral form. The continuity equation and the three momentum equations are expressed in conservative form as follows

$$\frac{d}{dt}\int\limits_V \mathbf{U}dV + \oint\limits_S \left(\mathbf{F}_I\hat{\mathbf{i}} + \mathbf{G}_I\hat{\mathbf{j}} + \mathbf{H}_I\hat{\mathbf{k}}\right)\cdot\hat{\mathbf{n}}dS = \oint\limits_S \left(\mathbf{F}_V\hat{\mathbf{i}} + \mathbf{G}_V\hat{\mathbf{j}} + \mathbf{H}_V\hat{\mathbf{k}}\right)\cdot\hat{\mathbf{n}}dS \quad (2.4)$$

where $\mathbf{U}$ is the vector of conserved flow properties, $\mathbf{F}_I\hat{\mathbf{i}} + \mathbf{G}_I\hat{\mathbf{j}} + \mathbf{H}_I\hat{\mathbf{k}}$ is the convective flux vector, $\mathbf{F}_V\hat{\mathbf{i}} + \mathbf{G}_V\hat{\mathbf{j}} + \mathbf{H}_V\hat{\mathbf{k}}$ is the viscous flux vector, and $\hat{\mathbf{n}}$ is the outward unit normal vector to the boundary of control volume V. By the definition of incompressible flows, the density ρ is a constant and can be factored out of the equations.

Each vector used in equation (2.4) is expressed as follows

$$\mathbf{U} = \left\{\begin{array}{c} 1 \\ u \\ v \\ w \end{array}\right\}$$

$$\mathbf{F}_I = \left\{\begin{array}{c} (u-u_b) \\ u(u-u_b)+p/\rho \\ v(u-u_b) \\ w(u-u_b) \end{array}\right\}$$

$$\mathbf{G}_I = \left\{\begin{array}{c} (v-v_b) \\ u(v-v_b) \\ v(v-v_b)+p/\rho \\ w(v-v_b) \end{array}\right\}$$

$$\mathbf{H}_I = \left\{\begin{array}{c} (w-w_b) \\ u(w-w_b) \\ v(w-w_b) \\ w(w-w_b)+p/\rho \end{array}\right\}$$

where the u , v, and w are velocity components of fluid particles and u_b , v_b, and w_b are velocity components of the control volume boundary.

The viscous fluxes are expressed as follows

$$\mathbf{F}_V = \left\{ \begin{array}{c} 0 \\ \tau_{11} \\ \tau_{12} \\ \tau_{13} \end{array} \right\}$$

$$\mathbf{G}_V = \left\{ \begin{array}{c} 0 \\ \tau_{21} \\ \tau_{22} \\ \tau_{23} \end{array} \right\}$$

$$\mathbf{H}_V = \left\{ \begin{array}{c} 0 \\ \tau_{31} \\ \tau_{32} \\ \tau_{33} \end{array} \right\}$$

For a Newtonian fluid, the shear stress tensor is expressed as

$$\tau_{ij} = \nu \left(\frac{\partial u_i}{\partial x_j} + \frac{\partial u_j}{\partial x_i} \right)$$

where $\nu = \mu/\rho$ is the kinematic viscosity.

2.5 Nondimensionalization

The incompressible Navier-Stokes equations are nondimensionalized by using the following relations.

$$x^* = \frac{x}{D}$$

$$u^* = \frac{u}{U_\infty}$$

$$t^* = \frac{t}{D/U_\infty}$$

$$p^* = \frac{p - p_\infty}{\rho U_\infty^2}$$

where D is the characteristic length scale which is the diameter of the cylinder, U_∞ is the free stream velocity, and p_∞ is the free stream pressure. Substituting all of the above relations into equation (2.4), rearranging terms and dropping the superscript $*$ yields the nondimensional form of the incompressible Navier-Stokes equations. Each component of vectors in nondimensional form is defined as follows

$$U = \left\{ \begin{array}{c} 1 \\ u \\ v \\ w \end{array} \right\}$$

$$\mathbf{F}_I = \left\{ \begin{array}{c} (u - u_b) \\ u(u - u_b) + p \\ v(u - u_b) \\ w(u - u_b) \end{array} \right\}$$

$$\mathbf{G}_I = \left\{ \begin{array}{c} (v - v_b) \\ u(v - v_b) \\ v(v - v_b) + p \\ w(v - v_b) \end{array} \right\}$$

$$\mathbf{H}_I = \left\{ \begin{array}{c} (w - w_b) \\ u(w - w_b) \\ v(w - w_b) \\ w(w - w_b) + p \end{array} \right\}$$

$$\mathbf{F}_V = \frac{1}{\mathrm{Re}} \left\{ \begin{array}{c} 0 \\ 2\frac{\partial u}{\partial x} \\ \frac{\partial u}{\partial y} + \frac{\partial v}{\partial x} \\ \frac{\partial u}{\partial z} + \frac{\partial w}{\partial x} \end{array} \right\}$$

$$\mathbf{G}_V = \frac{1}{\mathrm{Re}} \left\{ \begin{array}{c} 0 \\ \frac{\partial v}{\partial x} + \frac{\partial u}{\partial y} \\ 2\frac{\partial v}{\partial y} \\ \frac{\partial v}{\partial z} + \frac{\partial w}{\partial y} \end{array} \right\}$$

$$\mathbf{H}_V = \frac{1}{\mathrm{Re}} \left\{ \begin{array}{c} 0 \\ \frac{\partial w}{\partial x} + \frac{\partial u}{\partial z} \\ \frac{\partial w}{\partial y} + \frac{\partial v}{\partial z} \\ 2\frac{\partial w}{\partial z} \end{array} \right\}$$

where $\mathrm{Re} = \nu/(U_\infty D)$ is the Reynolds number which is the only control parameter of the flow for a given geometrical shape of the boundary.

2.6 Geometric conservation law and the moving mesh source term

At first proposed by Thomas and Lombard [88], the geometric conservation law (GCL) has been a property that an ALE scheme should obey. The GCL requires that a uniform flow solution should be preserved regardless of mesh motion. The GCL can be directly derived from the continuity equation, equation (2.2), by considering an incompressible uniform flow, *i.e.* a constant density ($\rho = \rho_\infty$) and constant velocity ($\mathbf{V} = \mathbf{V}_\infty$) everywhere. Then the continuity equation reduces to the geometric conservation law

$$\frac{d}{dt}\int\limits_V dV = \oint\limits_S \mathbf{V_b} \cdot \hat{\mathbf{n}} \mathbf{dS} \tag{2.5}$$

As seen in Eq. (2.5), the GCL states purely kinematic relations, namely the instantaneous rate of change of control volume is the rate of volume swept by S.

The system of conservation laws in Eq. (2.4) can be rewritten as below

$$\frac{d}{dt}\int\limits_V \mathbf{U} dV + \mathbf{R}\left(\mathbf{Q}, \mathbf{x}, \dot{\mathbf{x}}\right) = 0 \tag{2.6}$$

where $\mathbf{x}$ and $\dot{\mathbf{x}}$ are time varying position and velocity vectors of the mesh points. $\mathbf{Q}$ is the vector containing primitive variables, which are pressure and velocities, and $\mathbf{R}(\mathbf{Q}, \mathbf{x}, \dot{\mathbf{x}})$ represents the residual of the system of equations, and is defined as follows

$$\begin{aligned} \mathbf{R}(\mathbf{Q}, \mathbf{x}, \dot{\mathbf{x}}) = \quad & \oint\limits_S \left(\mathbf{F}_I \hat{\mathbf{i}} + \mathbf{G}_I \hat{\mathbf{j}} + \mathbf{H}_I \hat{\mathbf{k}}\right) \cdot \hat{\mathbf{n}} dS \\ & - \oint\limits_S \left(\mathbf{F}_V \hat{\mathbf{i}} + \mathbf{G}_V \hat{\mathbf{j}} + \mathbf{H}_V \hat{\mathbf{k}}\right) \cdot \hat{\mathbf{n}} dS \end{aligned} \tag{2.7}$$

The system of equations in equation (2.6) may be rewritten as

$$\frac{d}{dt}\left(\bar{\mathbf{U}} V\right) + \mathbf{R}\left(\mathbf{Q}, \mathbf{x}, \dot{\mathbf{x}}\right) = 0 \tag{2.8}$$

by using the control volume averaged conserved variables defined by

$$\bar{\mathbf{U}} = \frac{1}{V}\int\limits_V \mathbf{U} dV$$

Since the control volume $\mathbf{V}(t)$ and volume-averaged conserved variables $\bar{\mathbf{U}}(t)$ are smoothly varying with respect to time, the unsteady term in Eq. (2.8) can be expanded as

$$\frac{d\bar{\mathbf{U}}}{dt}V + \frac{dV}{dt}\bar{\mathbf{U}} + \mathbf{R}\left(\mathbf{Q}, \mathbf{x}, \dot{\mathbf{x}}\right) = 0 \tag{2.9}$$

Finally, the time derivative of the control volume in Eq. (2.9) can be replaced with a surface integral of control volume boundary velocity by the GCL as shown in Eq. (2.5) to obtain:

$$\frac{d\bar{\mathbf{U}}}{dt}V + \mathbf{R}\left(\mathbf{Q}, \mathbf{x}, \dot{\mathbf{x}}\right) = -\bar{\mathbf{U}}\oint_{S} \mathbf{V_b} \cdot \hat{\mathbf{n}} dS \tag{2.10}$$

We note that since the moving mesh source term is directly derived from the GCL, the system of conservation laws presented in Eq. (2.10) is inherently equipped with the GCL. Hence, the uniform flow is preserved regardless of the mesh motion, and the GCL is always satisfied.

2.7 Time-accurate formulation of the artificial compressibility method

The incompressible Navier-Stokes equations are being solved with the method of artificial compressibility. The artificial compressibility method is presented as a time-accurate formulation by using the dual time-stepping scheme of Jameson [31]. The original form of the artificial compressibility method introduced by Chorin [13] was for steady-state problems where no true time-derivative terms appear the formulation. The time accurate artificial compressibility formulation in the present work has been presented by Belov [6] by using the dual time-stepping algorithm of Jameson.

In the current time-accurate formulation, a pseudo time-derivative of pressure is added to the continuity equation and pseudo time-derivatives of velocity components are added to the momentum equations. As a result, the continuity equation has a pseudo time-derivative and the momentum equations have both true and pseudo time-derivatives.

The system of conservation laws with the added pseudo-term can be expressed as

$$\mathbf{P}\frac{d}{dt^*}\int\limits_V \mathbf{Q}dV + \mathbf{R}^*\left(\mathbf{Q},\mathbf{x},\dot{\mathbf{x}}\right) = 0 \tag{2.11}$$

where the vector $\mathbf{Q}$ contains the primitive variables which are the unknowns of the system of equations, and $\mathbf{P}$ is a diagonal matrix containing the artificial compressibility parameter β acting as a pre-conditioner for the continuity equation

$$\mathbf{P} = \begin{bmatrix} 1/\beta & 0 & 0 & 0 \\ 0 & 1 & 0 & 0 \\ 0 & 0 & 1 & 0 \\ 0 & 0 & 0 & 1 \end{bmatrix}$$

$$\mathbf{Q} = \begin{Bmatrix} p \\ u \\ v \\ w \end{Bmatrix}$$

The vector $\mathbf{R}^*(\mathbf{Q},\mathbf{x},\dot{\mathbf{x}})$ is a semi-discretized unsteady residual which includes the true time-derivative residual $\mathbf{R}\left(\mathbf{Q},\mathbf{x},\dot{\mathbf{x}}\right)$, and the moving mesh source term $\mathbf{S}\left(\mathbf{Q},\mathbf{x},\dot{\mathbf{x}}\right)$, and is given by

$$\mathbf{R}^*\left(\mathbf{Q},\mathbf{x},\dot{\mathbf{x}}\right) = \left[\frac{d\bar{\mathbf{U}}}{dt}V\right]^{n+1} + \mathbf{R}\left(\mathbf{Q},\mathbf{x},\dot{\mathbf{x}}\right) - \mathbf{S}\left(\mathbf{Q},\mathbf{x},\dot{\mathbf{x}}\right) \tag{2.12}$$

where the discretized true time-derivative by using the second order backward difference formula at time step $(n+1)$ is defined by

$$\left[\frac{d\bar{\mathbf{U}}}{dt}V\right]^{n+1} = \left(\frac{3\bar{\mathbf{U}}^{n+1} - 4\bar{\mathbf{U}}^{n} + \bar{\mathbf{U}}^{n-1}}{2\Delta t}\right)V^{n+1}$$

In a similar way, the velocity of control volume (mesh) can also be approximated as follows

$$[\dot{\mathbf{x}}]^{n+1} = \frac{3\mathbf{x}^{n+1} - 4\mathbf{x}^{n} + \mathbf{x}^{n-1}}{2\Delta t}$$

and the moving mesh source term is defined as follows

$$\mathbf{S}\left(\mathbf{Q}, \mathbf{x}, \dot{\mathbf{x}}\right) = -\bar{\mathbf{U}} \int\limits_{S} \mathbf{V}_b \cdot \mathbf{n} dS$$

Since t^* in equation (2.11) refers to the fictitious time during the pseudo-transient state and the moving control volume $V = V(t)$ is a function only of the true time, the pseudo time-derivative can be moved inside of the volume integral. Once the unsteady residual $\mathbf{R}^*$ is constructed, the following steady-state problem in pseudo-time

$$\frac{d}{dt^*}\left(\mathbf{Q}^{n+1,k}\right)V^{n+1} + \mathbf{P}^{-1}\mathbf{R}^*\left(\mathbf{Q}^{n+1,k}, \mathbf{x}^{n+1}, \dot{\mathbf{x}}^{n+1}\right) = 0 \qquad (2.13)$$

is to be solved for the steady state in pseudo-time by using an iterative scheme. The index k in equation (2.13) refers to the number of interations in pseudo time. For each true time step, a steady state problem in pseudo time is solved by an explicit multistage scheme. The iteration in pseudo time is referred to as the sub-iteration as opposed to the time-stepping in true time. Hence, the time advancement requires dual time-stepping, which involves the solution of a steady-state problem in pseudo time for each true time step. A more detailed description of the dual time-stepping scheme is intoduced later in a separate section.

The artificial compressibility parameter β controls the speed of artificial pressure waves and it also affects the overall convergence rate. Depending on the preconditioning method employed, more complicated preconditioning matrices including the variable β can be used [22, 12, 44, 45, 56, 68, 91, 92, 93, 94]. For the current study, a simple diagonal preconditioning matrix with a constant β in the order of $O(100)$ is used.

2.8 Reynolds Averaged Navier-Stokes Equations

In order to express the Reynolds Averaged Navier-Stokes Equations in differential form, let us rewrite the incompressible Navier-Stokes equations in differential form. Applying the divergence theorem and letting the control volume shrink to zero yields the incompressible Navier-Stokes equations in differential form

$$\frac{\partial u_i}{\partial x_i} = 0 \tag{2.14}$$

$$\rho \frac{\partial u_i}{\partial t} + \rho \frac{\partial}{\partial x_j}\left(u_j u_i\right) = -\frac{\partial p}{\partial x_i} + \frac{\partial}{\partial x_j}\left[2\mu\left(\frac{\partial u_i}{\partial x_j} + \frac{\partial u_i}{\partial x_j}\right)\right] \tag{2.15}$$

Next, we decompose the instantaneous velocity $u_i(\mathbf{x}, t)$ into the mean velocity $U_i(\mathbf{x})$ and the fluctuation $u_i'(\mathbf{x}, t)$, that is

$$u_i(\mathbf{x}, t) = U_i(\mathbf{x}) + u_i'(\mathbf{x}, t) \tag{2.16}$$

where the mean velocity is defined as

$$U_i(\mathbf{x}) = \lim_{T \to \infty} \frac{1}{T} \int_0^T u_i(\mathbf{x}, t) dt.$$

By substituting equation (2.16) in equations (2.14) and (2.15), and time (ensemble) averaging the incompressible Navier-Stokes equations yields the Reynolds averaged Navier-Stokes (RANS) equations

$$\frac{\partial U_i}{\partial x_i} = 0$$

$$\rho \frac{\partial U_i}{\partial t} + \rho \frac{\partial}{\partial x_j} (U_j U_i) = -\frac{\partial p}{\partial x_i} + \frac{\partial}{\partial x_j} \left(2\mu S_{ij} - \rho \overline{u'_j u'_i} \right)$$

where $S_{ij} = (\partial U_i / \partial x_j + \partial U_j / \partial x_i)$ is strain rate tensor of mean velocity.

The correlation term of fluctuations $\rho \overline{u'_i u'_j}$ is known as the Reynolds stress tensor. The Reynolds stresses represent the time-averaged rate of momentum transfer due to turbulence, whereas the viscous stresses $2\mu S_{ij}$ stem from the momentum transfer at the molecular level.

2.9 Eddy Viscosity Hypothesis

In the RANS equations, six additional unknowns of Reynolds stresses are introduced in addition to the four unknowns of mean flow variables p , u , v , and w. The total number of unknowns is ten and the number of equations is only four, therefore the RANS equations are not closed and cannot be solved unless the Reynolds stresses are determined by introducing further approximations or additional equations. The Reynolds stress tensor can be dramatically simplified by using the turbulent-viscosity hypothesis (also known as the Boussinesq approximation)

$$-\rho \overline{u'_i u'_j} + \frac{2}{3} \rho k \delta_{ij} = 2\rho \nu_t S_{ij}$$

where k is turbulent kinetic energy and S_{ij} is strain rate tensor of mean flow velocities. In the current study of turbulent flow simulations, the Spalart-Allmaras one-equation model is employed. Compared with a two-equation turbulence model, the turbulent kinetic energy term is neglected, and the (kinematic) eddy viscosity ν_t , the only additional unknown from Reynolds averaging, is being determined by solving the eddy-viscosity transport equation

$$-\rho\overline{u_i'u_j'} = 2\rho\nu_t S_{ij}$$

Substituting the eddy viscosity relation into the RANS equations yields the momentum equations expressed in the following form

$$\frac{\partial U_i}{\partial t} + \frac{\partial}{\partial x_j}\left(U_j U_i\right) = -\frac{1}{\rho}\frac{\partial p}{\partial x_i} + \frac{\partial}{\partial x_j}\left[(\nu + \nu_t)\left(\frac{\partial u_i}{\partial x_j} + \frac{\partial u_j}{\partial x_i}\right)\right]$$

The only difference from the original incompressible Navier-Stokes equations is the appearance of eddy viscosity in the viscous flux term. If the eddy viscosity ν_t vanishes, the original incompressible Navier-Stokes equations are recovered. Now the system of equations is composed of the continuity equation, the three momentum equations, and the eddy viscosity transport equation. The unknowns are the four primitive variables (p, u, v, w) and the turbulent eddy viscosity (ν_t), hence the system of equations is closed and solvable.

2.10 Spalart-Allmaras Turbulence Model

Spalart and Allmaras [81] introduced a one-equation model originally developed for aerodynamic flow. A single model transport equation is solved for the turbulent viscosity (ν_t) and it has been shown that the model is quite successful especially for drag prediction in aerodynamic applications [24].

In addition, the model has several attractive features compared to algebraic (e.g. Baldwin-Lomax) and two-equation (e.g. $k - \epsilon$) models [5, 24]. First, since the model is *local*, it is suitable to implement on unstructured meshes. If a model is *non-local*, such as Baldwin-Lomax model, it requires information about the solution along lines normal to the wall, which is not readily available on unstructured meshes. Second, probably the most significant in computational aspect, because the working variable behaves linearly near the wall, it only require wall spacing of $y^+ \leq 3.5$ which is comparable to the Baldwin-Lomax model. This saves huge number of grid points near the wall compared to the $k-\epsilon$ model which typically requires $y^+ < 0.2$. Third, the model shown to offer much better performance for separated flows than Baldwin-Lomax model. In general, the Spalart-Allmaras model shows substantially improved performance than algebraic models with much less computational cost compared to the more expansive models such as two-equation models or Reynolds-stress models.

The Spalart-Allmaras eddy viscosity transport equation in differential form is expressed as follows

$$\frac{\partial \tilde{\nu}}{\partial t} + \frac{\partial}{\partial x_j}\left(\tilde{\nu} u_j\right) = C_{b1}\tilde{S}\tilde{\nu} + \frac{1}{\sigma}\left\{\frac{\partial}{\partial x_j}\left[\left(\nu + \tilde{\nu}\right)\frac{\partial \tilde{\nu}}{\partial x_j}\right] + C_{b2}\frac{\partial \tilde{\nu}}{\partial x_j}\frac{\partial \tilde{\nu}}{\partial x_j}\right\} - C_{w1} f_w \left(\frac{\tilde{\nu}}{d}\right)^2 \tag{2.17}$$

The complete model equation includes trip functions which are used for modeling laminar to turbulent transition at a pre-specified point, but the current turbulent simulation assumes that the entire flow field is affected by the turbulence model. Hence, no such trip functions are used. The terms on the LHS of equation (2.17) are the unsteady term and the convective flux term in conservative form. The terms on the RHS are the production term, the diffusive flux term, and the destruction term which includes the distance d to the nearest viscous wall as a variable. In order to determine the eddy viscosity, first the transport equation has to be solved for the working variable $\tilde{\nu}$ and then it is converted to eddy viscosity ν_t by the following formula

$$\nu_t = f_{v1}\tilde{\nu}$$

$$f_{v1} = \frac{\chi^3}{\chi^3 + C_{v1}^3}$$

$$\chi \equiv \frac{\tilde{\nu}}{\nu}$$

Constants and functions used in the model equation are

$$C_{b1} = 0.1355$$

$$\sigma = 2/3$$

$$C_{b2} = 0.622$$

$$C_{w1} = \frac{C_{b1}}{\kappa^2} + \frac{(1 + C_{b2})}{\sigma}$$

$$\tilde{S} \equiv S + \frac{\tilde{\nu}}{\kappa^2 d^2} f_{v2}$$

$$f_{v2} = 1 - \frac{\chi}{1 + \chi f_{v1}}$$

$$f_w = g \left[\frac{1 + C_{w3}^6}{g^6 + C_{w3}^6} \right]^{1/6}$$

$$g = r - C_{w2} \left(r^6 - r \right)$$

$$r \equiv \frac{\tilde{\nu}}{\tilde{S} \kappa^2 d^2}$$

The turbulence model equation can also be expressed in integral form as follows

$$\frac{\partial}{\partial t} \int\limits_V \tilde{\nu} dV + \oint\limits_S \left(F_c^{\tilde{\nu}} - F_v^{\tilde{\nu}} \right) dS = \int\limits_V Q^{\tilde{\nu}} dV \tag{2.18}$$

where the convective flux is given by

$$F_c^{\tilde{\nu}} = \tilde{\nu}\left(un_x + un_y + un_z\right)$$

and the diffusive flux is

$$F_v^{\tilde{\nu}} = n_x \tau_{xx}^{\tilde{\nu}} + n_y \tau_{yy}^{\tilde{\nu}} + n_z \tau_{zz}^{\tilde{\nu}}$$

Each component of the diffusive flux is defined as

$$\tau_{xx}^{\tilde{\nu}} = \frac{1}{\sigma}\left(\nu + \tilde{\nu}\right)\frac{\partial \tilde{\nu}}{\partial x}$$

$$\tau_{yy}^{\tilde{\nu}} = \frac{1}{\sigma}\left(\nu + \tilde{\nu}\right)\frac{\partial \tilde{\nu}}{\partial y}$$

$$\tau_{zz}^{\tilde{\nu}} = \frac{1}{\sigma}\left(\nu + \tilde{\nu}\right)\frac{\partial \tilde{\nu}}{\partial z}$$

Lastly, the source term is defined as follows

$$Q^{\tilde{\nu}} = C_{b1}\tilde{S}\tilde{\nu} + \frac{C_{b2}}{\sigma}\left\{\left(\frac{\partial \tilde{\nu}}{\partial x}\right)^2 + \left(\frac{\partial \tilde{\nu}}{\partial y}\right)^2 + \left(\frac{\partial \tilde{\nu}}{\partial z}\right)^2\right\} - C_{w1}f_w\left(\frac{\tilde{\nu}}{d}\right)^2$$

In order to couple the turbulence model equation with the mean flow equations, the time-stepping scheme of the turbulence equation should be in a consistent form with that of the mean flow equation. A dual time-stepping time-accurate formulation of the turbulence equation is given by

$$\frac{\partial}{\partial t^*}\int\limits_V \tilde{\nu}\,dV + R^*\left(\tilde{\nu}\right) = 0 \tag{2.19}$$

where t^* refers to pseudo time and R^* is the unsteady residual defined by

$$R^*\left(\tilde{\nu}\right) = \frac{\partial}{\partial t}\int\limits_V \tilde{\nu}\,dV + \oint\limits_S \left(F_c^{\tilde{\nu}} - F_v^{\tilde{\nu}}\right)dS - \int\limits_V Q^{\tilde{\nu}}\,dV$$

Once the unsteady residual is constructed by using the temporal and spatial discretization schemes, the steady state problem in pseudo time is solved for the eddy viscosity at the next time step. The pseudo transient problems for the turbulence model equation as expressed in equation (2.19) can be coupled with that of the mean flow equation (2.11). The two sets of equations are coupled and solved simultaneously, hence the flow field and eddy viscosity are strongly coupled and converge concurrently.

Chapter 3

Numerical Integration Scheme

A conservative finite volume scheme is presented for numerical flux computation on general hybrid meshes. A node-dual scheme is used for the construction of non-overlapping finite control volumes. Another conceptual finite volume, called edge-dual, is introduced for the velocity gradient computation of the viscous flux.

A new computationally efficient two-step (face-and-edge) algorithm is presented for the velocity gradient computation using the edge-duals. For computation of the convective numerical flux, two different schemes are introduced, namely a central difference scheme with artificial dissipation and a high order upwind scheme based on Roe's flux-difference splitting. In the present study, the upwind scheme is first applied to the hybrid meshes, while the central schemes has been employed for the hybrid meshes in the past. For the central scheme, different artificial dissipation models are discussed. Special methods for the application of boundary conidtions are presented for general hybrid meshes.

An implicit dual time-stepping scheme is presented for the time accurate formulation of the artificial compressibility method. A-stable backward difference formulas are introduced for the discretization of the true time-evolution term and an explicit multistage scheme is used for pseudo time-stepping.

3.1 Spatial discretization with general hybrid meshes

A conservative, finite-volume discretization scheme is used for solving the incompressible Navier-Stokes equations. A node-centered median dual scheme is used for spatial discretization. The edge-based algorithm is used for the computation of convective numerical fluxes. By employing the edge-based algorithm, the convective type flux computation routine runs a loop over edges (not nodes/faces). After a single loop over edges, each node receives complete convective flux contributions.

For viscous flux evaluation at an edge midpoint, another conceptual finite volume composed of its neighbor cells is used for the velocity gradient computation. A new efficient face-and-edge algorithm is presented for the computation of the velocity gradients. This face-and-edge algorithm is composed of two steps; the first involving a face-wise loop for the surface integrals of edge-duals, and the second edge-wise operations for the computation of velocity gradients and viscous fluxes.

Typical examples of node-centered median dual finite control volumes are delineated in figure 3.1. The region delimited by dashed lines around node i represents the node-dual in two dimensions. The node-dual is constructed by connecting lines defined by edge midpoints and centroids of the cells sharing the center node i. The L and R in Figure 3.1 represent left and right sides of node-dual boundary by assuming that the edge is directed outwards with respect to the node-dual i. In three dimensions as depicted in Figure 3.2, the node dual is constructed by connecting faces (instead of lines in two dimensions) defined by edge midpoints, cell centers and face centers sharing the common node n.

3.2 Convective flux

The convective flux for the node-dual i in discretized form can be expressed as

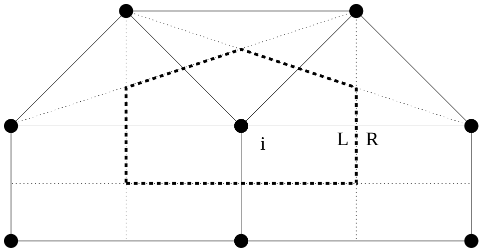

(a) node-dual with mixed cells

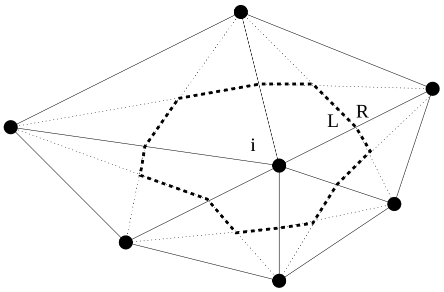

(b) node-dual with triangular cells

Figure 3.1: Node-duals in two dimensions

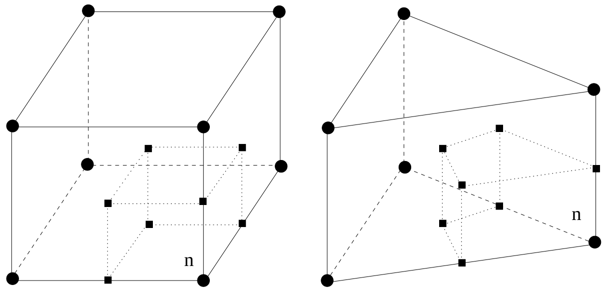

(a) Hexahedron (b) Prism

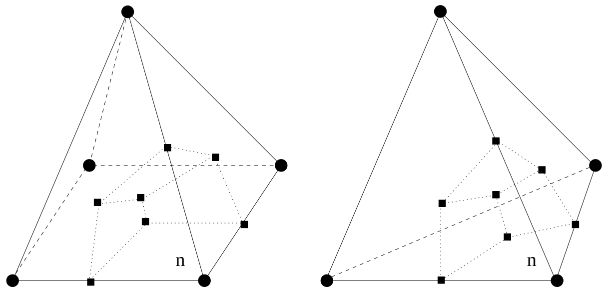

(c) Pyramid (d) Tetrahedron

Figure 3.2: Node-dual contributions from different types of elements in three dimensions

$$\oint_{S_i} (\mathbf{F}_I \mathbf{i} + \mathbf{G}_I \mathbf{j} + \mathbf{H}_I \mathbf{k}) \cdot \mathbf{n} dS \approx \sum_{j=1}^{J_i} (\mathcal{F})_j \Delta S_j = \mathbf{C}_i(\mathbf{Q}) \tag{3.1}$$

where $(\mathcal{F})_j = \mathbf{F}_I n_x + \mathbf{G}_I n_y + \mathbf{H}_I n_z$ is the numerical flux evaluated at the midpoint of edge j, J_i is the number of edges connected to the node i and n_x, n_y, and n_z are the components of the outward unit normal vector of the node-dual boundary, and ΔS_j is the portion of the node-dual boundary associated with edge j . $\mathbf{C}_i(\mathbf{Q})$ is the summation of the numerical convective fluxes through the control volume boundary which makes the total contribution of the convective flux to node i.

A typical formation of a fraction of the node-dual boundary associated with an edge is delineated in Figure 3.3 for two dimensions and in Figure 3.4 for three dimensions. In two dimensions, the surface normal to the node-dual is approximated by

$$\mathbf{n}_{ij} = \mathbf{n}_L + \mathbf{n}_R$$

where the subscripts L and R represent the left and right side respectively assuming that the edge is directed from node i to node j.

In three dimensions, the surface normal is computed by

$$\mathbf{n}_{ij} = \sum_{k=1}^{K} \mathbf{n}_k$$

where K is the total number of faces associated with the edge $i - j$. Since an arbitrary number of elements can share a common edge, the number of faces associated with the edge can also vary.

As shown in figures 3.3 and 3.4, the fragments of the node-dual boundary are not necessarily colinear (coplanar in three dimensions) to each other, nor perpendicular to the edge. Nevertheless, if the mesh is regular, these fractions of the node-dual boundary are close to being colinear (coplanar in three dimensions) to each other and perpendicular to the edge.

3.2.1 Central difference

Both the central difference and upwind schemes are used for the convective flux evaluation. For the central difference scheme, the numerical flux is evaluated at the node-dual boundary by the arithmetic averaging of the fluxes at the two end nodes as shown in Eq. (3.2).

$$\left(\mathcal{F}_{central}\right)_j = \frac{1}{2}\left(\mathcal{F}\left(\mathbf{Q}_i\right) + \mathcal{F}\left(\mathbf{Q}_j\right)\right) \tag{3.2}$$

Since the central difference scheme is susceptible to the odd-even mode decoupling and solution oscillations, an additional artificial dissipation term is needed. Different artificial dissipation models are tested. A more detailed discussion of the artificial dissipation models is presented in a later section.

3.2.2 Upwind by Roe's flux-difference splitting

Instead of the central scheme with the supplementary artificial dissipation term, an upwind scheme can be used by evaluating the numerical fluxes using Roe's approximate Riemann solver [69, 70] as follows

$$\mathcal{F}_{upwind} = \frac{1}{2}\left(\mathcal{F}\left(\mathbf{Q}_L\right) + \mathcal{F}\left(\mathbf{Q}_R\right)\right) + \frac{1}{2}\left|\hat{\mathbf{A}}\left(\mathbf{Q}_R, \mathbf{Q}_L\right)\right|\left(\mathbf{Q}_L - \mathbf{Q}_R\right) \tag{3.3}$$

where the $\mathcal{F}\left(\mathbf{Q}_L\right)$ and $\mathcal{F}\left(\mathbf{Q}_R\right)$ are the convective flux vectors from the solutions reconstructed on the left $\left(\mathbf{Q}_L\right)$ and right $\left(\mathbf{Q}_R\right)$ sides of the control volume boundary as delineated in Figure 3.1. These solutions at the edge midpoint are reconstructed by using Taylor series expansions about the two end nodes, which requires pre-computation of nodal gradients of the solutions.

Roe's matrix $\left|\hat{\mathbf{A}}\right|$ is defined as

$$\left|\hat{\mathbf{A}}\right| = \mathbf{R}\left|\hat{\mathbf{\Lambda}}\right|\mathbf{R}^{-1}$$

where $\mathbf{R}$ is the right eigenvector matrix of the flux Jacobian, $\mathbf{R}^{-1}$ is its inverse, and $\left|\hat{\mathbf{\Lambda}}\right|$ is a diagonal matrix whose components are absolute values of the eigenvalues. Roe's matrix $\hat{\mathbf{A}}$ satisfies the following three properties

1. $\hat{\mathbf{A}}\left(\mathbf{Q}, \mathbf{Q}\right) = \mathbf{A}\left(\mathbf{Q}\right)$ where $\mathbf{A}\left(\mathbf{Q}\right) = \frac{\partial \mathbf{F}}{\partial \mathbf{Q}}$ is the flux Jacobian
2. $\hat{\mathbf{A}}\left(\mathbf{Q}_R, \mathbf{Q}_L\right)$ is diagonalizable and has real eigenvalues
3. For any $\mathbf{Q}_R, \mathbf{Q}_L$, $\hat{\mathbf{A}}\left(\mathbf{Q}_R, \mathbf{Q}_L\right) \times \left(\mathbf{Q}_R - \mathbf{Q}_L\right) = \mathbf{F}\left(\mathbf{Q}_R\right) - \mathbf{F}\left(\mathbf{Q}_L\right)$

Property 1 is concerned with the consistency condition which guarantees that the approximate solution converges to the exact solution smoothly as $\mathbf{Q}_L$ and $\mathbf{Q}_R$ approach each other. Property 2 guarantees that the linearized system is hyperbolic. Property 3 ensures that the approximate solution is exact if $\mathbf{Q}_L$ and $\mathbf{Q}_R$ can be connected by a single discontinuity.

As shown by Taylor and Whitfield [85], for the incompressible Euler equations with artificial compressibility, each component of Roe's matrix can be constructed by arithmetic averaging of the left and right states, which results in satisfaction of all three conditions for Roe's matrix. A nonsingular eigensystem of Roe's matrix was reported by Anderson *et al.* [4] in two dimensions, and by Kim [38] in three dimensions.

When the first order upwind scheme is employed, the solutions at the left and right sides of the control volume boundary can be chosen simply as the solutions at the two end nodes. However, for high order upwind schemes, the solutions at the control volume boundary must be reconstructed by using the Taylor series expansions about the two end nodes. The solution reconstruction from the two end nodes to the edge mid-point which represents the node-dual boundary can be expressed as

$$\mathbf{Q}_L = \mathbf{Q}_i + \frac{1}{2}\left(\nabla \mathbf{Q}\right)_i \cdot \Delta \mathbf{r}_{ij} \tag{3.4}$$

$$\mathbf{Q}_R = \mathbf{Q}_j - \frac{1}{2}\left(\nabla \mathbf{Q}\right)_j \cdot \Delta \mathbf{r}_{ij} \tag{3.5}$$

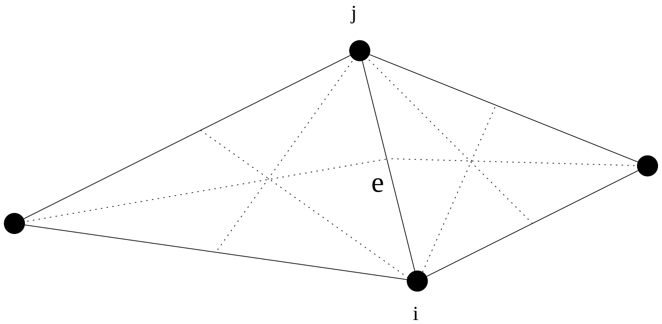

(a) a formation of edge $i - j$ in a 2D triangular region

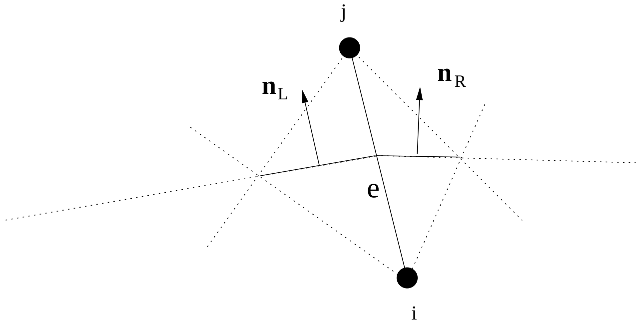

(b) node-dual boundary (poly-line) associated with edge $i - j$

Figure 3.3: Fraction of node-dual boundary associated with an edge in two dimensions. Always two (left and right) line segments are associated with an edge, except for edges on the boundary. The two line segments (on the left and right side of edge $i - j$) are not necessarily colinear nor perpendicular to the edge.

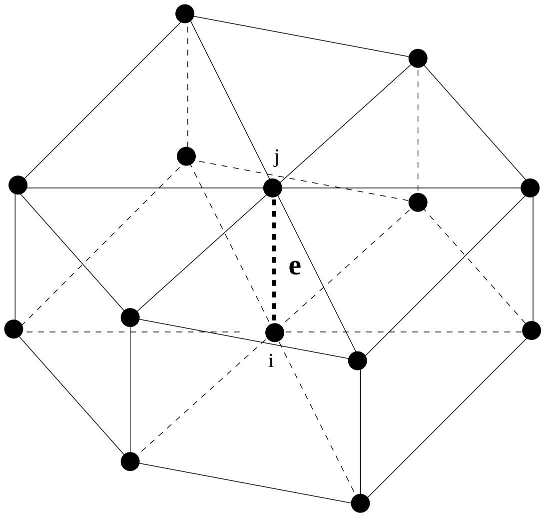

(a) an example of edge $i - j$ in a 3D prismatic region

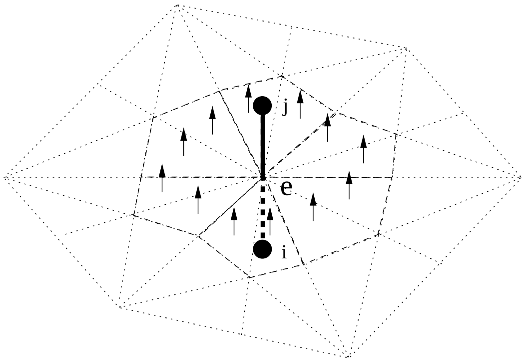

(b) node-dual boundary (poly-surface) associated with edge $i - j$

Figure 3.4: Fraction of node-dual boundary associated with an edge in three dimensions. An arbitrary number of surface segments are associated with an edge. The surface segments are not necessarily coplanar nor perpendicular to the edge.

where the $\Delta\mathbf{r}_{ij}$ is the distance vector from node i to node j, and $\nabla\mathbf{Q}$ is the nodal gradient of the solution which is evaluated by a least-squares procedure [3]. The Gram-Schmidt process is used for solving the least-squares problem ($\mathbf{Ax} = \mathbf{b}$) by decomposing the coefficient matrix $\mathbf{A}$ into a product of an orthogonal matrix $\mathbf{Q}$ and an upper (right) triangular matrix $\mathbf{R}$. This Gram-Schmidt process allows for pre-computation of all weights only from the geometric information. Hence, the actual computation of the nodal gradients using the least-squares procedure can be implemented just by a single loop over edges. For more details, Anderson and Bonhaus [3] for two dimensions and Haselbacher and Blazek [28] for three dimensions may be consulted.

The surface integral in discrete form as expressed in Eq. (3.1) is presented in a node-wise fashion. However, the actual computation is performed in an edge-wise manner by visiting each edge only once, computing the flux contributions, and sending the positive contribution to the node inside and the negative contribution to the node outside depending on the direction of the edge.

Since this convective flux computation is purely edge-based, all nodes get the total contribution of the convective flux after a single edge-loop. This edge-wise algorithm does not require any information about cell topology, so the algorithm is suitable especially for general hybrid meshes which include various types of elements in a single computational domain.

3.3 Viscous flux

In order to evaluate the viscous fluxes through control volume boundaries, the gradients of velocity components are needed to be pre-computed at each edge. For this velocity gradient computation, another conceptual finite volume called edge-dual is constructed. The edge-dual is composed of the neighbor cells sharing a common edge. Various kinds of edge-duals encountered in hybrid meshes are delineated in

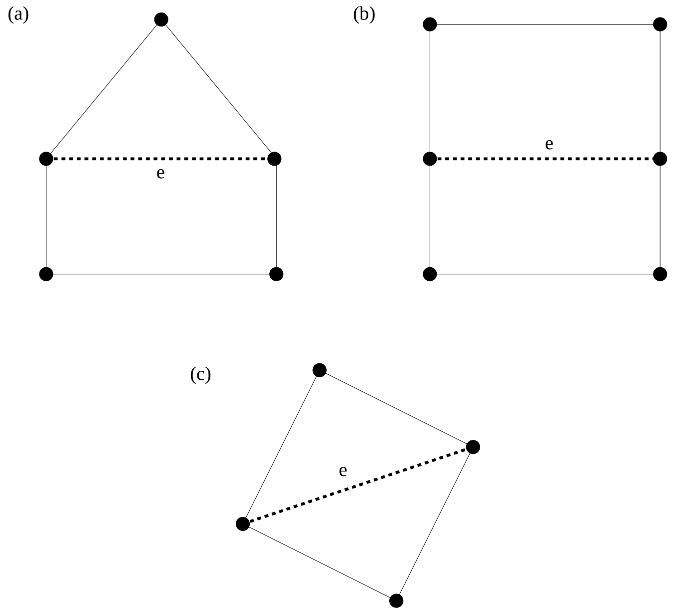

Figure 3.5: Various formations of edge-duals in two dimensions. An edge-dual is composed of neighbor cells sharing a common edge (e), indicated by thick dashed lines.

Fig. 3.5 in two dimensions and Fig. 3.6 in three dimensions.

For the computation of velocity gradients at each edge, the divergence theorem is used and the surface integrals along edge-dual boundaries are evaluated. For example, computing the volume averaged value of $\frac{\partial u}{\partial x}$ using an edge-dual can be expressed as

$$\left(\frac{\partial u}{\partial x}\right)_e = \frac{1}{V_e}\oint_{S_e} u n_x dS \tag{3.6}$$

where V_e is the volume of the edge-dual and S_e is its boundary.

This approach has been advocated by other researchers [10, 8] because it is less susceptible to solution wiggles and can be applied on more compact stencils than

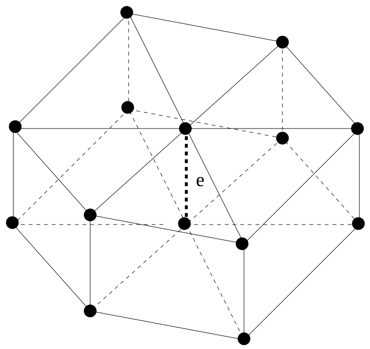

(a) edge-dual composed of prisms

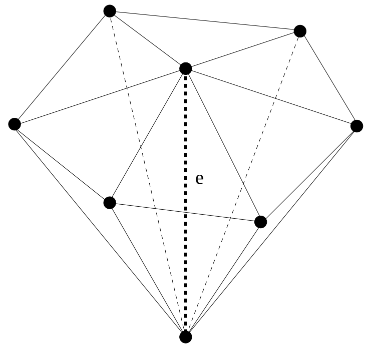

(b) edge-dual composed of tetrahedra

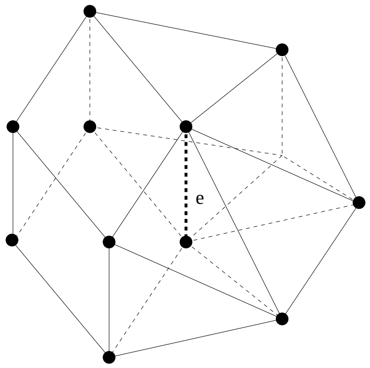

(a) edge-dual composed of mixed cells

Figure 3.6: Various formations of edge-duals in three dimensions. An edge-dual is composed of neighbor cells sharing a common edge (e), indicated by thick dashed lines.

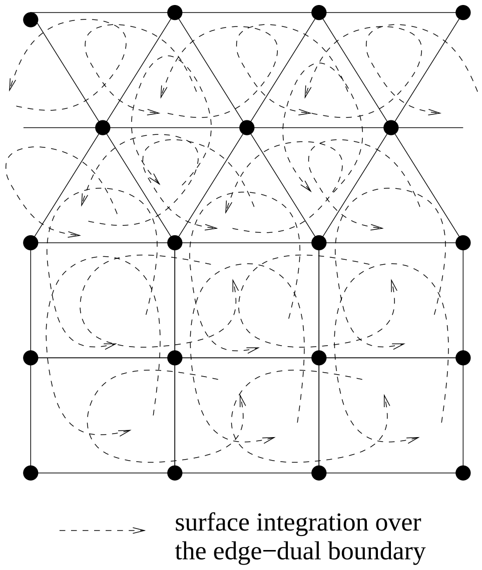

Figure 3.7: Surface integration over the edge-dual boundary with the conventional algorithm; visitting edges and performing surface integration over the edge-dual boundary.

other methods, for example, evaluating velocity gradient at nodes and averaging the nodal velocity gradients at each edge. However, visiting edges and performing surface integration over various kinds of edge-duals introduces excessive complexity.

The actual implementation of the surface integral over the edge-duals as expressed in Eq. (3.6) and delineated in figure 3.7 has two major drawbacks. First, it needs additional connectivity information of edge-to-faces for each edge-dual. In two dimensions, an edge-dual is composed of four to six edges, so each edge has to store its edge-dual connectivity information of four to six integers. In three dimensions, this edge-to-faces connectivity information reaches up to eighteen integers (faces) for an edge in a prismatic region and sixteen integers (faces) for an edge in a hexahedral region. Second, and probably more seriously, it requires redundant visits of a surface,

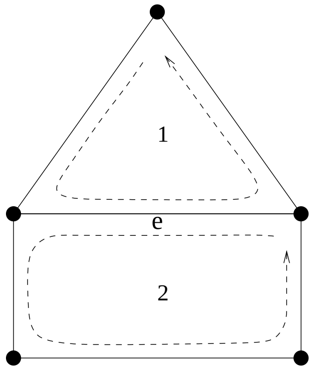

Figure 3.8: Cell-wise surface integrals for velocity gradient computations using edge-duals

because a surface typically belongs to multiple edge-duals. In two dimensions the number of visits of an edge is four if the edge is in a triangular region, five if the edge is on the interface of triangular and quadrilateral regions, and six if the edge is in a quadrilateral region, and can be counted by using figure 3.7 These redundant visits of a face become more severe in three dimensions. For a face in a hexahedral region, the number of visits of the face is approximately sixteen, which can be a major obstacle for viscous simulations.

A new computationally efficient algorithm is now presented for the velocity gradient computation using the edge-duals. In the algorithm, as depicted in Fig. 3.8 for an edge-dual in two dimensions, the surface integrals over the edge-duals are evaluated in two steps. At the first step, the cell-wise surface integrals are computed by a single edge-loop. At the second step, the cell-wise surface integrals are gathered at the common edge and are divided by the sum of the volumes of neighbor cells, which is the edge-dual volume. The cell-wise surface integrals are delineated in Fig. 3.8, and the final computation of $\frac{\partial u}{\partial x}$ at the common edge is given by

$$\left(\frac{\partial u}{\partial x}\right)_e = \frac{\oint_1 un_x dS + \oint_2 un_x dS}{V_1 + V_2} \tag{3.7}$$

where V_1 and V_2 are the volumes of triangular and quadrilateral cells in Fig. 3.8. The cell-wise surface integrals which are represented with dashed lines in Fig. 3.8 can be computed by a single edge-loop. In three dimensions, this edge-loop is replaced with a face-loop because cells in three dimensions are delimited with faces. At the second loop over edges, the pre-computed surface integrals from the neighbor cells are gathered at the common edge. By the summation of the surface integrals from neighbor cells, the contributions from common faces (edges in two dimensions) which reside inside of the edge-dual automatically cancel out, and the summation recovers the net surface integral over the edge-dual. Finally, the division of the surface integral by the edge-dual volume yields the edge-dual averaged velocity gradients.

This edge-dual approach can also be interpreted as the computation of velocity gradients by volume weighted averaging of velocity gradients at the neighbor cells as shown in

$$\left(\frac{\partial u}{\partial x}\right)_e = \left(\frac{1}{V_1}\oint_1 un_x dS\right) w_1 + \left(\frac{1}{V_2}\oint_2 un_x dS\right) w_2 \tag{3.8}$$

where $w_1 = \frac{V_1}{V_1+V_2}$ and $w_2 = \frac{V_2}{V_1+V_2}$ are the weights for the neighbor cells. In the end, all velocity gradient computations expressed in equations (3.6), (3.7), and (3.8) provide the same result.

Since each cell has to store these surface integrals from the first loop, an extra memory space is needed for each cell. This extra cell-wise memory space is four real variables in two dimensions and nine real variables in three dimensions, and each of them corresponds to a component of the velocity gradient. Additionally, for the second loop over edges, connectivity information of *edge-to-(neighbor)cells* should be pre-constructed. This *edge-to-(neighbor)cells* information requires the memory space of two integers in two dimensions and four to six integers in the hexahedral/prismatic region in three dimensions. Overall, the major saving from the proposed algorithm comes from the CPU time, and the memory requirement of the new algorithm of equation (3.7) is comparable to the conventional method of equation (3.6).

This two-step algorithm can be expressed in a pseudo-code as follows

```
for each face do
    $(uS_x)_{inside\,cell} = (uS_x)_{inside\,cell} + (uS_x)_{face}$
    $(uS_x)_{outside\,cell} = (uS_x)_{outside\,cell} - (uS_x)_{face}$
end

for each edge do
    $\left(\frac{\partial u}{\partial x}\right)_{edge} = \frac{\sum\limits_{neighbor\,cells} (uS_x)}{\sum\limits_{neighbor\,cells} (V)}$
end
```

The above pseudo-code can be delineated graphically in two dimensions as shown in figure 3.9.

Once the velocity gradients are computed at all edges, the same edge-wise operation is used for the viscous flux evaluation at node i as shown below

$$\oint\limits_{S_i} \left(\mathbf{F}_V\mathbf{i} + \mathbf{G}_V\mathbf{j} + \mathbf{H}_V\mathbf{k}\right) \cdot \mathbf{n}dS \approx \sum_{j=1}^{J_i} \left(\mathcal{F}_V\right)_j \Delta S_j = \mathbf{V}_i(\mathbf{Q}) \tag{3.9}$$

where $(\mathcal{F}_V)_j = \mathbf{F}_V n_x + \mathbf{G}_V n_y + \mathbf{H}_V n_z$ is the viscous flux evaluated at edge j, J_i is the number of edges connected to node i, ΔS_j is the area of the node-dual boundary associated with the j_{th} edge, and $\mathbf{V}_i(\mathbf{Q})$ is the total contribution of the viscous fluxes to node i.

Except the pre-computation of velocity gradients at edges, the viscous flux

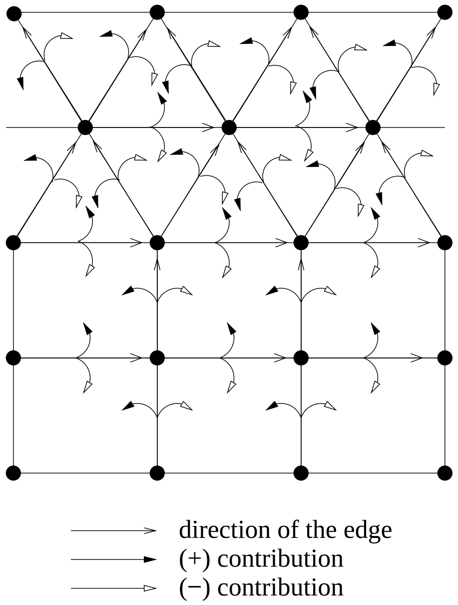

(a) face-wise loop for cell-wise surface integration

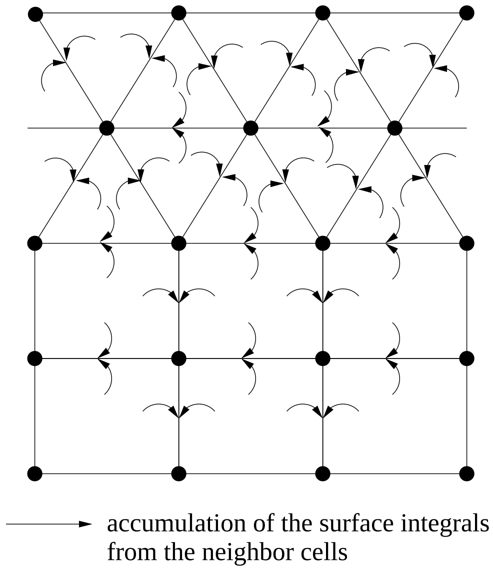

(b) edge-wise loop for the evaluation of the surface integrals

Figure 3.9: Computationally efficient two-step (*face-and-edge*) algorithm for the surface integrals over edge-duals in two dimensions.

computation of Eq. (3.9) can be performed in an edge-wise fashion. This edge-wise operation for viscous flux evaluation can be combined with the second step of the face-and-edge algorithm as presented in the pseudo-code, hence the viscous flux computation can be completed by a pair of face-and-edge loops.

3.4 Artificial Dissipation

Central difference schemes exhibit high frequency spurious oscillations of solutions, and these oscillations are believed to be triggered by the nonlinear nature of the governing equations. In order to suppress this high frequency oscillation, an additional smoothing term is needed. For flows with discontinuities, such as shocks, a blend of second and fourth order difference artificial dissipation is used [32]. Current simulations of incompressible flows, where the speed of sound is always greater than flow speed, no such discontinuities exist. Hence, only fourth order difference artificial dissipation is added to suppress the spurious oscillations.

The conventional scalar smoothing for a node i can be expressed as below

$$\mathbf{D}_i(\mathbf{Q}) = -\sum_{j=1}^{J_i} \sigma_4 \rho_{ij} \left(\delta_{xx}\mathbf{Q}_j - \delta_{xx}\mathbf{Q}_i\right) \tag{3.10}$$

Here, J_i is the number of nodes connected to node i by its neighbor edges, ρ_{ij} is an estimate of the spectral radius associated with the j_{th} neighbor edge, and δ_{xx} is an undivided second order difference operator defined as follows

$$\delta_{xx}\mathbf{Q}_i = \sum_{j=1}^{J_i} \left(\mathbf{Q}_j - \mathbf{Q}_i\right) \tag{3.11}$$

For nodes on the boundary, the contribution of the undivided Laplacian is incomplete. Hence, the undivided Laplacian is extrapolated from the adjacent nodes above the boundary down to the nodes on the boundary. The estimate of the spectral radius scaled by the node-dual boundary associated with edge j is defined as

$$\rho_{ij} = \left(|u_n| + c\right) \Delta S_j \tag{3.12}$$

where the velocity normal to the node dual boundary is

$$u_n = un_x + vn_y + wn_z$$

and the artificial speed of sound defined as follows

$$c = \sqrt{u_n^2 + \beta}$$

The spectral radius at each edge is scaled by the area of the node-dual boundary ΔS_j associated with the edge j, and the normal velocity u_n is associated with the direction normal to the node-dual boundary associated with the j_{th} edge. This scaling is often called individual eigenvalue scaling [82] and has been reported that it is adequate for meshes with aspect ratios up to the order of $O(10)$ [46].

By scaling the spectral radius with the node-dual boundary, the actual contribution of artificial dissipation is dimensionally consistent with the surface integrals of convective and viscous fluxes. Ideally, on a uniform mesh, the final contribution of artificial dissipation when divided by the node-dual volume is

$$\frac{1}{V_i}\mathbf{D}_i\left(\mathbf{Q}\right) = \sigma_4 O\left(\Delta x^3\right) \nabla^4 \mathbf{Q}$$

Therefore, the added artificial dissipation which is a third-order term should not affect the spatial accuracy of the central difference scheme which is of second order. However, on meshes with high aspect ratios, the artificial dissipation may not be scaled properly [46, 83, 82]. Furthermore, a severe oscillation on hybrid meshes has been reported by Haselbacher and Blazek [28] when the explicit Runge-Kutta scheme is used in conjunction with a central scheme. Haselbacher and Blazek proposed a modified artificial dissipation scheme as expressed below

$$\mathbf{D}_i(\mathbf{Q}) = -\sum_{j=1}^{J_i} \sigma_4 \rho_{ij} \left(\mathbf{Q}_L - \mathbf{Q}_R\right) \tag{3.13}$$

based on the difference of the reconstructed solutions ($\mathbf{Q}_L$ and $\mathbf{Q}_R$) on the left and the right side of the control volume boundary . Taylor series expansions are used for solution reconstruction at the node-dual boundary as presented in equations (3.4) and (3.5). Note that the artificial dissipation model expressed in equation (3.13) results in a second-order accurate dissipation scheme which is equivalent to the conventional artificial dissipation based on undivided Laplacians as expressed in equation (3.13). If instead of using the Taylor series expansions, the left and right states are simply chosen as the nodal states on both sides of the boundary, then the second-order accurate dissipation scheme reduces to a first-order accurate scheme as below

$$\mathbf{D}_i(\mathbf{Q}) = -\sum_{j=1}^{J_i} \sigma_4 \rho_{ij} \left(\mathbf{Q}_i - \mathbf{Q}_j\right) \tag{3.14}$$

3.5 Comparisons of dissipation models on a general hybrid mesh

Central differences with the two different artificial dissipation models as well as Roe's upwind scheme are tested for the investigation of their applicability to the general hybrid meshes. The general hybrid mesh used for the current comparison of artificial dissipation models is displayed in Figures 1.2 and 6.6. It includes local hexahedra on the frontal viscous region of the cylinder, prisms in its rear half, pyramids at the interface between the hexahedral and tetrahedral regions, and tetrahedra for the rest.

The comparison between the central difference schemes with the conventional artificial dissipation and the modified artificial dissipation based on the solution re-

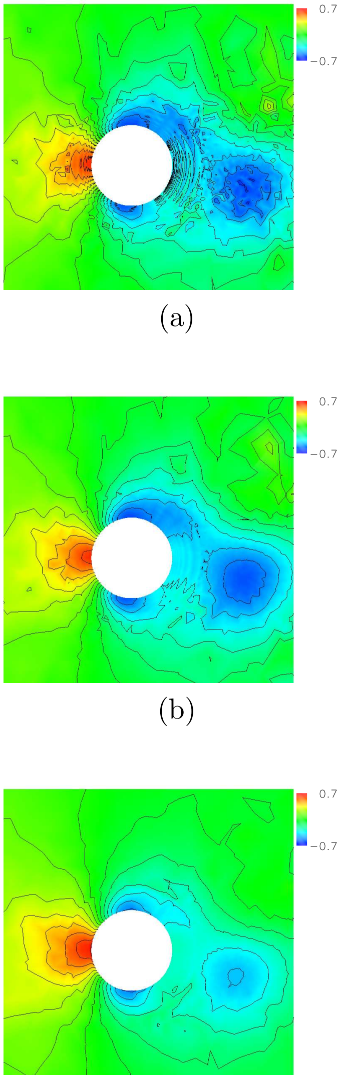

(a)

(b)

(c)

Figure 3.10: Comparison of pressure contours obtained with different dissipation models. (a) corresponds to the conventional scalar dissipation model, (b) to the modified dissipation model of Haselbacher and Blazek, and (c) to the implicit dissipation by upwind scheme. The pressure contours on the plane cuts are obtained at the same time within a shedding cycle. $Re = 150$.

constructions are presented. The second order upwind scheme result is also included. The pressure contours obtained by using the aforementioned schemes are displayed in Fig. 3.10.

First, the conventional dissipation model shows severe oscillation in the pressure contours, which indicates that the scheme is incapable of suppressing the solution oscillations on general hybrid meshes. Furthermore, as pointed by Haselbacher and Blazek [28], this smoothing model shows a severe stability problem on hybrid meshes when it is driven by the explicit Runge-Kutta time-stepping scheme which is used in the current study.

The modified smoothing model of Haselbacher and Blazek [28] based on the differences of the reconstructed solutions (Eq. (3.13)) is tested, and then compared with the second order upwind scheme by using Roe's flux-difference splitting. The Haselbacher and Blazek's scheme shows superior ability of suppressing the oscillations to the conventional dissipation scheme. The pressure contours are similar to the ones yielded by the upwind scheme.

The computational cost of the modified smoothing is slightly higher than the conventional smoothing due to the solution reconstruction step for each edge. However, the modified smoothing is still less expensive than the upwind scheme, because the upwind scheme requires the evaluation of Roe's matrix at each edge.

In general, in the regions of highly stretched cells and anisotropic support of the edges (eg. along the interfaces of prisms/hexahedra and tetrahedra/pyramids, where only a single edge resides inside of the prismatic/hexahedral region), the Haselbacher and Balzek dissipation model and upwind scheme yield more smooth pressure contours than the conventional scalar dissipation model. Hence, for general hybrid meshes, the central difference scheme with the modified dissipation model of Haselbacher and Blazek or upwind schemes are preferred to the conventional scalar dissipation model.

3.6 Boundary Conditions

Boundary conditions are classified into viscous wall, inlet, outlet, far field, and symmetry plane. On the viscous wall, which is the surface of the cylinder, no slip condition is specified and pressure is extrapolated from the domain such that the gradient of pressure along the normal direction is zero.

For inlet and outlet boundaries, special attention is needed. Since the current solution scheme is based on the artificial compressibility method, the flow field can be considered as compressible until the solution is completely converged. Hence, the application of the boundary condition should also follow that of the compressible flow part (always subsonic though). For subsonic compressible flows, there exist one out-going characteristic wave and three incoming waves at the inlet, and three out-going and one in-coming characteristic waves at the outlet [21].

Typically, at the inlet pressure is extrapolated to account for the unique out-going wave, and all velocity components are specified with free stream values for the three in-coming characteristic waves. At the outlet, all velocity components are extrapolated for the three out-going waves and only pressure is specified as the free stream quantity due to the one in-coming wave. At the far field boundaries, the top and bottom planes are parallel to the free stream and cylinder; there pressure is extrapolated and velocities are specified just as in the free stream. On the symmetry plane, which is perpendicular to the axis of the cylinder, all quantities are extrapolated except the velocity component normal to the plane, which is set to zero. This symmetry plane can also be treated as a periodic plane.

All boundary condition application routines can be implemented either by Neumann or Dirichlet type. Hybrid meshes do not impose extra complexity for application of the Dirichlet type boundary condition. Node-wise specification of appropriate values is sufficient. For the Neumann type boundary condition, the actual implementation can be either node-wise or cell-wise. For the current hybrid meshes, both of the methods (node-wise and cell-wise) are used in order to take advantage of the geometric characteristics of hybrid meshes. On the viscous wall, typically very thin layers of hexahedral or prismatic cells are located with good normality condition. Hence, on the wall, a node-wise extrapolation scheme is the best. On the boundaries other than the viscous wall, the good normality condition is no longer valid. Hence, the cell-wise extrapolation is employed. The cell-wise extrapolation is composed of two steps. At the first step, a cell-averaged value is computed, and then at the second step this cell averaged value is projected on the boundary face and extrapolated to each one of boundary nodes by using inverse-distance weighting. The weights for each one of the boundary nodes are pre-computed, and also the sum of the weights is checked to be unity for all boundary nodes at which we get the cell-wise extrapolation. This two extrapolation processes are delineated in Figure 3.11 for two dimensional hybrid meshes and Figure 3.12 for three dimensional general hybrid meshes.

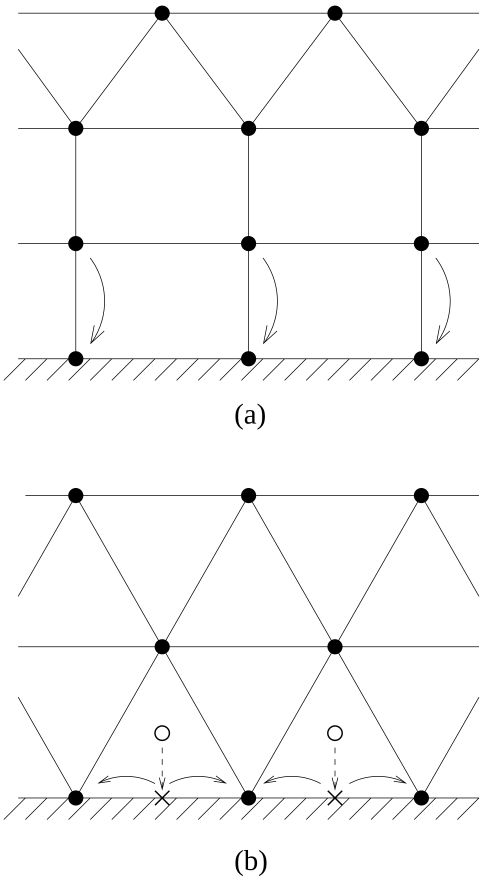

Figure 3.11: Two dimensional application of the extrapolation boundary condition: (a) node-wise direct application on viscous wall and (b) cell-wise two step application on other types of boundaries such as far fields, inlet or outlet.

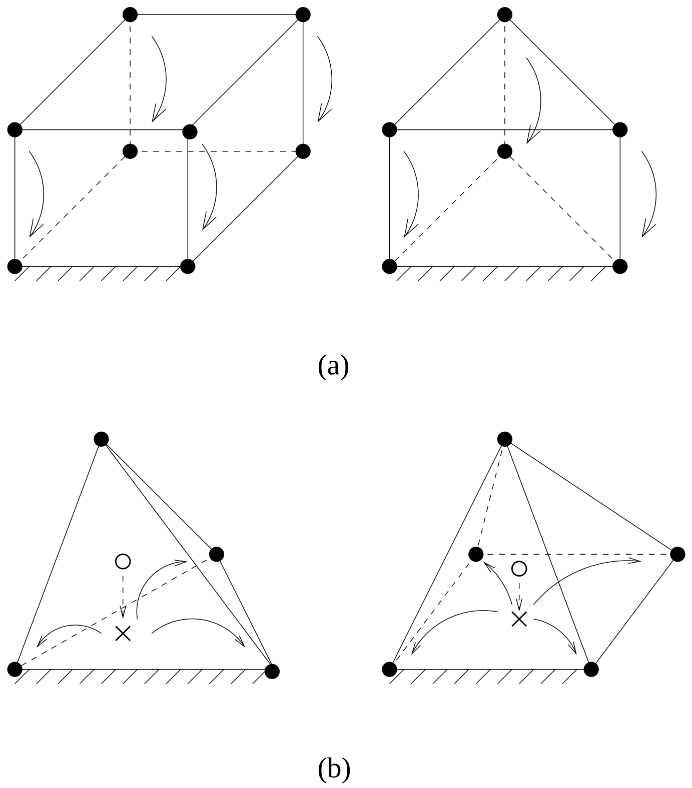

(a)

(b)

Figure 3.12: Three dimensional application of the extrapolation boundary condition: (a) on viscous wall and (b) other boundaries such as far fields, symmetric planes, inlet or outlet

3.7 Dual time-stepping scheme

Current time-accurate formulation of the artificial compressibility method includes two different time evolution terms: one in true (physical) time t and the other in pseudo time t^*. First, the true time-derivative term is discretized by using the second order backward difference formula, and then the pseudo time-derivative term is integrated until it reaches the steady state in pseudo time. Hence, the current time-accurate simulation is driven by a series of steady state problems in pseudo-time, and each of the steady state problems corresponds to a single true time-step.

Evaluating all flux contributions to the finite control volume V_i and adding the supplementary artificial dissipation term, which is necessary for a central difference scheme, yields the dual time-stepping time accurate formulation

$$\mathbf{P}\frac{d}{dt^*}\left(\mathbf{Q}_i V_i\right) + \frac{d}{dt}\left(\mathbf{U}_i V_i\right) + \mathbf{C}_i\left(\mathbf{Q}\right) = \mathbf{V}_i\left(\mathbf{Q}\right) + \mathbf{D}_i\left(\mathbf{Q}\right) \tag{3.15}$$

where $\mathbf{C}_i\left(\mathbf{Q}\right)$ is the convective flux, $\mathbf{V}_i\left(\mathbf{Q}\right)$ is the viscous flux, and $\mathbf{D}_i\left(\mathbf{Q}\right)$ is the added artificial dissipation.

If the upwind scheme is used, there is no need to include such an artificial dissipation term. This is because the upwind scheme includes dissipation implicitly in the numerical convective flux. The system of equations can be further simplified to

$$\mathbf{P}\frac{d}{dt^*}\left(\mathbf{Q}_i V_i\right) + \mathbf{R}_i^*\left(\mathbf{Q}\right) = 0 \tag{3.16}$$

by introducing the unsteady residual $\mathbf{R}_i^*\left(\mathbf{Q}\right)$ defined as follows

$$\mathbf{R}_i^*\left(\mathbf{Q}\right) = \frac{3}{2\Delta t}\left(\mathbf{U}_i^{n+1} V_i^{n+1}\right) - \frac{2}{\Delta t}\left(\mathbf{U}_i^{n} V_i^{n}\right) + \frac{1}{2\Delta t}\left(\mathbf{U}_i^{n-1} V_i^{n-1}\right) + \mathbf{R}_i\left(\mathbf{Q}\right)$$

The unsteady residual $\mathbf{R}_i^*\left(\mathbf{Q}\right)$ is the sum of the true time-derivative term discretized by using the second order backward difference formula, and the steady residual which includes all flux terms, defined by

$$\mathbf{R}_i\left(\mathbf{Q}\right) = \mathbf{C}_i\left(\mathbf{Q}\right) - \mathbf{V}_i\left(\mathbf{Q}\right) - \mathbf{D}_i\left(\mathbf{Q}\right)$$

In order to advance a time step from the current time t_n to the next time t_{n+1} , the unsteady residual $\mathbf{R}^*(\mathbf{Q})$ is first constructed by discretizing the true time-derivative with the implicit backward difference formula, and then the steady-state problem shown in equation (3.16) is being solved in pseudo time. Once the steady-state in pseudo-time is reached, the pseudo time-derivative vanishes and the solution has been advanced to the next time step.

The dual time-stepping scheme is driven by the time integration scheme for the pseudo steady-state problem. Therefore, the overall performance of the dual time-stepping scheme is highly dependent on the efficiency of the steady-state solver in pseudo time

$$\frac{d}{dt^*}\left(\mathbf{Q}_i^k V_i\right) + \mathbf{P}^{-1}\mathbf{R}_i^*\left(\mathbf{Q}^k\right) = 0 \tag{3.17}$$

An iterative scheme using a 5-stage scheme is used for solving the steady-state problem in pseudo time. In the equation (3.17), k is the index for the iteration in pseudo time. This iteration is referred to as the sub-iteration, because the iteration loop is inside of the true time-stepping. In pseudo time-stepping there is no need to preserve the transient temporal accuracy, so the local time-stepping is used for convergence acceleration in pseudo time. The 5-stage multistage scheme used for each subiteration is presented below

$$\begin{array}{ccc}
\mathbf{Q}^{(0)} & = & \mathbf{Q}^k \\
 & \vdots & \\
\mathbf{Q}^{(l)} & = & \mathbf{Q}^{(0)} - \alpha_l \Delta t_i^* \frac{1}{V_i}\mathbf{P}^{-1}\mathbf{R}_i^*\left(\mathbf{Q}^{(l-1)}\right) \\
 & \vdots & \\
\mathbf{Q}^{k+1} & = & \mathbf{Q}^{(5)}
\end{array} \tag{3.18}$$

stage	central difference		upwind
l	α_l	β_l	α_l
1	0.2500	1.00	0.0533
2	0.1667	0.00	0.1263
3	0.3750	0.56	0.2375
4	0.5000	0.00	0.4414
5	1.0000	0.44	1.0000

Table 3.1: Multistage coefficients for central difference and upwind schemes. Coefficients for the central difference scheme are designed for the maximum stability region, and the coefficients for the upwind scheme are designed for optimal high frequency dampling.

where $\alpha_1, \cdots, \alpha_5$ are multistage coefficients, and Δt_i^* is the local pseudo time step for node i.

If the central difference scheme is employed, in order to achieve large stability intervals for the multistage scheme, the convective and dissipative fluxes (viscous flux and artificial dissipation) are treated in a distinct fashion, and those are expressed as follows

$$\mathbf{R}^{(l)} = \mathbf{C}^{(l)} - \mathbf{R}^{(l)}_{\text{dissipative}} \tag{3.19}$$

and a combination of the dissipative fluxes at current and previous stages is used, and is defined by

$$\mathbf{R}^{(l)}_{\text{dissipative}} = (\beta_l)\left(\mathbf{V}^{(l)} + \mathbf{D}^{(l)}\right) + (1-\beta_l)\left(\mathbf{V}^{(l-1)} + \mathbf{D}^{(l-1)}\right) \tag{3.20}$$

The coefficients α_l in equation (3.18) are chosen to maximize the stability interval along the imaginary axis and the coefficients β_l in equation (3.20) are chosen to increase the stability interval along the negative real axis [46]. Using this approach, the dissipative fluxes need to be evaluated only at odd stages. This multistage scheme is referred to as the modified multistage scheme compared to the scheme of evaluating all fluxes at every stage.

For the upwind scheme, all fluxes are evaluated at every stage. The multistage coefficients $\alpha_1, \cdots, \alpha_5$ for the upwind scheme are originally presented in [95]. They are designed for optimal high frequency damping. All the coefficients for the multistage scheme are summarized in Table 3.1.

It was reported that the standard multistage scheme presented in equation (3.18) suffers from instability [49] if there is a high ratio of pseudo time step to true time step $\Delta t^* / \Delta t$. This is especially true when the local-pseudo time step becomes very large at the cells near far field boundaries. This instability is caused by the unsteady source term of the backward difference formula, and can be stabilized by treating the term implicitly as proposed by Melson [49]. The modification of the point-implicit multistage scheme is presented below

$$\begin{aligned}
\mathbf{Q}^{(0)} &= \mathbf{Q}^{k} \\
&\vdots \\
\mathbf{Q}^{(l)} &= \tfrac{1}{1+\alpha_l \bar{\lambda}} \left[\mathbf{Q}^{(0)} - \alpha_l \Delta t_i^* \tfrac{1}{V_i} \mathbf{R}_i^* \left(\mathbf{Q}^{(l-1)} \right) + \alpha_l \bar{\lambda} \mathbf{R}_i^* \left(\mathbf{Q}^{(l-1)} \right) \right] \qquad (3.21) \\
&\vdots \\
\mathbf{Q}^{k+1} &= \mathbf{Q}^{(m)}
\end{aligned}$$

where $\bar{\lambda} = \frac{3}{2} \frac{\Delta t^*}{\Delta t}$.

The point implicit treatment affects only the equations with true time-derivatives. This affects the momentum equations and possibly the turbulent eddy viscosity transport equation if it is treated in dual time-stepping unsteady form. The continuity equation which does not have the true time-derivative is not affected. Hence, for simplicity, the diagonal preconditioning matrix **P** is omitted in the point implicit multistage formulation shown in Eq. (3.21), since its effect on the momentum equations is the same as that of an identity matrix.

3.8 Time step calculation

The dual-time stepping scheme has two different time steps: the true time step and the pseudo time step. The true time-stepping is discretized by using the A-stable second order backward difference formula. This scheme is stable regardless of the time step size. For the pseudo time-stepping scheme, which is driven by an explicit multistage scheme, a time step calculation formula is needed. Current local pseudo time step is calculated by using both convection and diffusion limits which were originally proposed by Kallinderis [34].

The local pseudo time step for node i is computed by

$$\Delta t_i^* = \omega \frac{V_i}{A_x + A_y + A_z + D} \tag{3.22}$$

where

$$A_x = \left(|u| + c_x\right) S_x$$

$$A_y = \left(|v| + c_y\right) S_y$$

$$A_z = \left(|w| + c_z\right) S_z$$

$$D = 2 \frac{1}{\mathrm{Re}} \frac{V_i}{S_x + S_y + S_z}$$

The artificial speeds of sound in each coordinate direction are given by

$$c_x = \sqrt{u^2 + \beta}$$

$$c_y = \sqrt{v^2 + \beta}$$

$$c_z = \sqrt{w^2 + \beta}$$

and the projected areas of the node-dual volume are defined as follows

$$S_x = \frac{1}{2} \sum_e |S_x|_e$$

$$S_y = \frac{1}{2} \sum_e |S_y|_e$$

$$S_z = \frac{1}{2} \sum_e |S_z|_e$$

where S_x, S_y, and S_z are the components of the area normal vector.

The weighting factor ω may be considered as the local Courant number of the CFL (*Courant, Friedrichs, and Lewy*) condition.

Chapter 4

2D Verification and Validation Study

The proposed Navier-Stokes method is verified and validated for two dimensional applications. Spatial accuracy is verified by a mesh refinement study and temporal accuracy is demonstrated by a time step refinement study. Robustness of the proposed scheme is tested with high aspect ratio cells and small size cells on 2D hybrid meshes. The result is validated by the comparisons with available experimental and computational results.

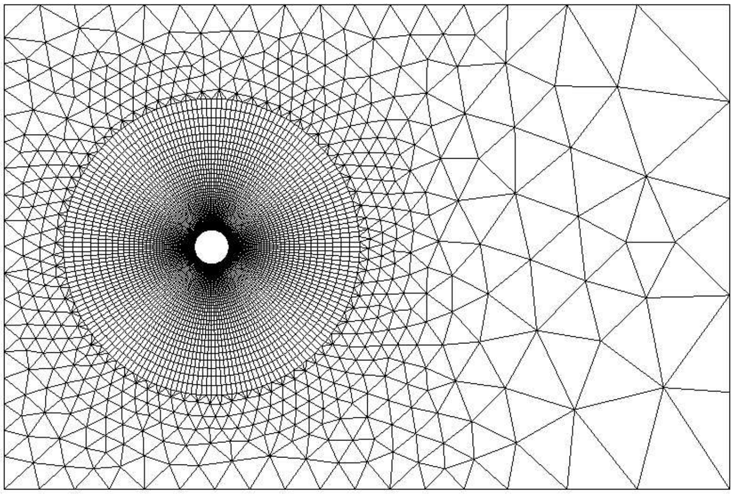

Figure 4.1: 2D Hybrid mesh composed of quadrilaterals and triangles (13,086 nodes and 13,515 elements)

4.1 Computational Meshes

Hybrid meshes have the merits of good viscous layer capturing ability owed to the structured meshes and the flexibility of dealing with complex geometries borrowed from unstructred meshes. However, it is not an obvious task constructing a series of successively refined hybrid meshes. Hence, for the mesh convergence study, polar meshes with O-shape topology are used due to their straightforward way of mesh generation and refinement. For the rest of the simulations, hybrid meshes are used.

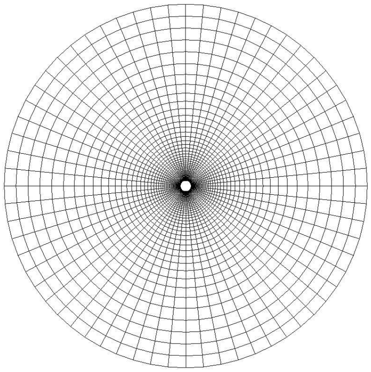

(a) coarse (64x50)

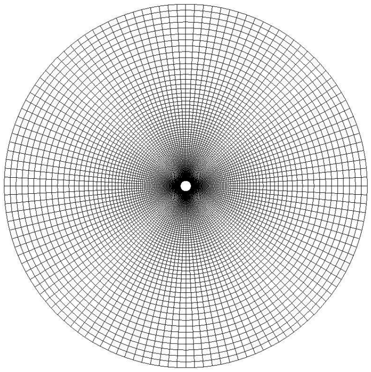

(b) medium (128x99)

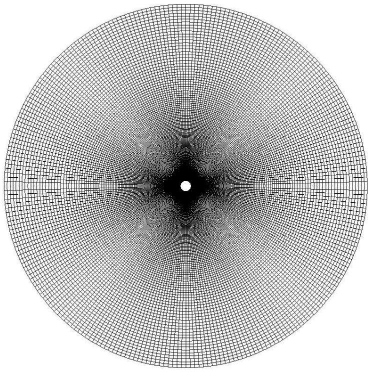

(c) fine (256x197)

Figure 4.2: Three subsequently refined meshes for mesh convergence study

Mesh type	$n_{wall} \times n_{radial}$	Spacing on wall, Δr_0
Coarse mesh	64×50	0.02 diameter
Medium mesh	128×99	0.01 diameter
Fine mesh	256×197	0.005 diameter

Table 4.1: Characteristics of the three O-meshes.

4.2 Mesh Convergence Study

Mesh convergence and spatial accuracy of the presented solution algorithm is verified in two different ways; first the accuracy of the derivative computation is checked by using analytically prescribed flow fields, and second the convergence of the characteristic parameters of flow simulations (C_D, C_L, and St) are verified by solving flow problems over a circular cylinder.

4.2.1 Error analysis about the derivative computations

A simple truncation error analysis is presented about the numerical derivative computations in one dimensional meshes. Three levels of 1-D meshes used for the local truncation error analysis are delineated in Figure 4.3. The initial mesh is generated with uniform stretching ratio α (for example, $\alpha = 1.2$ means 20% of stretching). The medium mesh is obtained by subdividing the original mesh, and the fine mesh is obtained by subdividing the medium mesh.

Taylor series expansions about node i to its two neighbor nodes can be expressed as follows by using the original (level-0) coarse mesh.

$$u_{i+1} = u_i + (\alpha h)(u_x)_i + \frac{(\alpha h)^2}{2!}(u_{xx})_i + \frac{(\alpha h)^3}{3!}(u_{xxx})_i + \cdots \tag{4.1}$$

$$u_{i-1} = u_i + (-h)(u_x)_i + \frac{(-h)^2}{2!}(u_{xx})_i + \frac{(-h)^3}{3!}(u_{xxx})_i + \cdots \tag{4.2}$$

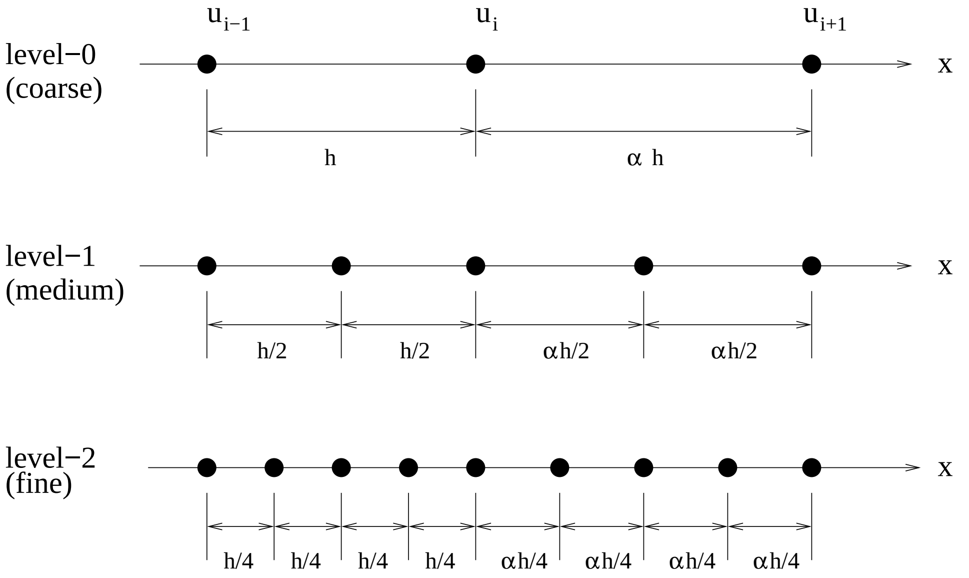

Figure 4.3: Three levels of 1-D meshes. The original level-0 (coarse) mesh is generated with uniform stretching ratio α. The medium mesh is obtained by subdividing the coarse mesh and the fine mesh is obtained by subdividing the medium mesh.

Substracting equation 4.1 from equation 4.2 yields

$$\frac{u_{i+1} - u_{i-1}}{\alpha h + h} = (u_x)_i + \frac{(\alpha^2 h^2 - h^2)}{2!\,(\alpha h + h)}\,(u_{xx})_i + H.O.T.$$

Then the local truncation error at node i for the first order derivative (u_x) computation is

$$(T.E.)_{u_x} = \frac{(\alpha^2 h^2 - h^2)}{2!\,(\alpha h + h)}\,(u_{xx})_i + H.O.T.$$

and by rearranging the leading order term the local truncation error is

$$(T.E.)_{u_x} = (\alpha - 1)\,O\,(h)\,(u_{xx})_i$$

Since the mean stretching halves as the initial mesh is refined by a factor of 2, the average mesh stretching (α_m) and spacing (h_m) for the m-level mesh can be expressed as

$$\alpha_m - 1 = \frac{\alpha_0 - 1}{2^m}$$

$$h_m = \frac{h_0}{2^m}$$

where m refers to the level of refinement. For example, $m = 0$ corresponds to the initial (coarse) mesh, $m = 1$ to the one level refined (medium) mesh, and $m = 2$ to the two level refined (fine) mesh.

Since $\alpha - 1$ halves as the mesh is refined by a factor of two, we have

$$(\alpha - 1) = O\left(h\right) \tag{4.3}$$

hence the local truncation error is

$$(T.E.)_{u_x} = O\left(h^2\right)\left(u_{xx}\right)_i \tag{4.4}$$

By assuming that $\left(u_{xx}\right)_i$ is bounded, the local truncation error for the first order derivative computation is second order.

Likewise, a similar expression can be derived for the second order derivative computation. Multiplying α to equation 4.2 and adding it to equation 4.1 yields

$$\frac{u_{i+1} - (\alpha + 1)\,u_i + \alpha u_{i-1}}{\alpha h \frac{(\alpha h + h)}{2}} = \left(u_{xx}\right)_i + \frac{\left(\alpha^3 h^3 - \alpha h^3\right)}{3!\frac{\alpha h(\alpha h + h)}{2}}\left(u_{xxx}\right)_i + H.O.T.$$

The local truncation error at node i for the second order derivative (u_{xx}) computation is

$$(T.E.)_{u_{xx}} = \frac{\left(\alpha^3 h^3 - \alpha h^3\right)}{3!\frac{\alpha h(\alpha h + h)}{2}}\left(u_{xxx}\right)_i + H.O.T.$$

and by rearranging the leading order term, the local truncation error is

$$(T.E.)_{u_{xx}} = (\alpha - 1)\, O\,(h)\,(u_{xxx})_i$$

Using equation (4.3), the local truncation error for the u_{xx} computation is given by

$$(T.E.)_{u_{xx}} = O\left(h^2\right)(u_{xxx})_i \tag{4.5}$$

With bounded $(u_{xxx})_i$, the local truncation error for the second order derivative computation is also second order.

4.2.2 Analytic field function test

When the analytic solution exists, the error can be computed directly by comparing the numerical solution with the exact solution. For current applications where no exact solution exists, comparison of the results of a few representative differential operators can be used as a measure of spatial accuracy of the current discretization scheme. Two differential operators appearing in the Navier-Stokes equations are chosen to mimic flux computation employed by the flow solver. The divergence operator is chosen to represent the convective flux computation and the Laplacian operator is chosen for the viscous flux evaluation.

In order to measure the error of numerical derivatives of a given vector field, first prescribe an analytical velocity field (hence $u_h = u_{exact}$ already), and then compute numerical derivatives by using the spatial discretization employed, and finally compare the computed derivatives with the exact derivatives.

An analytic velocity field used for the derivative computations is defined by

$$\mathbf{U} = \sin(x)\,\mathbf{i} + \cos(y)\,\mathbf{j}$$

and the error is measured as follows

	Δr_0	$divergence\, Error$	$laplacian\, Error$
coarse	0.02	2.54×10^{-2}	2.73×10^{-2}
medium	0.01	6.97×10^{-3}	7.48×10^{-3}
fine	0.005	1.92×10^{-3}	2.05×10^{-3}

Table 4.2: Errors of derivative computations by using the prescribed analytic velocity field.

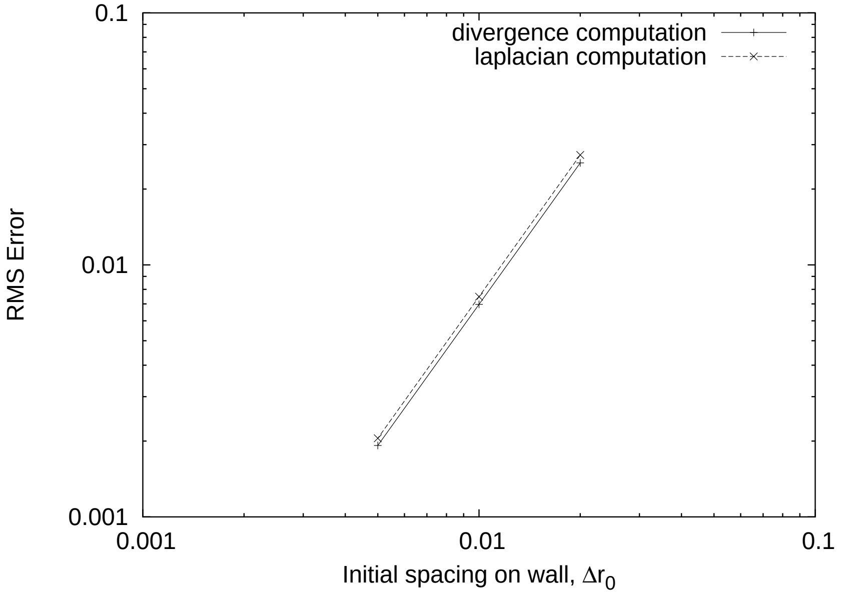

Figure 4.4: Mesh convergence study: Analytic Field Function Test

$$divergence\,Error_{\Delta r} = \sqrt{\frac{\sum_{i=1}^{NI} \left|(\nabla \cdot \mathbf{U})_{\Delta r} - (\nabla \cdot \mathbf{U})_{exact}\right|^2}{NI}}$$

$$laplacian\,Error_{\Delta r} = \sqrt{\frac{\sum_{i=1}^{NI} \left\|(\nabla^2 \mathbf{U})_{\Delta r} - (\nabla^2 \mathbf{U})_{exact}\right\|^2}{NI}}$$

where NI is the number of interior nodes. The actual values of error for the three meshes considered are summarized in Table 4.2 and plotted in Figure 4.4.

The accuracy of derivative computations can be estimated by the technique of Richardson's deferred approach to the limit [66, 7] as follows

$$\log_2 \left(\frac{divergence\,Error_{\Delta r=0.01}}{divergence\,Error_{\Delta r=0.005}} \right) = 1.860$$

$$\log_2 \left(\frac{laplacian\,Error_{\Delta r=0.01}}{laplacian\,Error_{\Delta r=0.005}} \right) = 1.867$$

Both of the derivative computation is nearly second order accurate and this agrees well with the 1D analysis as presented in equations (4.4) and (4.5). The slight discrepancy seems due to the higher spatial dimension.

4.2.3 Unsteady flows around a cylinder

Flow around an impulsively started cylinder is tested for Re = 150. The second order backward difference scheme is used for discretizing the true time-derivative and the time step is fixed to $\Delta t = 0.1$ for all three cases.

Figure 4.5 shows the histories of drag and lift coefficients (C_D and C_L) for three different simulations, and their convergence as the mesh is refined. A detailed comparison of C_D , C_L , shedding period T, and Strouhal frequency St are summarized in Table 4.3.

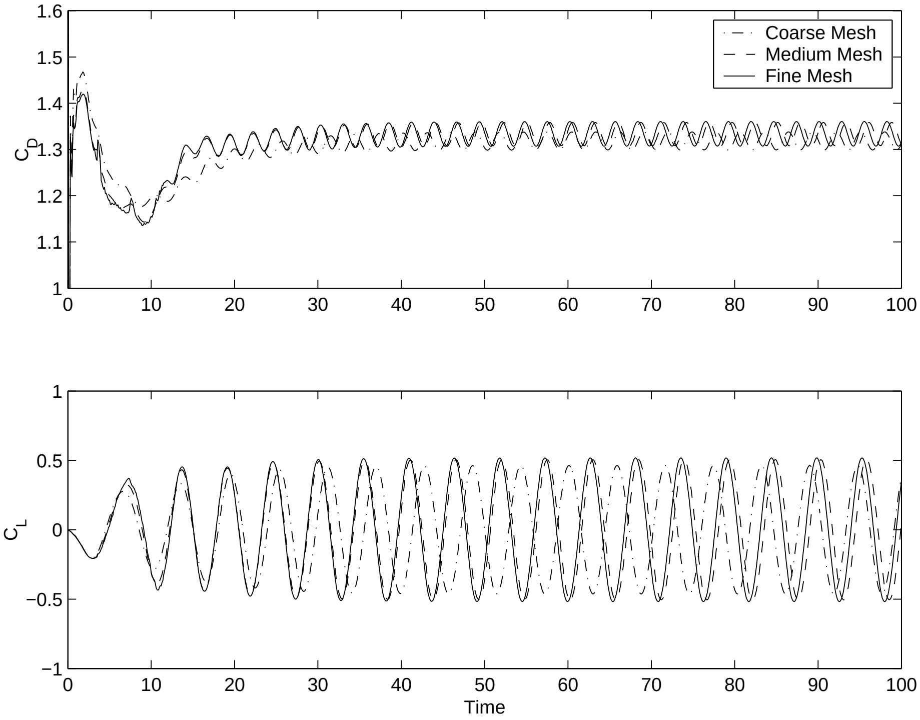

Figure 4.5: Mesh refinement study, $Re = 150$

Mesh type	C_D	C_L	T	St
Coarse mesh	1.3185 ± 0.0195	± 0.462	5.8	0.172
Medium mesh	1.3330 ± 0.0250	± 0.505	5.5	0.182
Fine mesh	1.3335 ± 0.0265	± 0.517	5.4	0.185

Table 4.3: Mesh refinement study for Re = 150

Richardson's extrapolation is used to determine the order of convergence for C_D, C_L , and shedding period T. These parameters are converging nearly in the order of 2.

$$\log_2\left(\frac{\operatorname{amp}(C_D)_{medium}-\operatorname{amp}(C_D)_{coarse}}{\operatorname{amp}(C_D)_{fine}-\operatorname{amp}(C_D)_{medium}}\right)=1.87$$

$$\log_2\left(\frac{\operatorname{amp}(C_L)_{medium}-\operatorname{amp}(C_L)_{coarse}}{\operatorname{amp}(C_L)_{fine}-\operatorname{amp}(C_L)_{medium}}\right)=1.84$$

$$\log_2\left(\frac{(T)_{medium}-(T)_{coarse}}{(T)_{fine}-(T)_{medium}}\right)=2.0$$

4.3 Time Step Refinement Study

A series of three successively halved time steps is used for time step refinement study. The amplitudes of C_D and C_L , and shedding period T are compared to show the convergence and accuracy of the current temporal discretization scheme.

For long term behavior of unsteady simulations, the A-stability is a preferred property of the time integration scheme. A-stability guarantees the solution to be stable regardless of time step size when applied to a linear differential equation. According to the Dahlquist second barrier theorem [15], the second order scheme is the highest order scheme with A-Stability, and the current second order backward difference formula falls in this category.

Time step	C_D	C_L	T	St
$\Delta t = 0.1$	1.3805 ± 0.0275	± 0.561	5.3	0.1886
$\Delta t = 0.2$	1.3785 ± 0.0295	± 0.544	5.4	0.1851
$\Delta t = 0.4$	1.3415 ± 0.0225	± 0.465	5.8	0.1724

Table 4.4: Time step refinement study

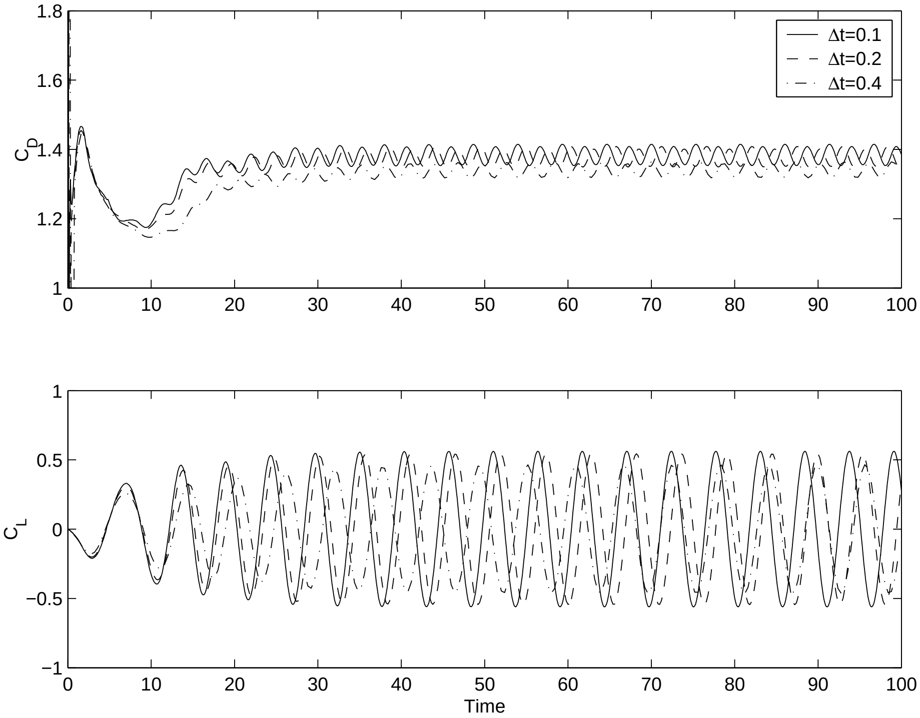

Figure 4.6: Time step refinement study, 2nd order backward difference

The parameters indicating the convergence of the vortex shedding are summarized in Table 4.4. Richardson's extrapolation is used to show the convergence and the order of accuracy of the current temporal discretization scheme.

$$\log_2\left(\frac{\mathrm{amp}\,(C_D)_{\Delta t=0.2}-\mathrm{amp}\,(C_D)_{\Delta t=0.4}}{\mathrm{amp}\,(C_D)_{\Delta t=0.1}-\mathrm{amp}\,(C_D)_{\Delta t=0.2}}\right)=1.80$$

$$\log_2\left(\frac{\mathrm{amp}\,(C_L)_{\Delta t=0.2}-\mathrm{amp}\,(C_L)_{\Delta t=0.4}}{\mathrm{amp}\,(C_L)_{\Delta t=0.1}-\mathrm{amp}\,(C_L)_{\Delta t=0.2}}\right)=2.21$$

$$\log_2\left(\frac{(T)_{\Delta t=0.2}-(T)_{\Delta t=0.4}}{(T)_{\Delta t=0.1}-(T)_{\Delta t=0.2}}\right)=2.0$$

4.4 High aspect ratio cell effect

For viscous flow simulations, it is typical that high aspect ratio cells are located near the viscous wall to capture the development of the boundary layer. These high aspect ratio cells may prevent the proper scaling of the artificial dissipation. In order to check if the current artificial dissipation model can be used for those high aspect ratio cells, two dimensional hybrid meshes are tested and compared with different aspect ratio cells in the viscous region. The close-up views of the two hybrid meshes with different aspect ratio cells are presented in Figure 4.7. The pressure contours on the hybrid meshes are compared in Figure 4.8. Both of the two meshes show smooth and similar patterns of pressure contours around the cylinder, which is supporting the fact that the current individual eigenvalue scaling as presented in Eq. (3.12) can be used with cells of high aspect ratio at least up to 50.

4.5 Small size cell effect

Small size cells are encountered not only in the viscous region but also in the region away from it. These small cells may deteriorate the overall convergence of the solution if time-accurate explicit scheme is used. In the traditional time-accurate explicit scheme, the time steps are scaled by the smallest cell size. If the mesh is successively refined several times, a very small cell can appear even in a region away from the viscous region. The current time-marching scheme is tested on such meshes with small cells in the wake region, in order to show the robustness of the dual time-stepping scheme over the traditional explicit scheme.

Fig. 4.9 shows the comparison of the original and redistributed mesh, where small cells appear in the wake region. These small size cells may lead to overall convergence deterioration if the pseudo time steps of the small cells govern the global convergence rate. This is not the case of the current local pseudo time-

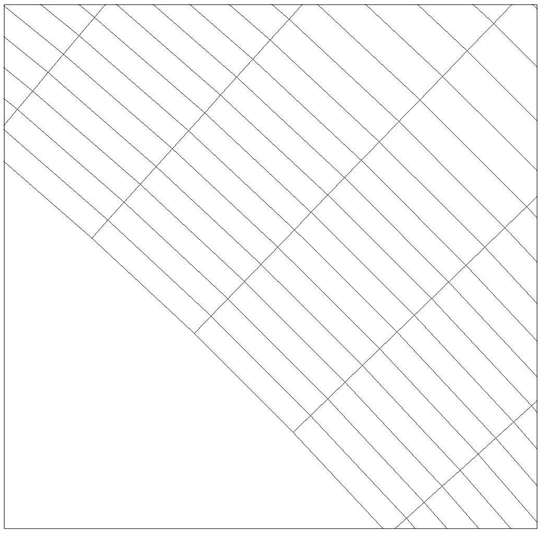

(a) low aspect ratio (AR = 5.8) cells on cylinder ($\Delta r_0 = 0.003$)

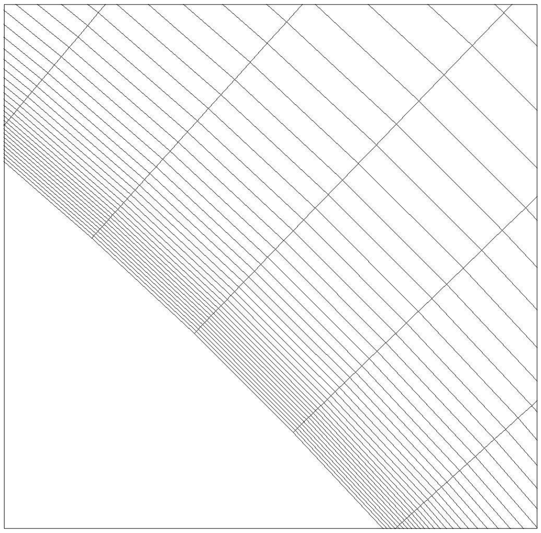

(b) high aspect ratio (AR = 47) cells on cylinder ($\Delta r_0 = 0.000368$)

Figure 4.7: Two dimensional hybrid meshes with different aspect ratio cells on the wall. Δr_0 is the initial mesh spacing on the cylinder surface.

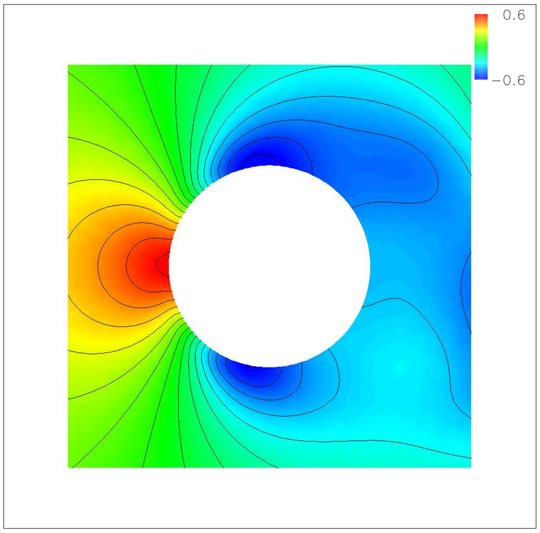

(a) low aspect ratio mesh

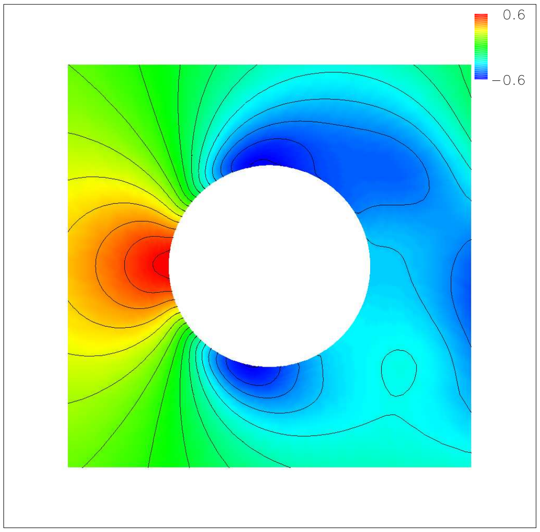

(b) high aspect ratio mesh

Figure 4.8: Pressure contours on 2D hybrid meshes with different aspect ratios; moderate aspect ratio cells on the wall (a), and high aspect ratio cells on the wall (b). Pressure contours are taken approximately at the same time within a shedding cycle.

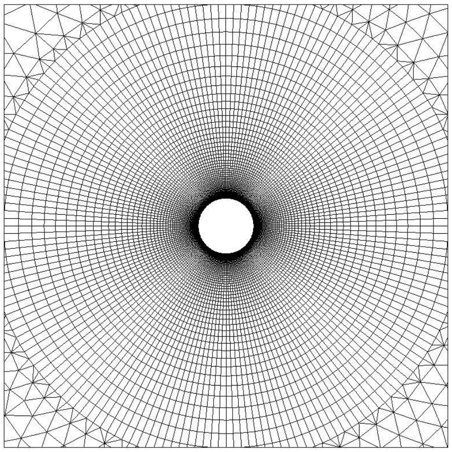

(a) mesh with regular cells

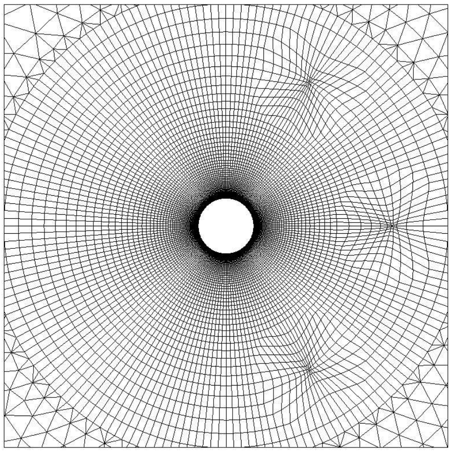

(b) mesh with small cells

Figure 4.9: Two dimensional hybrid meshes with and without small cells in the wake region. (a) the mesh with regular cells and (b) mesh with small cells generated by a mesh redistribution technique.

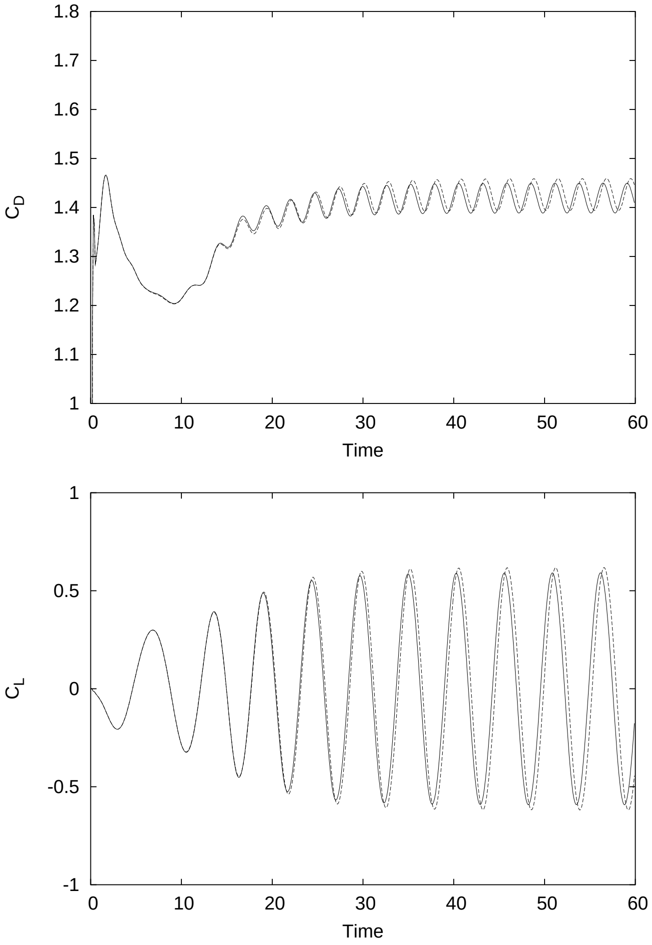

Figure 4.10: Small cell effect on the global solution behavior. The comparison of C_D and C_L histories for the meshes with and without small cells. Solid lines are used for the mesh without small cells, and dashed lines for the mesh with small cells in the wake region.

stepping scheme, since solution at every cell is updated with its own local time step, and this local time step does not affect the time steps of other cells. As shown in Figure 4.10, these small cells in the wake region do not affect the global solution (C_D and C_L) histories. This strengthens the idea that dual time-stepping scheme can be used with meshes of small cells without great sacrifice of convergence or accuracy.

4.6 Convergence Criterion

For implicit unsteady simulations, there should be appropriate convergence criterions to determine solution convergence at each time step. Several different criterions can be used. For example, divergence of the velocity field, maximum or root mean squared (RMS) residuals, or net mass accumulation over the entire computational domain may be the parameter indicating overall solution convergence.

Rogers and Kwak [73] reported that driving maximum divergence of velocity field less than 10^{-3} gives converged solution and this ensures enough accuracy on drag and lift coefficients for the cylinder flow on a structured mesh. In order to be sure about the solution accuracy of the unsteady simulation with hybrid meshes, two different convergence criteria are tested: one is subiterating until the Residual gets under a certain level, and the other pre-specifying the number of subiterations.

For the first creterion, the maximum continuity residual is chosen to be the parameter indicating the overall convergence of solution. Sub-iterations are performed until the maximum continuity residual gets less than 10^{-1}, 10^{-2} , and 10^{-3} . As shown in figure 4.11 the C_D and C_L history indicate a converged result when the maximum residual drops below 10^{-2}.

For the second criterion, as presented in Figure 4.12, a series of different numbers of subiterations (40, 80, and 160) are pre-specified and the results are compared to show the convergence depending on the number of subiterations. A fixed number of subiterations more than 80 shows a converged result in C_D and

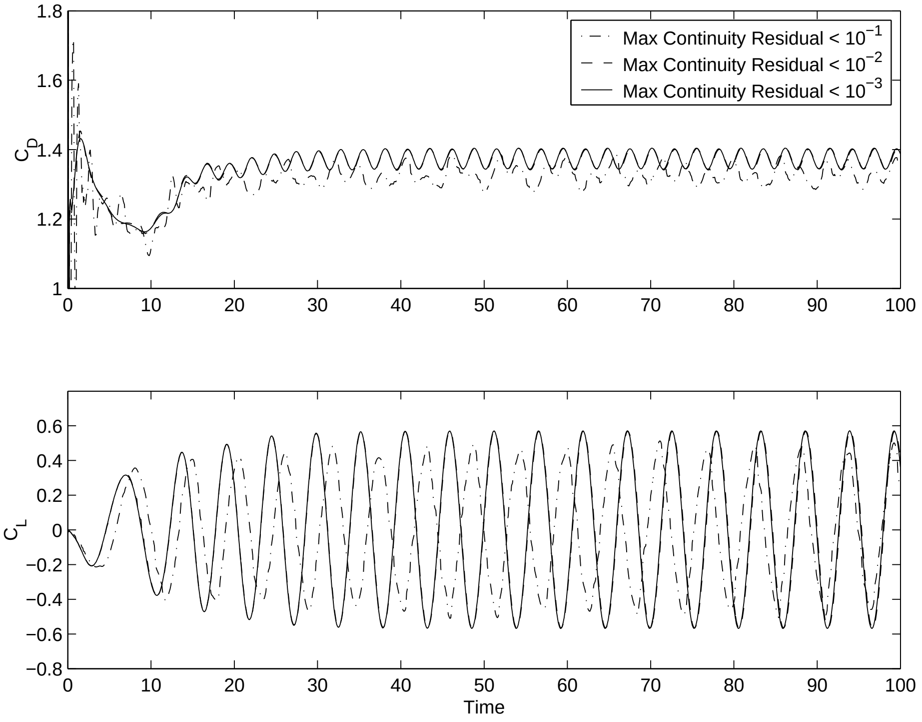

Figure 4.11: Maximum residual sensitivity on solution accuracy

C_L. The maximum continuity residual is presented in figure 4.13 with a series of prescribed subiterations. More than 80 subiterations are enough to drive the maximum continuity residual below 10^{-2} except at the initial stage of the simulation.

Since the cylinder is impulsively started, there is very rapid change of solutions at the initial stage of simulation, and in the initial stage an excessive number of subiterations is required to drop the residual to a certain level. As the simulation progresses, the change of solution is moderate and a fixed number of subiterations can be used to get a converged solution. Therefore, if one is interested only in the periodic shedding stage then a fixed number of subiterations can be specified. If one is interested in the solution change in the initial stage of the simulation, even though the impulsive motion is unrealistic, then the subiterating-to-convergence strategy can be utilized.

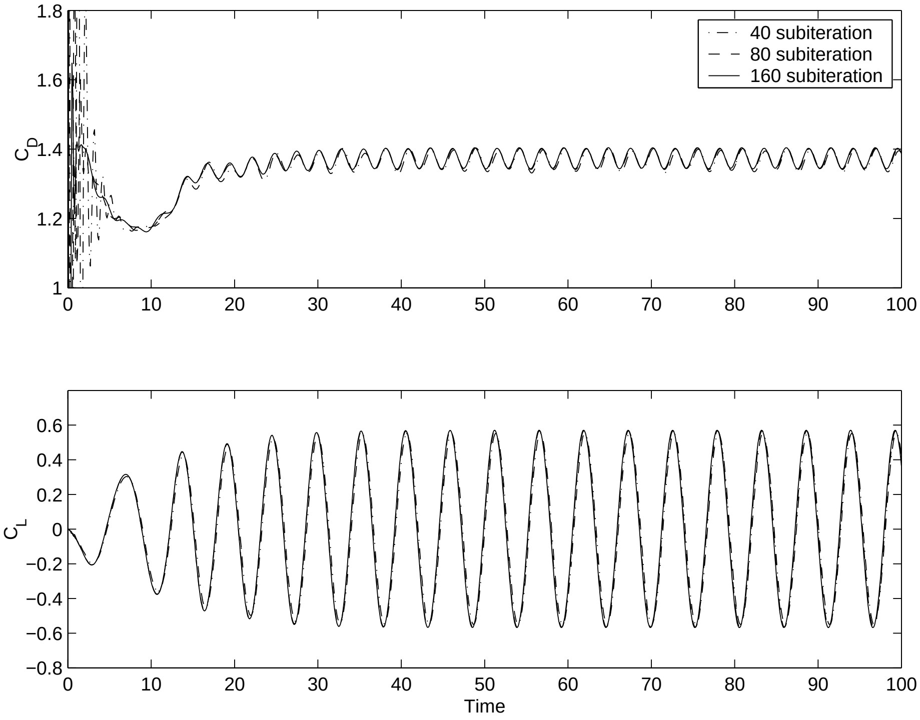

Figure 4.12: Number of subiteration effect on C_D and C_L history

4.7 Early shedding initiation technique

As the Reynolds number goes higher than $40 \sim 50$, the vortices attached behind the cylinder start to shed, and this results in the famous *Karman* vortex street. In physics, vortex shedding is triggered by a small disturbance in the flow field and/or asymmetry in the geometrical shape of the boundary. In numerical simulations, the round-off error of floating point operations is attributed to trigger the shedding. The time needed for the accumulation of the required round-off error can be avoided by some initial disturbance if one is more interested in vortex shedding than the initial

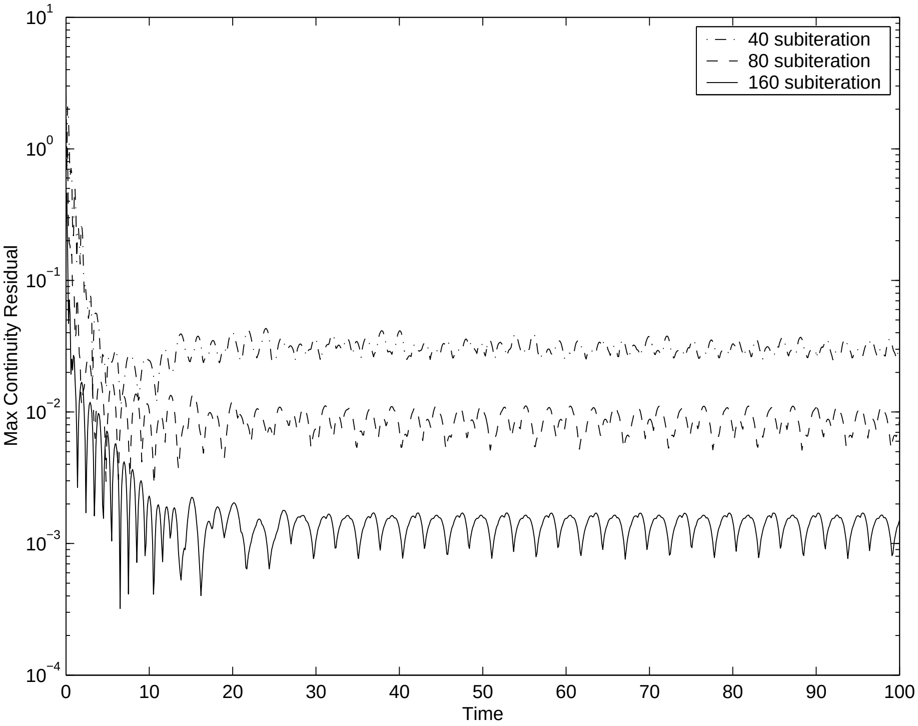

Figure 4.13: Number of subiteration effect on residual decay

stage of the simulation.

For the current study, a rotational disturbance is applied with a sinusoidal function. The maximum amplitude of the tangential velocity on cylinder surface is about 10% of free stream velocity. The rotational disturbance is applied during the nondimensional time $T = 0 \sim 5$ which is approximately one period of shedding. As shown in figure 4.14, the initial disturbance only accelerates the flow field to reach the periodic shedding state, and does not affect the shedding phenomena in the periodic state.

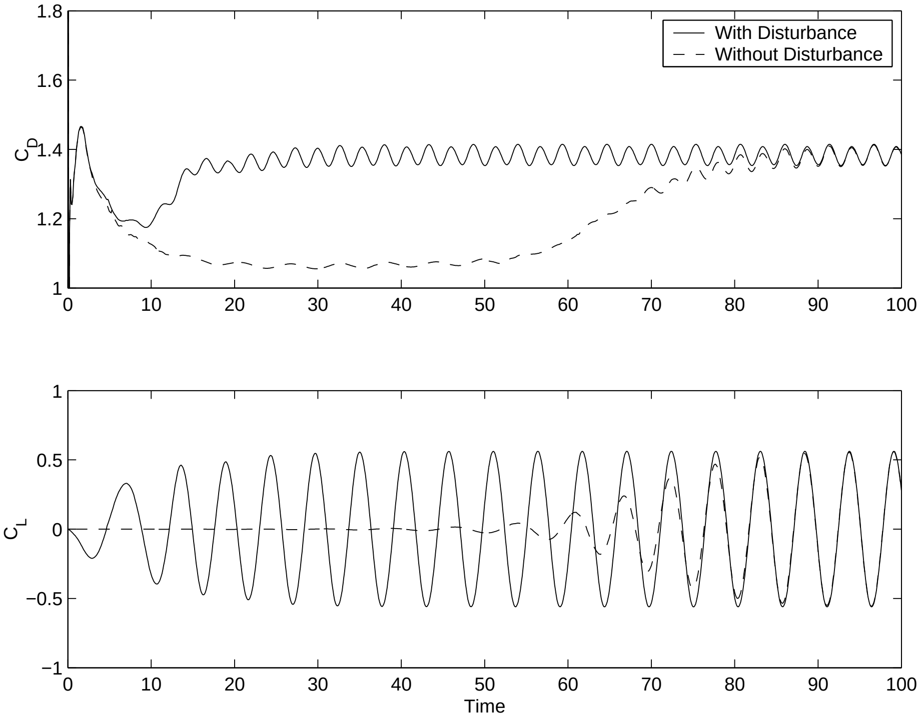

Figure 4.14: Early shedding iniation study

4.8 Comparison with other results

The result of the current simulation is compared with other reported computational and experimental results. Both the hybrid mesh (180 nodes on wall, and 13,086 nodes total) and the fine polar mesh (256x197 nodes) is used for this comparison study. The second order backward difference formula with time step $\Delta t = 0.1$ is used for both cases. The C_D, C_L, and St are chosen for the parameters of comparison and the details are presented in Table 4.5.

The results of Belov [6] and Lin [42] are obtained with a computation based on the artificial compressibility method in two dimensions. Belov used a structured polar mesh (257x257 nodes), and Lin used an unstructured mesh only with triangles

	C_D	C_L	St
Hybrid mesh	1.380 ± 0.027	± 0.561	0.188
Polar mesh	1.333 ± 0.026	± 0.517	0.185
Belov [6]	1.168 ± 0.025	± 0.486	0.182
Lin [42]	1.166 ± 0.023	± 0.477	0.182
Experiment-1 [97]	*N.A.*	*N.A.*	0.183
Experiment-2 [67]	1.328	*N.A.*	*N.A.*

Table 4.5: Comparison with other computational and experimental results. Hybrid mesh and polar mesh results are from the current simulations with $\Delta t = 0.1$. The fine mesh (256x197) is used for the the polar mesh result. Belov's result is obtained with a 2D structured polar mesh, and Lin's result is obtained with 2D unstructured mesh only with triangles. Experiment-2 is for $Re = 152$, and the rest for $Re = 150$.

(128 nodes on wall, and 42,200 nodes total).

Overall, the current simulation result agrees well with the compared computational and experimental results. Especially for the C_D values, the current simulation gives better agreement with the reported experimental result [67]. The snap shots of the vortex shedding for $Re = 150$ over a single period are presented in Figure 4.15 for stream lines, Figure 4.16 for vorticity, Figure 4.17 for pressure, and Figure 4.18 for u-velocity fields.

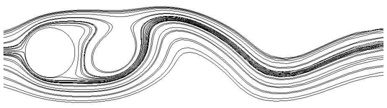

(a) Time = 80

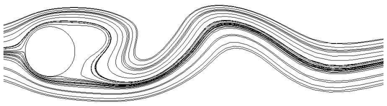

(c) Time = $80 + \frac{1}{4}T$

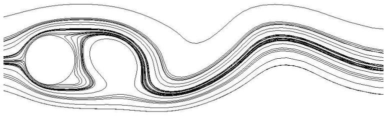

(e) Time = $80 + \frac{2}{4}T$

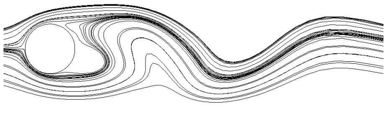

(g) Time = $80 + \frac{3}{4}T$

Figure 4.15: Stream lines over a shedding cycle. $Re = 150$ with the 2D hybrid mesh.

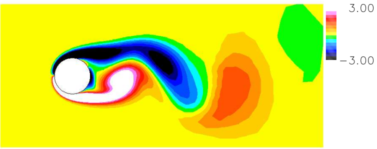

(a) Time = 80

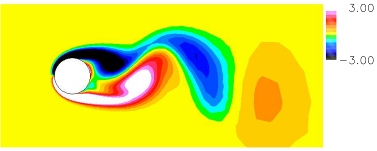

(c) Time = $80 + \frac{1}{4}T$

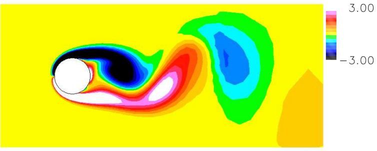

(e) Time = $80 + \frac{2}{4}T$

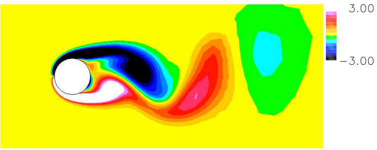

(g) Time = $80 + \frac{3}{4}T$

Figure 4.16: Vorticity fields over a shedding cycle. $Re = 150$ with the 2D hybrid mesh.

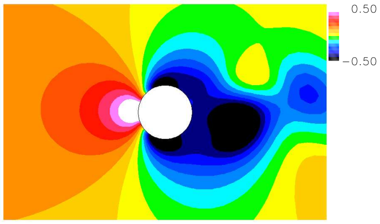

(a) Time = 80

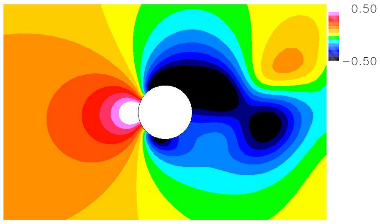

(c) Time = $80 + \frac{1}{4}T$

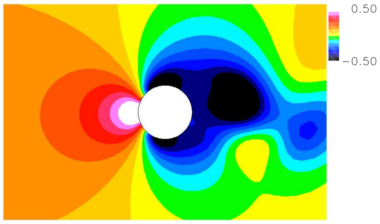

(e) Time = $80 + \frac{2}{4}T$

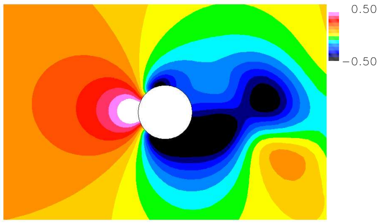

(g) Time = $80 + \frac{3}{4}T$

Figure 4.17: Pressure fields over a shedding cycle. $Re = 150$ with the 2D hybrid mesh.

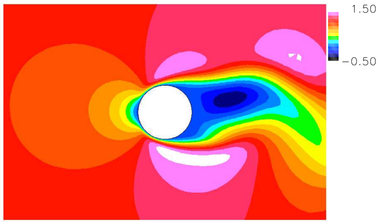

(a) Time = 80

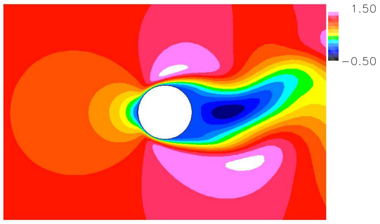

(c) Time = $80 + \frac{1}{4}T$

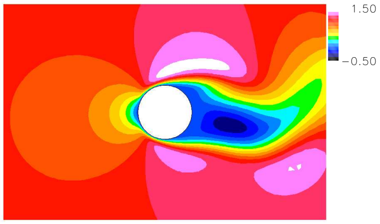

(e) Time = $80 + \frac{2}{4}T$

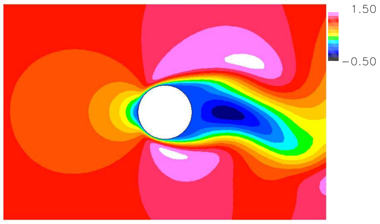

(g) Time = $80 + \frac{3}{4}T$

Figure 4.18: u-velocity fields over a shedding cycle. $Re = 150$ with the 2D hybrid mesh.

Chapter 5

Inflow Turbulence Study

The purpose of this chapter is to investigate the effect of inflow turbulence on flows around a circular cylinder in two dimensions using the incompressible Navier-Stokes method which was developed and validated in previous chapters.

Two different flow conditions are tested: one for low Reynolds number ($Re = 150$) and the other for moderate Reynolds number ($Re = 1,000$). The effect of inflow turbulence is demonstrated with comparisons to the uniform inflow cases. A local mesh refinement study is presented to show the effect of mesh resolution regarding capturing inflow turbulent eddies. The mesh refinement effect on turbulent vortex shedding is further emphasized by a frequency analysis of the hydrodynamic responses.

5.1 Significance of inflow turbulence

Turbulent flows are present everywhere. Especially, the inflow ocean turbulent effects on offshore structures are of high interest due to the lack of information about its role regarding the hydrodynamic forces and fatigue load on structures. If the inflow condition is changed from uniform to turbulent, the flow condition around the structure will be completely different from that of uniform inflow. For example, an airplane with turbulent inflow typically suffers strong vibration and noise due to the non-uniform inflow. This is also happening in the offshore structures exposed to the ocean current which can be turbulent. The difference of the two cases is the model of flow around the structure: typically flow around airplane is modeled as compressible flow (except very low Mach number flow), hence it is called as aero-elasticity problem, but the flow around offshore structure is incompressible, hence it can be termed as the hydro-elasticity. The structural model in this chapter is fixed however, in order to first investigate the effect of inflow turbulence on the hydrodynamic force exerted on the structure, without considering the inertia effect of the structure.

Two different inflow turbulence profiles (Re=150 and Re=1000) are prepared by an isotropic geophysical turbulence model [50]. These turbulence profiles are specified as the inflow condition for the current numerical simulations over a circular cylinder, our representative offshore structure.

5.2 Unsteady turbulent flow simulations using an eddy viscosity model

Applying a turbulent eddy viscosity transport model to unsteady turbulent flow problems may be arguable, however the eddy viscosity model approach is still among the very few methods which are feasible with the computing power of moderate scale.

Since its first introduction in 1992, the Spalart-Allmaras one-equation model, chosen for the current turbulent flow simulation, has been proven to give reasonable results with inexpensive computational cost compared to other more computationally expensive approaches, such as two-equation models, Reynolds stress model, detached eddy simulations, large eddy simulations, or direct numerical simulations.

5.3 Inlet turbulent velocity profiles

In order to study free stream turbulence effects on the flows around a cylinder, a turbulent velocity profile is to be prescribed at the inlet instead of the uniform velocity profile. The 2D turbulent velocity profile is obtained by a slice of velocity field from the 3D velocity field. The 3D velocity field is generated by spatial realizations of frozen isotropic homogeneous turbulence for a given computational grid [50].

The homogeneous turbulence means its fluctuating velocity $\mathbf{u}(\mathbf{x}, t)$ is statically homogeneous (invariant under translations). An approximation of homogeneous turbulence can be achieved in wind-tunnel experiments by passing a uniform stream through a grid with regular spacing. If the flow field is statically invariant under rotations and reflections of the coordinate system, then it is isotropic. Hundreds of wind-tunnel experiments have been performed on isotropic turbulence, and much of the turbulence theory is based on it [65].

Time series of inlet turbulent profiles ($u = U + u'$, $v = V + v'$) are displayed in Figure 5.1 for $Re = 150$ and in Figure 5.3 for $Re = 1,000$. Generally, the higher Reynolds number case shows higher amplitude and frequencies of the fluctuations and also wider variances of the fluctuations in space (from nodes to nodes) compared to the lower Reynolds number case.

5.4 Boundary conditions for inflow turbulence simulations

In 2D simulations, the boundaries are classified as inlet, outlet, viscous wall, and far field parallel to the mean flow direction. As the inlet velocity profile changes from the uniform to the irregular turbulent, boundary conditions (inlet and far field) have to be modified accordingly for both of the mean flow equations and the turbulence equation solvers.

For the uniform inflow case, the velocities at the far fields are considered uniform. This is no longer valid for turbulent inflow case, since the turbulent eddies are everywhere even at the far fields. Hence, for the turbulence inflow simulations, the velocities at the far fields are extrapolated from the domain as the pressure is. Likewise, turbulent eddy viscosity is also extrapolated from the domain along the far field boundaries. At the inlet, the given turbulent velocity profile is specified instead of the uniform velocity, while the pressure is extrapolated just as in the uniform inlet case.

For the turbulent transport equation solver, the inlet boundary requires special attention. The instantaneous inlet turbulent velocity profile (u_i) is already equipped with the homogeneous isotropic turbulent fluctuations (u_i'), and those are defined by

$$u_i\left(\mathbf{x},t\right) = U_i\left(\mathbf{x},t\right) + u_i'\left(\mathbf{x},t\right) \tag{5.1}$$

where i denotes each coordinate direction. The mean velocity components are defined as follows

$$U_i\left(\mathbf{x}\right) = \lim_{T\to\infty}\frac{1}{T}\int_t^{t+T} u_i\left(\mathbf{x},t\right)dt$$

and this is uniform everywhere and spatially invariant. Hence, the strain rate tensor of the mean velocity field is equal to zero at the inlet.

$$S_{ij} = \frac{1}{2}\left(\frac{\partial U_i}{\partial x_j} + \frac{\partial U_i}{\partial x_j}\right) = 0 \tag{5.2}$$

In order to calculate the eddy viscosity corresponding to a given turbulent fluctuation, the eddy viscosity hypothesis (Boussinesq approximation) has to be used. This hypothesis relates the Reynolds stresses ($-\overline{u_i'u_j'}$) with the *non-zero* strain rate tensor (S_{ij}), which is defined by

$$-\rho\overline{u_i'u_j'} = 2\rho\nu_t S_{ij} \tag{5.3}$$

Since our mean velocity is uniform, the strain rate tensor S_{ij} of the mean velocity is also zero, which contradicts the eddy viscosity hypothesis. Hence, the eddy viscosity of the turbulent fluctuation cannot be determined for uniform mean flow.

By this contradition a question arises; should the eddy viscosity be non-zero, even if the mean flow is uniform? The answer is no, because by specifying the turbulent velocity profiles at the inlet, the turbulent fluctuation is fed to the mean flow solver. The effect of turbulence is accounted by the mean flow equations, and no additional eddy viscosity is necessary at the inlet. Hence, eddy viscosity at the inlet should be ideally zero, otherwise the effect of inflow turbulence will be doubly counted and contaminated by the non-zero eddy viscosity.

Nevertheless, the hydrodynamic foces exerted on the cylinder are relatively insensitive to the values of eddy viscosity at the inlet. The reason is that the amount of eddy viscosity at the upstream is a few orders of magnitude smaller than that in the near wall region. Hence, we can specify the eddy viscosity at the inlet to be the same as that of uniform inflow. However, regardless of the values of eddy viscosity at the inlet, as the flow goes down stream the flow becomes non-uniform even in the mean-sense, and the Spalart-Allmaras turbulence model detects this and adjusts the eddy viscosity accordingly.

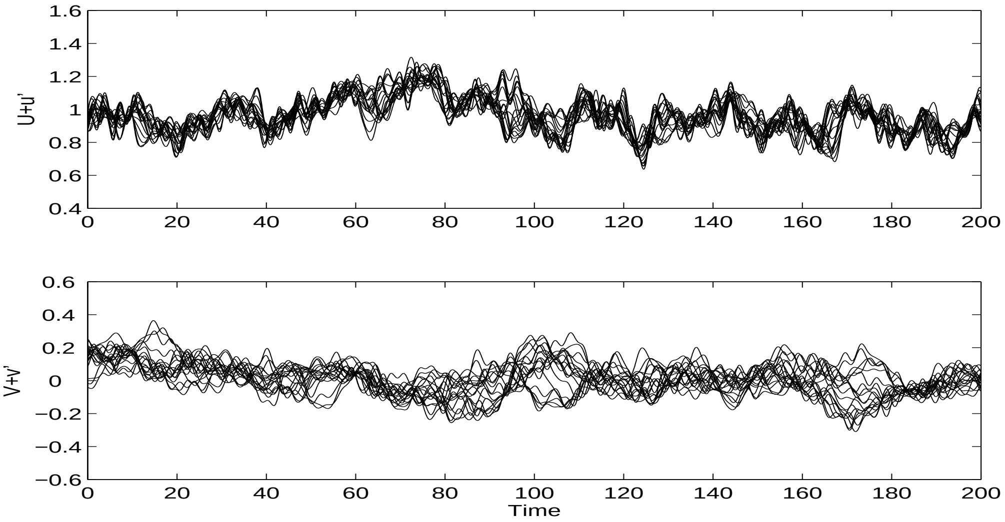

Figure 5.1: Turbulent velocity profile at the inlet nodes, $Re = 150$

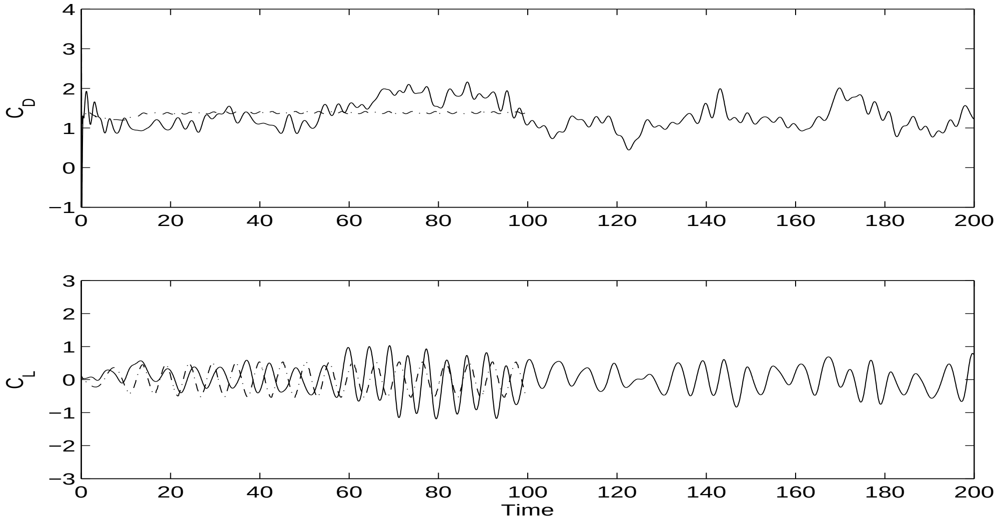

Figure 5.2: C_D and C_L responses to the turbulent and uniform inflow, $Re = 150$. Solid lines are for turbulent inflow, and dash-dotted lines for uniform inflow.

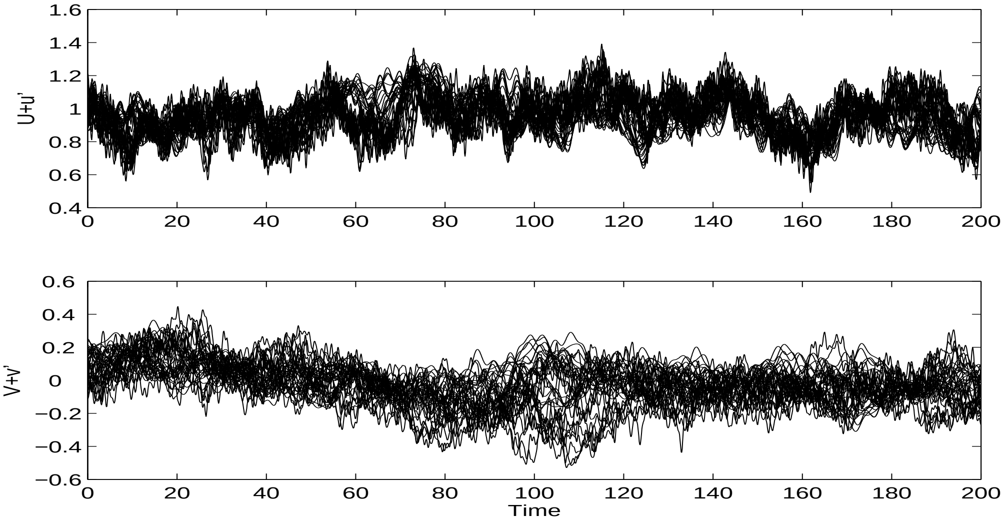

Figure 5.3: Turbulent velocity profile at the inlet nodes, $Re = 1000$

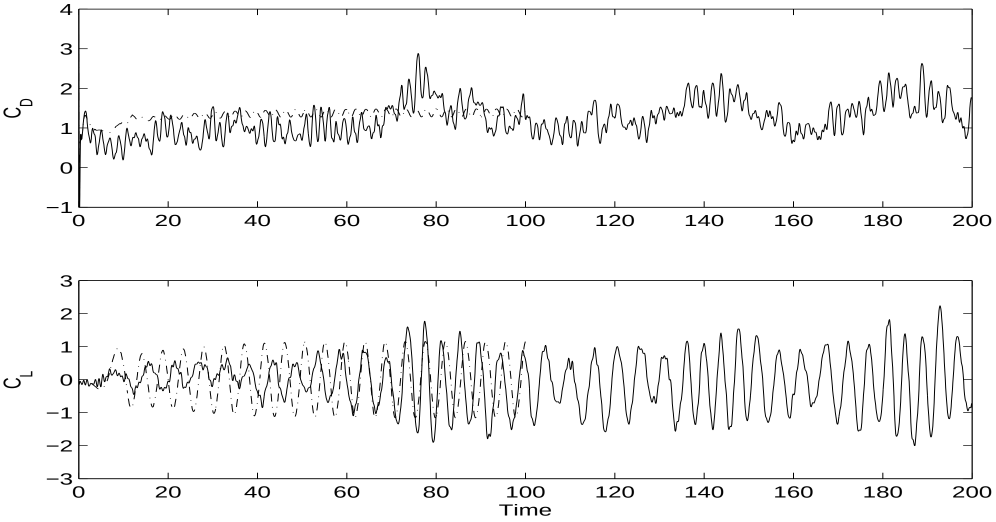

Figure 5.4: C_D and C_L responses to the turbulent and uniform inflow, $Re = 1000$. Solid lines are for turbulent inflow, and dash-dotted lines for uniform inflow.

5.5 C_D and C_L responses to inflow turbulence

The effect of inflow turbulence on the hydrodynamic forces exerted on the cylinder is presented in Figure 5.2 for $Re = 150$ and Figure 5.4 for $Re = 1,000$, and they are compared with those of the uniform inflow case.

As is evident from Figures 5.1- 5.4, when the inflow turbulence is applied, *the time series of the drag coefficient usually (not always) follows the time series of the inflow u-velocity.* Furthermore, higher values of C_D are always accompanied with higher amplitudes of C_L and faster shedding frequencies.

However, there is an exception which does not follow this trend. Especially in the region of $Time = 100 \sim 120$ for $Re = 1,000$, both the C_D and the amplitudes of the C_L decrease even though the inflow u-velocity increases. In such region ($Time = 110 \sim 120$), a wide variances of inflow v-velocity is observed in the inflow turbulence profile, and their relation (variances of inflow v-velocity and diminishing of vortex shedding) is uncertain at this time and of interest for further investigation.

The general trends of the drag and lift coefficient to the inflow turbulence profile can be summarized as below.

1. The stronger inflow u-velocity, the higher C_D.
2. The higher C_D accompanies the higher amplitudes of C_L and St.
3. When shedding diminishes even with increase of inflow u-velocity, a wide variance of inflow v-velocity is observed.

5.6 Local mesh refinement effect

Since the local mesh spacing determines the smallest scale of turbulent eddies which can be resolved, enough resolution of mesh has to be assured for accurate simulation of inflow turbulence.

For the $Re = 150$ case, the cylinder diameter is about 10 times smaller than the integral length scale of the upstream turbulence, which is a length scale characterizing coherence of the fluctuations. For this case, grid spacing at the inlet boundary is smaller than the cylinder diameter, so the resolution of the computational grid is deemed to be fine enough to capture the smallest eddies.

For higher Reynolds number ($Re = 1,000$), the scales of the upstream turbulent eddies are getting smaller, so the computational grid near the inlet may need to be refined in order to resolve these smaller scales of eddies. To see the mesh resolution effect on inflow turbulence simulations, the large triangular cells which are located away from the wall are refined. Each triangular cell is divided into four child triangles. The one-step adapted mesh is compared with the original mesh in Figure 5.6.

The mesh refinement effect on the C_D and C_L responses is compared in Figure 5.7 for $Re = 150$ and in Figure 5.8 for $Re = 1,000$. For $Re = 150$, the adapted mesh simulation shows almost identical result to the original mesh simulation. This tells that the original mesh is fine enough to resolve most of the turbulent eddies which are significant to the drag and lift response of the structure. But for Re = 1000, there is a noticeable difference in the drag and lift responses between the adapted and original mesh results. Especially in the fluctuations of the drag and lift coefficients, more frequencies are encountered by the adapted meshes than the original mesh. This extra frequencies in the drag and lift seems to be the direct effect of the smaller scales of eddies which are resolved by the refined mesh. The vorticity fields at a series of time steps are presented in Figure 5.9 for $Re = 150$ and in Figure 5.10 for $Re = 1,000$ to show the transport of the turbulent eddies. It is obvious that the adapted mesh resolves much smaller scales of eddies.

Finally, frequency responses to inflow turbulence are presented. The uniform inflow case is first examined as a reference. In general, the inflow turbulence introduces more frequencies and the shedding frequencies spread in wider ranges; some frequencies faster than that of the uniform inflow, and others slower than that.

The details of the frequency analysis are presented in figure 5.11 for $Re = 150$ and figure 5.12 for $Re = 1,000$. For the Re = 150 case, the frequency responses are almost the same and insensitive to mesh refinement, which means that the original mesh resolves most of the eddies that are significant to the vortex shedding. However, for the Re = 1000 case, the frequency analysis of the adapted mesh simulation reveals more frequencies which were not resolved by the original mesh simulation. This indicates that the refined mesh is resolving more small scales of turbulent eddies and these small eddies result directly in the extra frequencies of shedding.

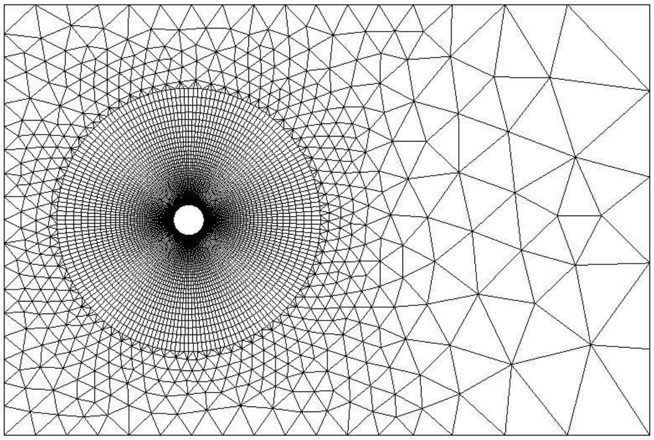

(a) original 2D hybrid mesh (13,086 nodes 13,515 elements)

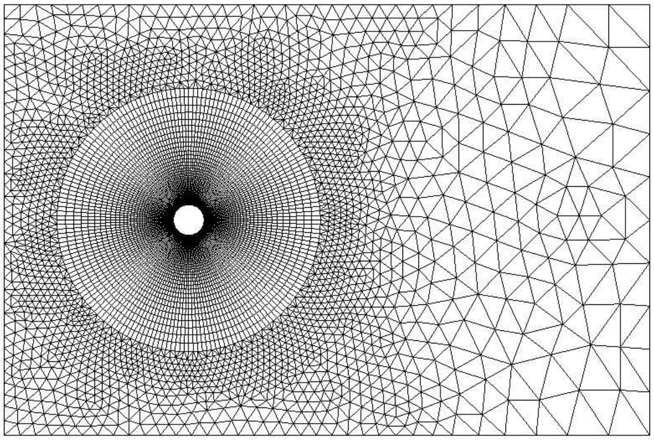

(b) locally refined 2D hybrid mesh (14,412 nodes, 16,110 elements)

Figure 5.5: Local mesh refinement in the outer triangular region

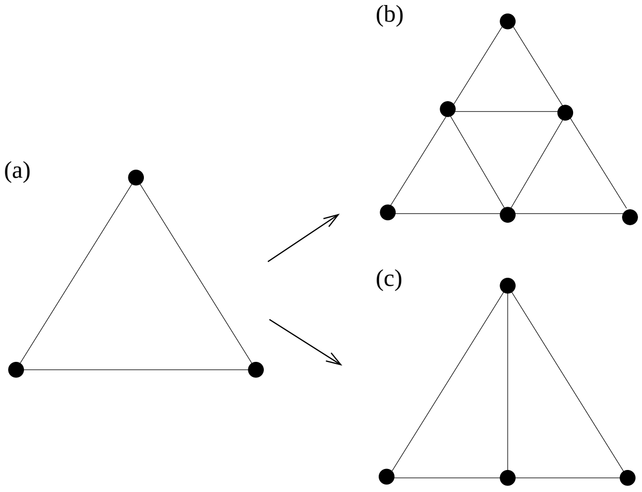

Figure 5.6: Division types for triangular elements without hanging nodes. (a) original cell, (b) isotropic division, (c) anisotropic division which is used only at the transitional regions between the triangular and quadrilateral.

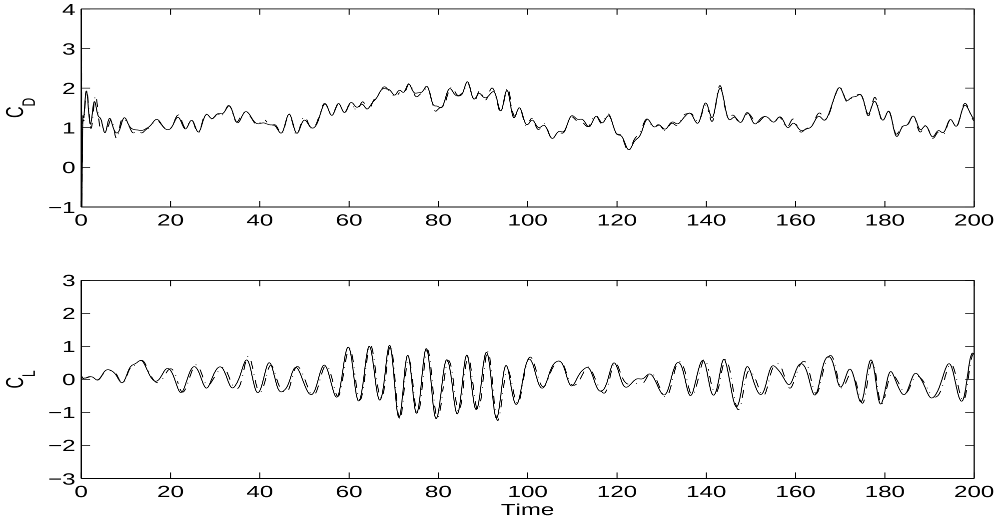

Figure 5.7: Mesh adaption effects on C_D and C_L responses, $Re = 150$. Solid lines for original mesh, and dash-dotted lines for refined mesh.

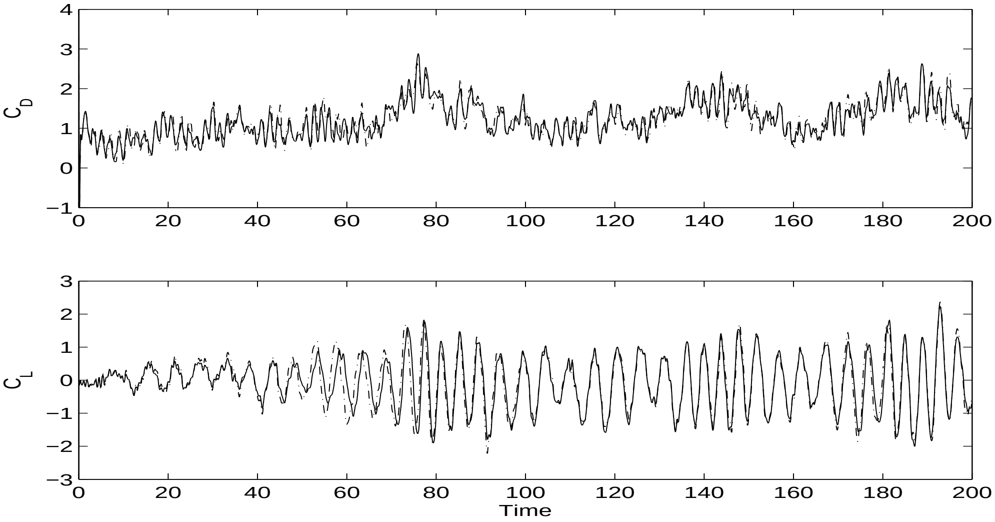

Figure 5.8: Mesh adaption effects on C_D and C_L responses, $Re = 1000$. Solid lines for original mesh, and dash-dotted lines for refined mesh.

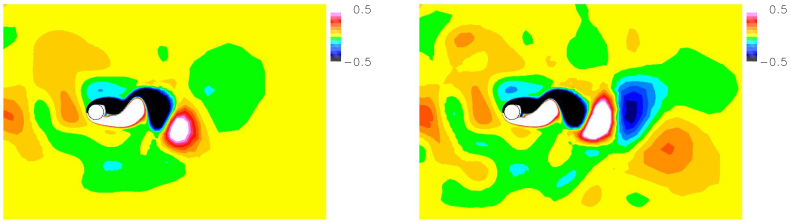

(a) Time = 60, original mesh (b) Time = 60, refined mesh

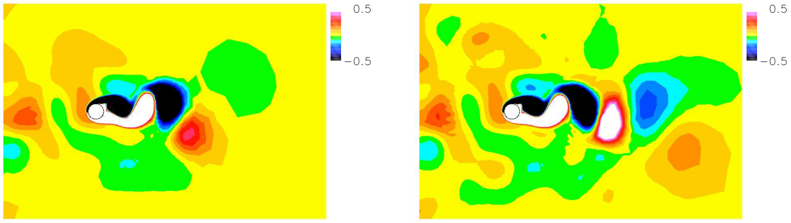

(c) Time = 61, original mesh (d) Time = 61, refined mesh

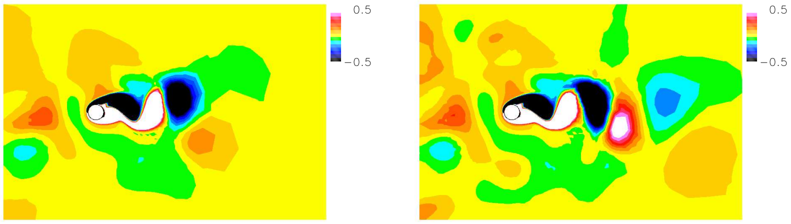

(e) Time = 62, original mesh (f) Time = 62, refined mesh

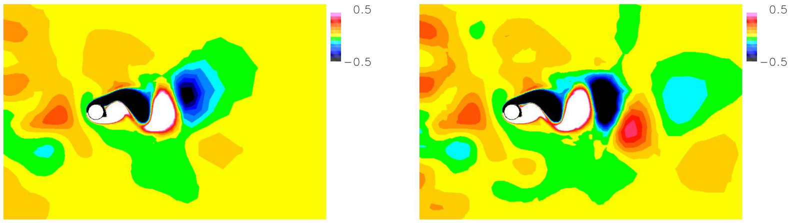

(g) Time = 63, original mesh (h) Time = 63, refined mesh

Figure 5.9: Vorticity transport with inflow turbulence, Re = 150

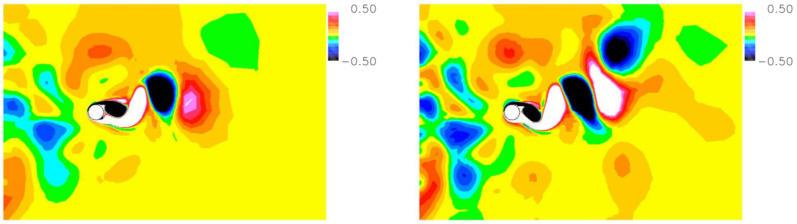

(a) Time = 40, original mesh (b) Time = 40, refined mesh

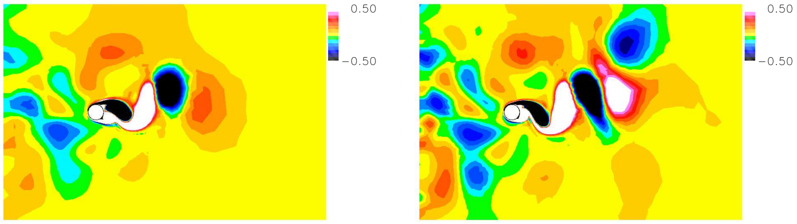

(c) Time = 41, original mesh (d) Time = 41, refined mesh

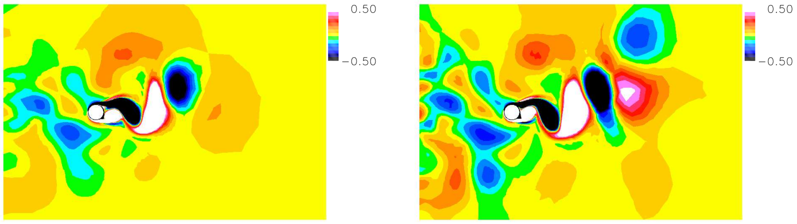

(e) Time = 42, original mesh (f) Time = 42, refined mesh

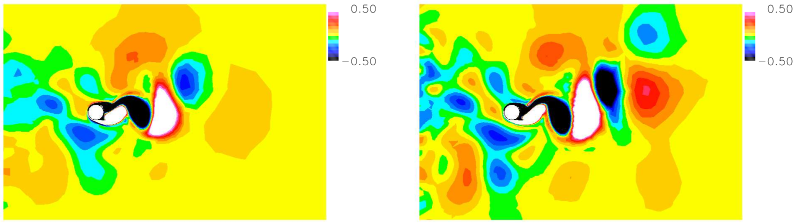

(g) Time = 43, original mesh (h) Time = 43, refined mesh

Figure 5.10: Vorticity transport with inflow turbulence, Re = 1000

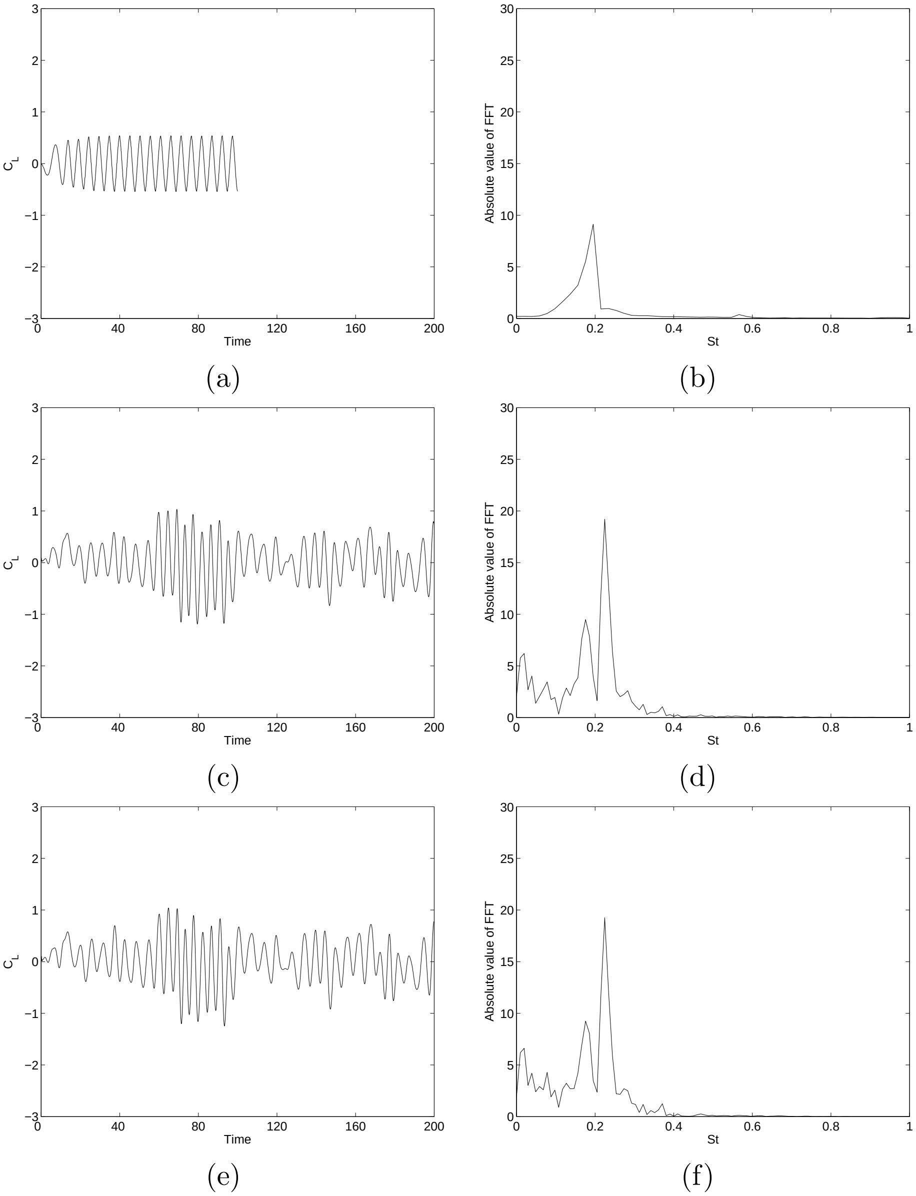

(a) (b)

(c) (d)

(e) (f)

Figure 5.11: FFT spectrums of C_L responses for Re = 150. (a) and (b) correspond to the uniform flow using original mesh; (c) and (d) correspond to the turbulent flow using original mesh; (e) and (f) correspond to the turbulent inflow using adapted mesh, which is showing almost idential result with the original. Same time step $\Delta t = 0.1$ is used for all cases.

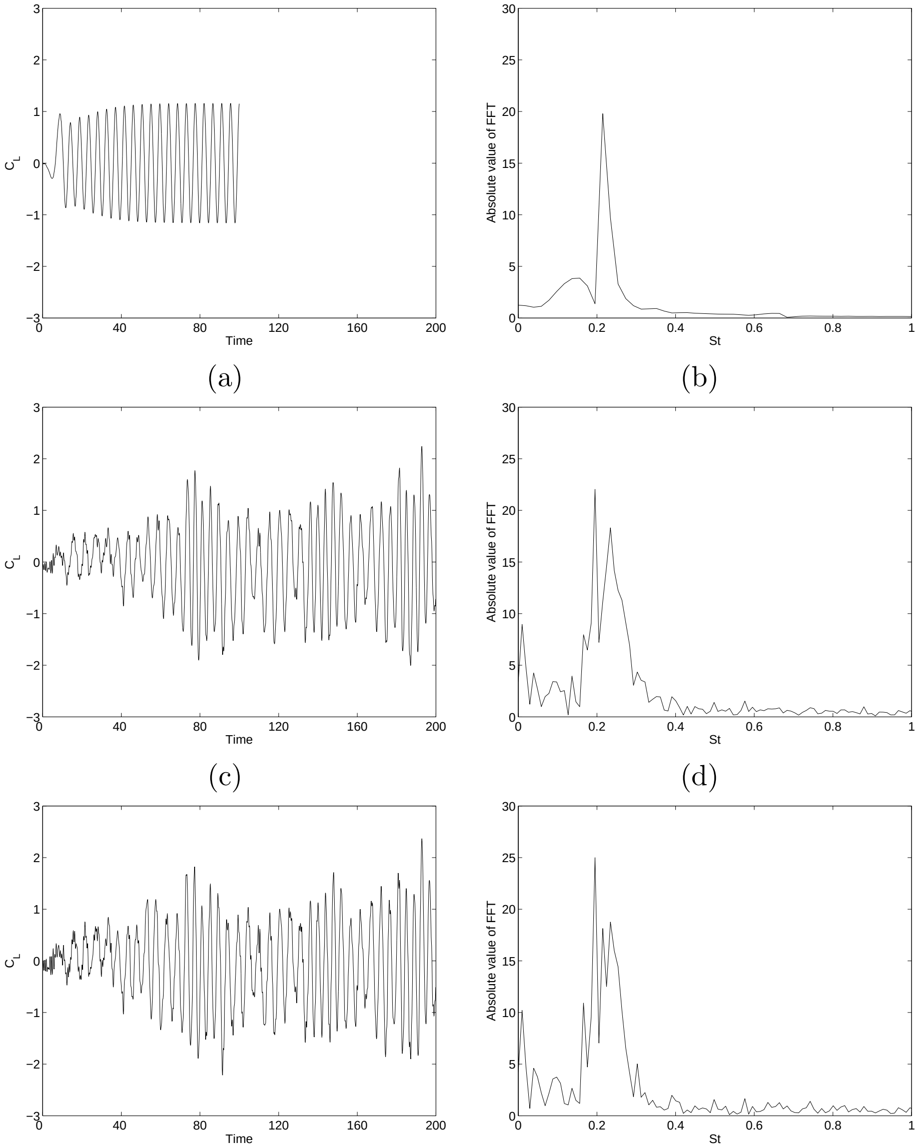

(a) (b)

(c) (d)

(e) (f)

Figure 5.12: FFT spectrums of C_L responses for Re = 1000. (a) and (b) correspond to the uniform flow using original mesh; (c) and (d) correspond to the turbulent flow using original mesh; (e) and (f) correspond to the turbulent inflow using adapted mesh, which is showing extra peaks other than the ones resolved by the original mesh simulation. Same time step $\Delta t = 0.1$ is used for all cases.

Chapter 6

3D Verification and Validation Study

Verification and validation of the developed Navier-Stokes method is presented in three dimensions with general hybrid meshes. Flows around a sphere and a cylinder are simulated and the results are compared with reported experimental measurements. A mesh convergence study is performed using a series of successively refined sphere meshes. A wide range of Reynolds numbers ($100 \sim 1,000,000$) is tested for validation of the numerical solution using both the sphere and cylinder problems. Validity and effectiveness of local hexahedra is presented with general hybrid meshes which contain local hexahedra in various regions of the computational domain.

6.1 Mesh convergence study

A set of three successively refined meshes around a sphere are constructed for a mesh convergence study. A triangular surface mesh over the sphere is first generated and the surface mesh is extruded along the radial directions with a uniform stretching of 20%. The outer boundary is located about 17 diameters away from the center of the sphere. In order to get a one-step refined mesh, each prismatic cell is subdivided into eight prisms (each surface triangle divided into four surface triangles and each lateral edge is divided into two edges), therefore refining the mesh once produces a mesh containing eight times as many cells as the original. This procedure is repeated twice to construct three successively refined meshes. The detailed characteristics of the resulting meshes are summarized in Table 6.1.

	nodes	elements	initial spacing on wall, Δr_0
coarse	162 x 33	320 x 32	0.01
medium	642 x 65	1280 x 64	0.005
fine	2562 x 129	5120 x 128	0.0025

Table 6.1: Characteristics of the initial (coarse), once (medium) and twice (fine) refined sphere meshes

Mesh convergence tests are performed in two different ways; first we compute two representative differential operations using a prescribed analytic velocity field and second we measure the drag coefficients from the flow simulations around the sphere.

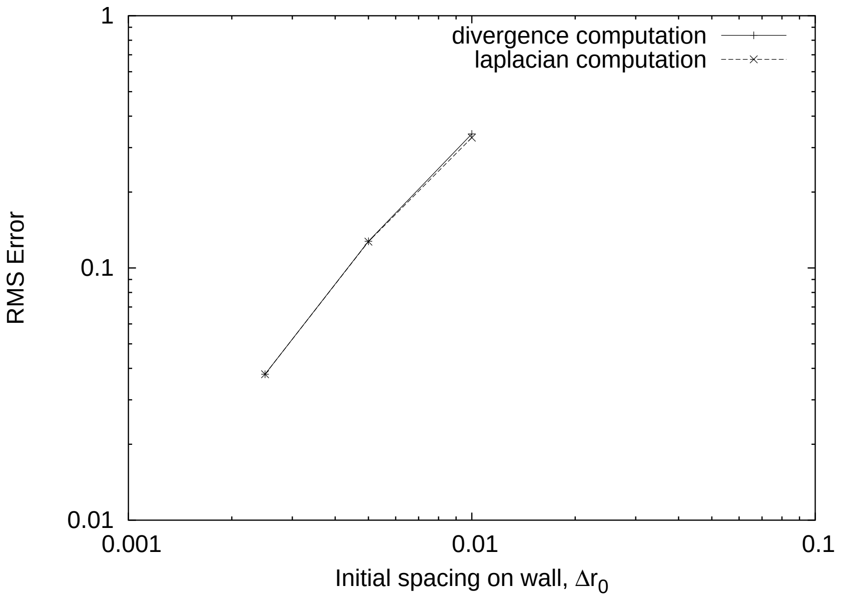

Figure 6.1: Mesh convergence test using analytic velocity fileds

6.1.1 Analytic velocity function test

The divergence operator is chosen to mimic the convective flux computation and the Laplacian operator is chosen for emulating the viscous flux evaluation. The numerical and exact solutions are compared to show the accuracy of the current spatial discretization scheme. The analytic velocity field prescribed is

$$\mathbf{U} = \sin{(x)}\,\mathbf{i} + \cos{(y)}\,\mathbf{j} + \sin(z)\mathbf{k} \tag{6.1}$$

Since the exact values of the divergence and Laplacian are known for the analytic velocity field, the error is computed by

	Δr_0	*divergence Error*	*laplacian Error*
coarse	0.01	3.401×10^{-1}	3.285×10^{-1}
medium	0.005	1.276×10^{-1}	1.271×10^{-1}
fine	0.0025	3.789×10^{-2}	3.789×10^{-2}

Table 6.2: Errors of derivitive computations by using prescribed analytic velocity field.

$$divergence\,Error_{\Delta r} = \sqrt{\frac{\sum_{i=1}^{NI} \left|(\nabla \cdot \mathbf{U})_{\Delta r} - (\nabla \cdot \mathbf{U})_{exact}\right|^2}{NI}}$$

$$laplacian\,Error_{\Delta r} = \sqrt{\frac{\sum_{i=1}^{NI} \left\|(\nabla^2 \mathbf{U})_{\Delta r} - (\nabla^2 \mathbf{U})_{exact}\right\|^2}{NI}}$$

where NI is the number of interior nodes. The order of convergence can be approximated by Richardson's extrapolation [66] as follows

$$\log_2\left(\frac{divergence\,Error_{\Delta r=0.005}}{divergence\,Error_{\Delta r=0.0025}}\right) = 1.751$$

$$\log_2\left(\frac{laplacian\,Error_{\Delta r=0.005}}{laplacian\,Error_{\Delta r=0.0025}}\right) = 1.746$$

The actual values of error for the three meshes considered are summarized in Table 6.2 and plotted in Figure 6.1. The small deviation from the second order accuracy, the theoretical order of accuracy which was derived for simple 1D meshes in equation (4.4) and (4.5), seems to be due to the higher spatial dimension.

	C_D
coarse	1.069
medium	1.081
fine	1.084

Table 6.3: Drag coefficients on the initial (coarse), once (medium) and twice (fine) refined sphere meshes, $Re = 100$

6.1.2 Flows around a sphere

Flows around a sphere for Re = 100 are tested using the three meshes mentioned before. The C_D 's for the three cases are compared in Table 6.3 and the order of convergence is estimated using the same extrapolation technique as follows

$$\log_2 \left(\frac{(C_D)_{fine} - (C_D)_{medium}}{(C_D)_{medium} - (C_D)_{coarse}} \right) = 2.0$$

As is evident, the current discretization scheme yields second order accuracy for the drag coefficient C_D.

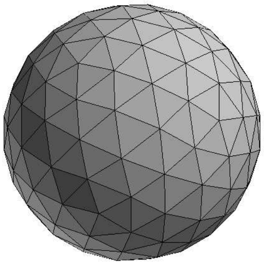

(a) coarse (162x33 nodes, 320x32 elements)

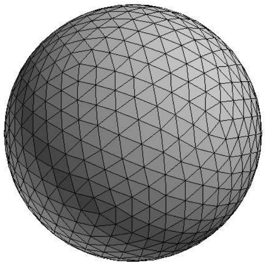

(b) medium (642x65 nodes, 1280x64 elements)

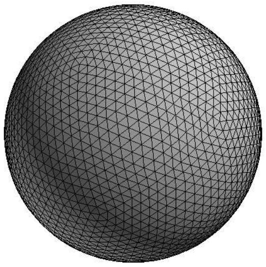

(c) fine (2562x129 nodes, 5120x128 elements)

Figure 6.2: Three levels of sphere mesh used for the mesh convergence study

6.2 High Reynolds number flows around a sphere

The current simulation of flows around a sphere is validated by comparison with experimental results. The medium sphere mesh is used for the flow simulation over a sphere. Stream lines around the sphere are shown in Figure 6.3 for $Re = 100$.

A series of simulations are performed for various orders of Reynolds numbers in the range of $10 \sim 1,000,000$. The Spalart-Allmaras turbulence model equation is solved in conjunction with the mean flow equations (the Reynolds-averaged Naiver-Stokes equations) for all cases except $Re = 10$ and $Re = 100$ which correspond to laminar flow.

The C_D values obtained by the current simulations are compared with experimental results for various values of surface roughness, and those are presented in Figure 6.4. Overall, the current simulation follows well the experiments. Drag reduction induced by boundary layer transition from laminar to turbulent is also observered for $Re \geq 100,000$. The delayed separation due to the boundary layer transition is also observed and displayed in Figure 6.5. The narrowed wake region behind the sphere is evident by the comparison between the two representative Reynolds numbers, $Re = 1,000$ and $Re = 100,000$.

One can observe a slight deviation of numerical result from the experiments for Reynolds numbers in the supercritical regime ($Re \geq 100,000$). This discrepancy at the supercritical regime may attribute to many factors, such as surface roughness of the current computation model or mis-prediction of boundary layer transition by using a relatively simple turbulent model equation. However, it should be noticed that even the experimental results are very sensitive to surface roughness in the transcritical regime.

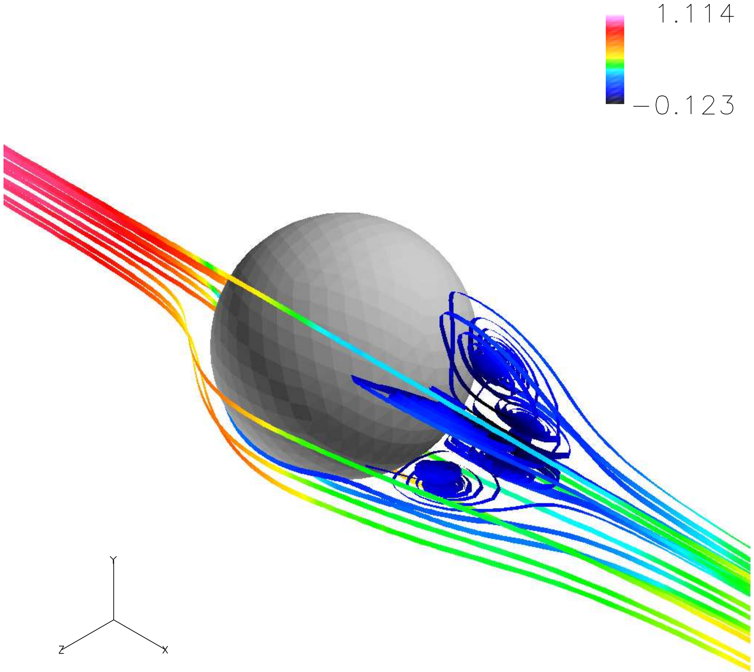

Figure 6.3: Stream lines (scaled with u-velocity) are displayed around a sphere, $Re = 100$.

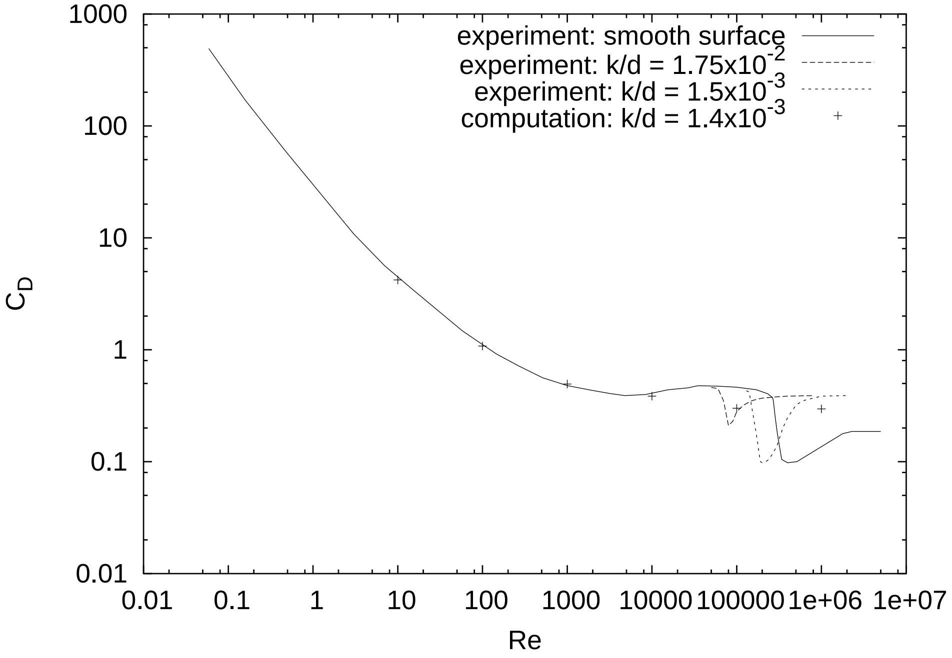

Figure 6.4: C_D vs. Re curve for flows around a sphere. Experimental results from [77, 2] and computational results obtained from the current simulation using the medium mesh are depicted.

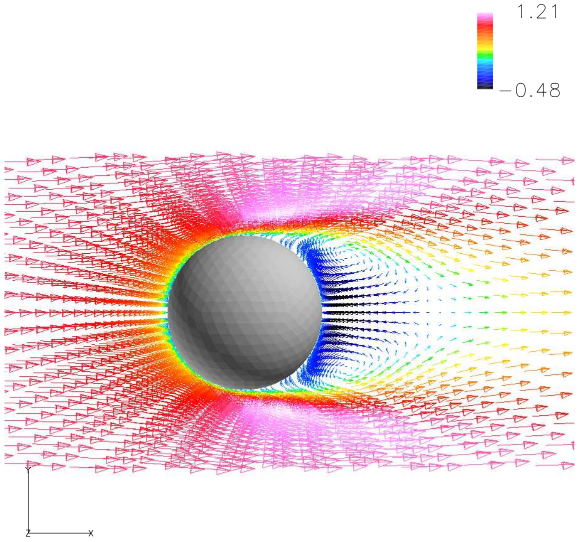

(a)$Re = 1,000$

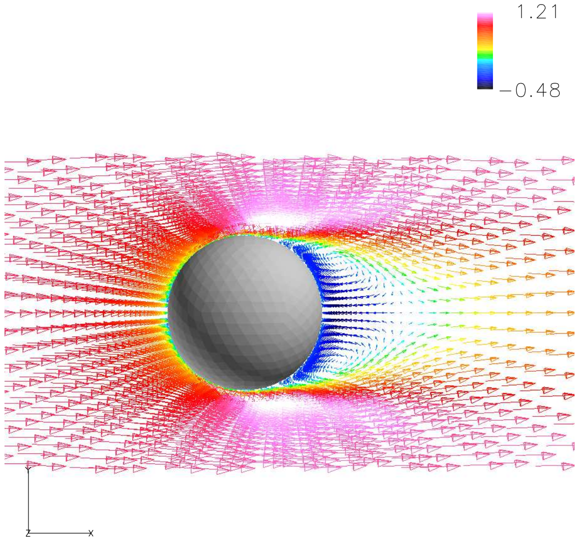

(b) $Re = 100,000$

Figure 6.5: Delayed separation and narrowed wake region due to the turbulent boundary layer development. Spalart-Allmaras model is used for all high Reynolds number flows ($Re \geq 1,000$).

6.3 Flows around a cylinder with general hybrid meshes

Flow around a circular cylinder is tested to show the validity and effectiveness of the proposed general hybrid mesh technique. Two different kinds of general hybrid meshes are used. The objectives of these general hybrid mesh simulations are first to show the accuracy of the proposed solution algorithm, and second to present the effectiveness of local hexahedra in general hybrid meshes.

The first general hybrid mesh (GHM 1) displayed in Fig. 6.6 includes local hexahedra in the frontal viscous region of the cylinder. The inclusion of local hexahedra into the GHM 1 is from *a priori* knowledge of the flow feature. Local hexahedra in the GHM 1 are intended to capture the unidirectional flow feature with a less amount of computational cost compared to the prismatic or tetrahedral elements.

The second general hybrid mesh (GHM 2) is shown in Fig. 6.7. The additional local hexahedra are introduced in the GHM 2 by replacing the wake region with a block of local hexahedra. The GHM 2 is intended to capture the wake with local hexahedra (with less number of edges) instead of tetrahedral elements in the wake region. Local hexahedra in the wake region and their lower density of edges are evident by a comparison between Figures of 6.6 and 6.7.

6.4 Effectiveness of local hexahedra

One of the major advantages of using hybrid meshes is their lower connectivity as compared to meshes with simplexes (triangles in two dimensions and tetrahedra in three dimensions). In particular, for a given set of nodes, neglecting the boundary effect, a mesh with tetrahedra contains about seven times as many edges as nodes, while a mesh with hexahedra contains only three times and a mesh with prisms contains only four times as many edges as nodes [47].

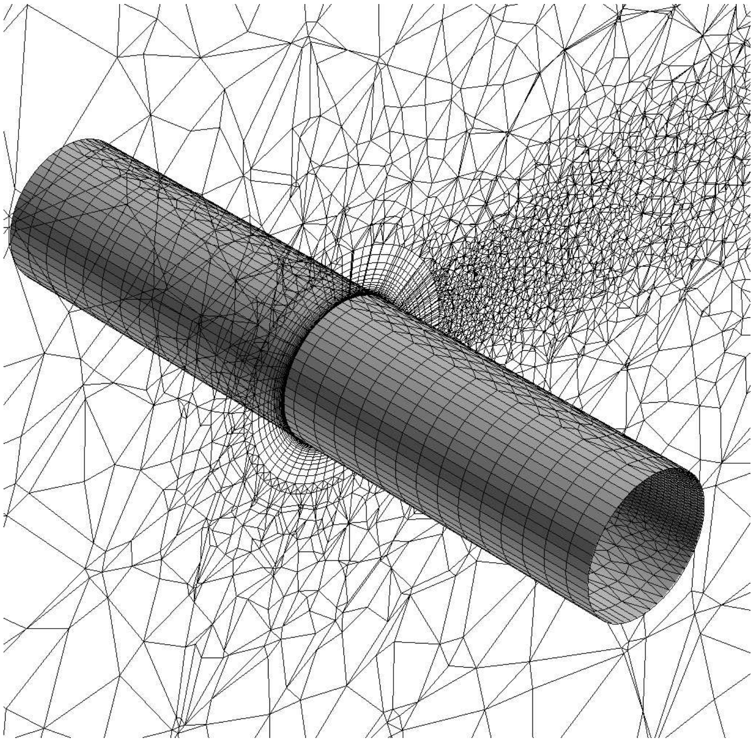

Figure 6.6: General hybrid mesh 1 (GHM 1) containing local hexahedra in the front half of the viscous region around the cylinder. $L/D = 5$.

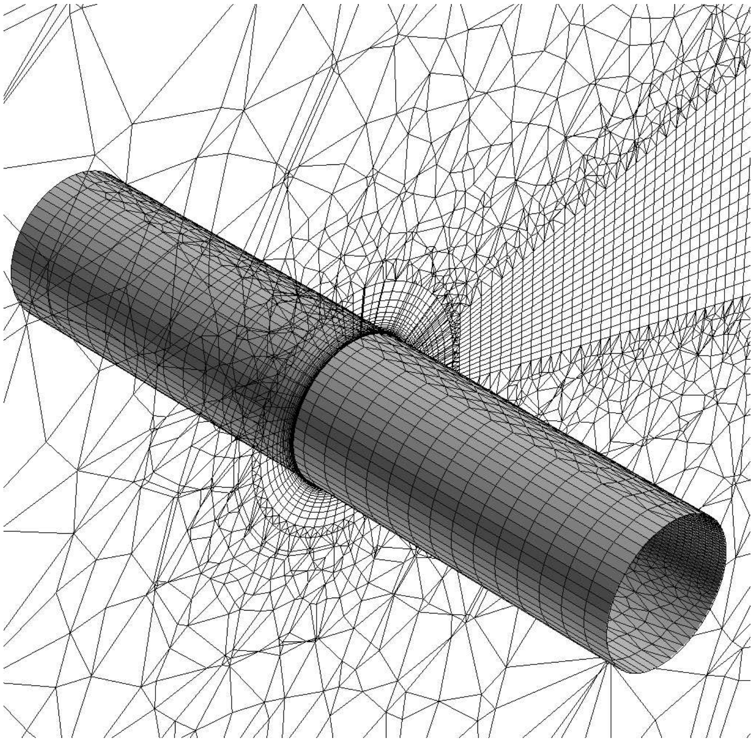

Figure 6.7: General hybrid mesh 2 (GHM 2) containing local hexahedra in the wake region as well as the frontal region of the cylinder. $L/D = 5$.

	GHM 1	GHM 2
number of nodes	148,719	158,293
number of cells	509,269	385,115
number of hexahedra	14,326	44,426
number of prisms	134,120	134,120
number of pyramids	3,770	40,026
number of tetrahedra	357,053	166,543
number of edges	749,664	683,563
number of faces	1,110,214	910,385

Table 6.4: Characteristics of proposed hybrid meshes

For the current node-centered scheme based on edge-wise flux computation, the unknowns are stored at the nodes while the computational cost is directly proportional to the number of edges, *i.e.* the amount of connectivity. If hexahedra are introduced locally in regions where the majority of nodes are located, the connectivity can be reduced considerably and the overall computational time can be saved accordingly.

The characteristics of the two general hybrid meshes are presented in Table 6.4. As is clear, by introducing more hexahedra into GHM 2, the reduction of tethedra is substantial. Furthermore, the numbers of edges and faces decrease in GHM 2, even though it contains more nodes than GHM 1. The number of edges is the parameter indicating the overall cost of flux computation based on edge-wise operations, and the number of faces is the performance indicator for the velocity gradient computation routine which involves the face-wise surface integrals of edge-duals. It can be expected that the computational cost of GHM 2, which contains a smaller number of edges and faces than GHM 1, will be less expensive than GHM-1 even though GHM 2 has more nodes.

		GHM-1	GHM-2
Central difference	CPU time	4889	4709
	CPU time / NI	0.0328	0.0297
	Max Memory	1265	1214
	Max Memory / NI	0.00850	0.00766
Upwind	CPU time	6250	6063
	CPU time / NI	0.0420	0.0383
	Max Memory	1268	1216
	Max Memory / NI	0.00852	0.00768

Table 6.5: Performance metrics for the hybrid meshes with and without local hexahedra in the wake region. Maximum memory is measured in MB, and the CPU time is measured in second when the simulation reaches $Time = 1.0$ on 16 processors. Metrics are then normalized by the division of total number of nodes (NI).

The C_D and C_L histories for the flows around a circular cylinder by using the two proposed general hybrid meshes are presented in Fig. 6.8. The results of the two general hybrid meshes are almost identical , and this indicates that the local hexahedra are successfully introduced in the wake region and give as accurate result as conventional meshes with tetrahedra in the region.

The performance metrics for the two hybrid meshes are compared in Table 6.5. The performance is measured in terms of total computational time and also maximum memory requirement. The central scheme is used with modified smoothing based on the solution reconstruction, and the second order upwind scheme is employed by using Roe's flux-difference splitting scheme. For all categories of performance metrics, the GHM 2 shows about 10% savings over the GHM 1, which is the direct effect of local hexahedra in the wake region. The saving in computational cost comes not only from CPU time but also from the amount of memory required. This is because local hexahedra save edges as well as faces which are the indicators of total memory requirement.

Since both of the tested meshes are already taking advantage of local hexahedra, this saving from local hexahedra in general hybrid meshes can be expected to be much more evident when they are compared to tetrahedral meshes or conventional hybrid meshes containing prisms and tetrahedra.

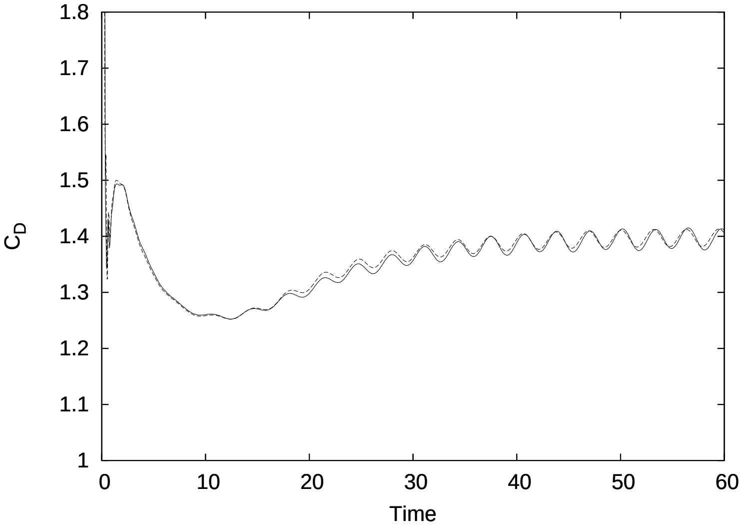

(a) Span-averaged C_D histories

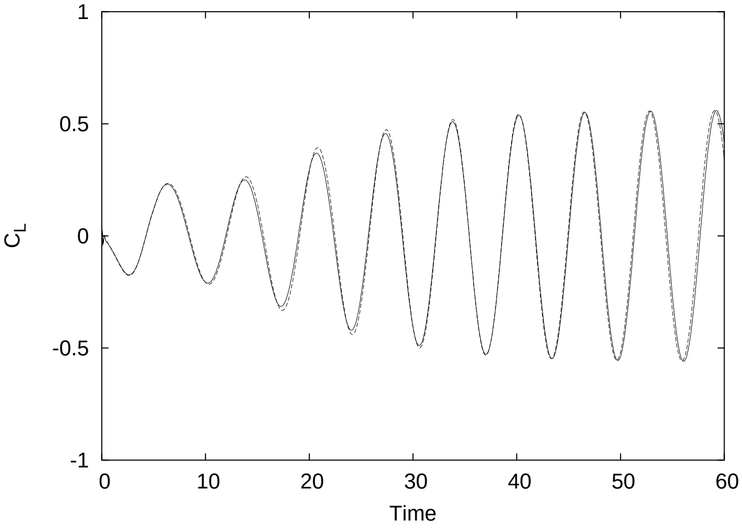

(b) Span-averaged C_L histories

Figure 6.8: Local hexahedra effect on C_D and C_L histories. The central difference scheme is used with modified smoothing of $\sigma_4 = 0.1$. Solid lines stand for the GHM 1 containing hexahedra only in the frontal viscous region, and the dashed lines stand for the GHM 2 which contains hexahedra in the wake region as well as the frontal viscous region. $Re = 150$.

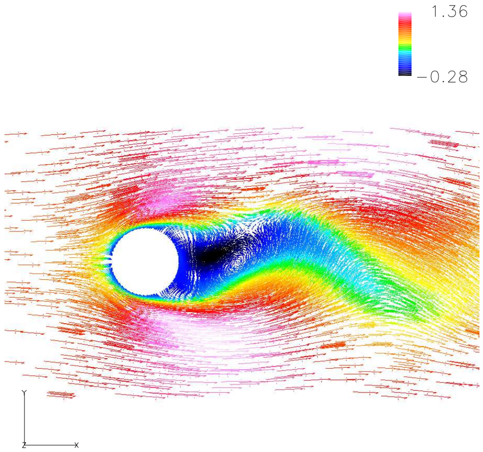

(a) general hybrid mesh 1

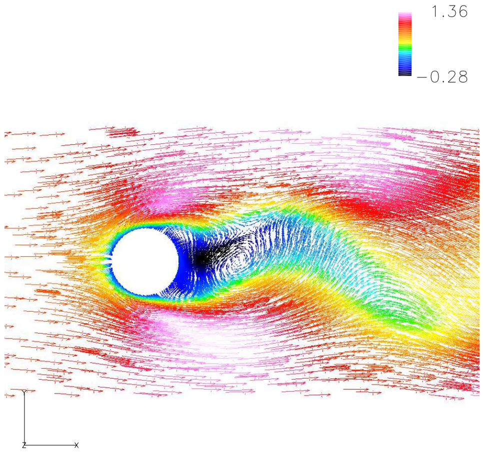

(b) general hybrid mesh 2

Figure 6.9: Comparison of velocity fileds for $Re = 150$ on general hybrid mesh 1 (GHM 1) and general hybrid mesh 2 (GHM 2). GHM 1 contains local hexahedra only in the frontal viscous region and GHM 2 contains local hexahedra in the wake region as well as the frontal viscous region. Velocity snap shots are taken at the time step within a shedding cycle.

6.5 High Reynolds number flows around a cylinder

The validity of the current Navier-Stokes method for general hybrid meshes is further emphasized by a series of high Reynolds number flow simulations over a circular cylinder. A wide range of Reynolds numbers are tested; $Re = 10 \sim 1,000,000$. For the cases of $Re \leq 100$ the flow is considered as laminar, hence no turbulence model is used. For the rest of the cases, $Re \geq 1,000$, the Spalart-Allmaras turbulence model is solved in conjunction with the mean flow equation. GHM 1, shown in Figure 6.6, is used for all of the cases.

For the series of Reynolds number, C_D is compared with experimental results. As shown in Figure 6.10, the current simulation agrees well with the experimental results. Expecially for the $Re = 100,000$ case, a sharp drop of C_D is predicted which is indicating the delayed separation induced by the boundary layer transition from laminar to turbulent. This delayed separation and narrowed wake region at $Re = 100,000$ is compared to the $Re = 1000$ case and those are displayed in Figure 6.11.

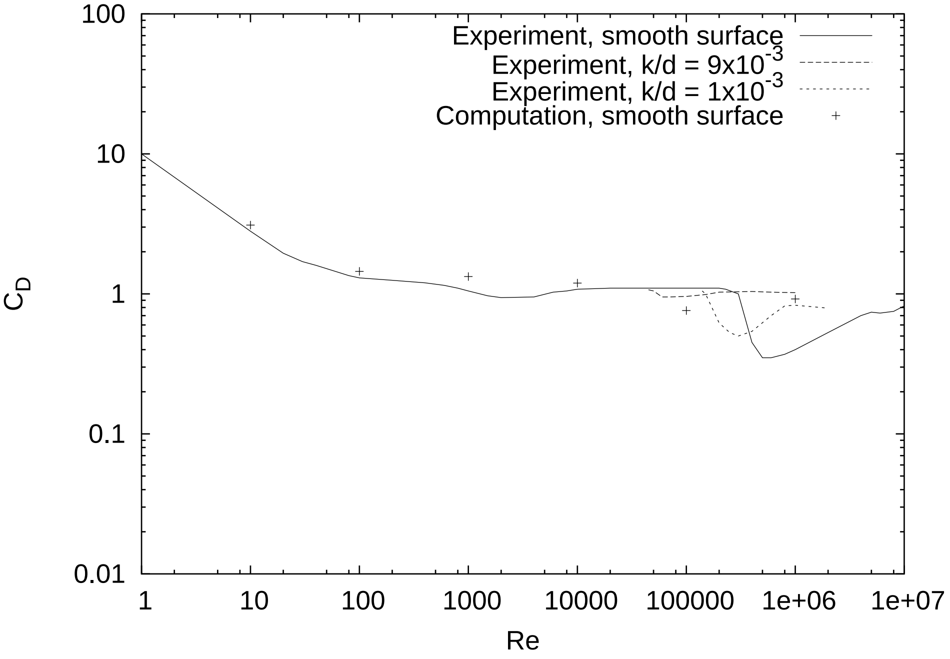

Figure 6.10: *Cd* vs. *Re* curve for cylinder using the general hybrid mesh 1. Computational result is obtained by the current simulation on general hybrid mesh, and experimental result are from [77, 54, 1, 74].

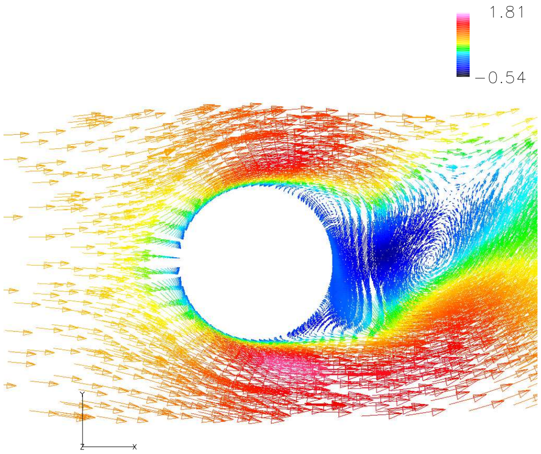

(a) $Re = 1,000$

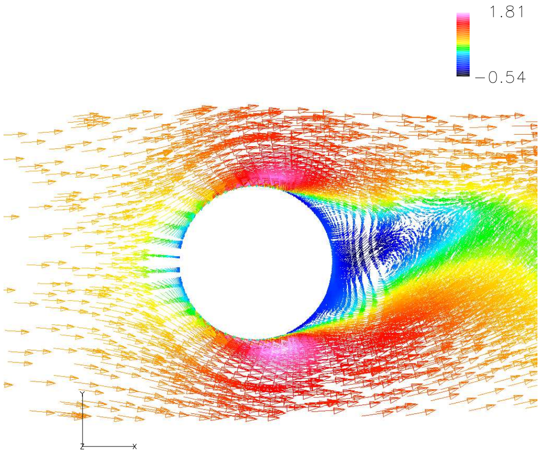

(b) $Re = 100,000$

Figure 6.11: Prediction of delayed separation (accompanied by a smaller wake region) due to the boundary layer transition from laminar to turbulent. Velocity fields, colored with u-velocity magnitude, are taken at the same time step within a shedding cycle. The Spalart-Allmaras turbulence model is used for both cases on the general hybrid mesh 1.

Chapter 7

Strong Coupling of Flow and Structure Interactions

In this chapter, the equation of motion for a cylinder subjected to vortex-induced vibration (VIV) is presented. The cylinder is modeled as a set of beam elements freely vibrating in the cross-flow direction. The equation of motion is nondimensionalized by using the same reference quantities used for the flow equations. Two coupling strategies for the fluid and structure interactions are introduced; namely weak coupling and strong coupling. The weak coupling is implemented by an explicit central difference scheme, and the strong coupling is constructed by using a predictor-corrector method driven by the pair of central difference and trapezoidal schemes. A comparison of the two coupling methods is presented and the superior stability property of strong coupling is emphasized.

7.1 Structural model for the cylinder

Different structural elements can be used for modelling the vibrating cylinder. For example, strings (cables), beams, or plates can be used. Typically, cables represent extremely slender structures with tensional rigidity but no bending stiffness. Such models can be a good choice for tension dominated behavior of structure, which is characterized by the following criterion [96]

$$\frac{T}{EIk^2} > 30 \tag{7.1}$$

where T is the tension, EI is the bending stiffness, and k is the wave number describing the excitation mode. As shown in equation 7.1, if the bending stiffness becomes significant (*i.e.* the aspect ratio L/D of the cylinder becomes smaller), then the cable model cannot be used and bending stiffness should be included.

For cylinder models representing offshore risers (hollow cylinders containing oil), plate elements can also be considered. However, the deformation of the riser pipe in the cross sectional plane is negligible compared to the rigid body motion.

As suggested by the elementary beam theory, if the aspect ratio is $L/D \sim 10$, the beam element can be a suitable choice to model the structure [30]. Hence, the cylinder for the current study, with moderate aspect ratio $L/D \leq O(10)$ and no cross sectional deformation, is modeled with beam elements.

7.2 Equation of motion for the bending vibration

The cylinder in Figure 7.1 is modeled with a structural beam element of four degrees of freedom (v_1, θ_1, v_2, θ_2). The direction of the cross flow displacement (v) coincides with the y-axis and the direction of the rotational degree of freedom (θ) lies in the negative x-direction in order to be consistent with the sign convention of the beam element.

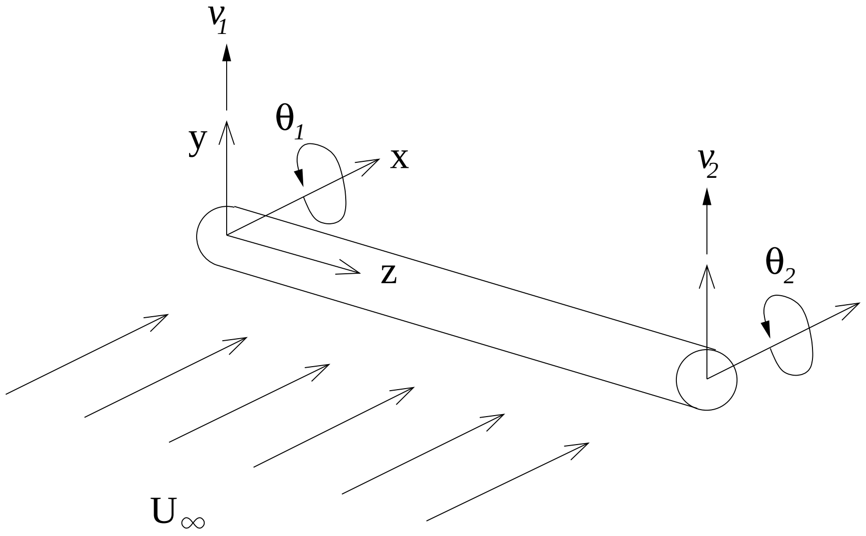

Figure 7.1: Structural model in 3D

The displacement function is expressed as

$$v(z) = f_1(z)\, v_1 + f_2(z)\, \theta_1 + f_2(z)\, v_2 + f_4(z)\, \theta_2 \tag{7.2}$$

where the four Hermite cubic shape functions are given by

$$
\begin{aligned}
f_1(z) &= 1 - 3\left(\tfrac{z}{L}\right)^2 + 2\left(\tfrac{z}{L}\right)^3 \\
f_2(z) &= z - 2\left(\tfrac{z^2}{L}\right) + \left(\tfrac{z^3}{L^2}\right) \\
f_3(z) &= 3\left(\tfrac{z}{L}\right)^2 - 2\left(\tfrac{z}{L}\right)^3 \\
f_4(z) &= -\left(\tfrac{z^2}{L}\right) + \left(\tfrac{z^3}{L^2}\right)
\end{aligned}
\tag{7.3}
$$

Since these cubic functions ensure that both the displacement and slope (first derivative) is continuous across the boundary of elements, they form a C^1 basis.

The kinetic energy of the beam element in flexural vibration is given by

$$T = \frac{\rho_s A}{2} \int_0^L \dot{v}(z)^2 \, dz \tag{7.4}$$

where ρ_s is structure density and A is the cross-sectional area of the cylinder. The strain energy for the beam element in bending is expressed by

$$U = \frac{EI}{2} \int_0^L v''(z)^2 dz \tag{7.5}$$

Primes denote the derivatives with respect to the axial direction z, while dots indicate differentiation with respect to time t.

The flexural (bending) stiffness of a beam is defined as EI, where E is Young's elastic modulus of the beam and I is the cross-sectional area moment of inertia about the neutral axis. For a cylinder with a circular cross-section the area moment of inertia is defined by

$$I = \frac{\pi}{64} D^4$$

where D is the cylinder diameter.

Substituting the displacement function into the kinetic energy and strain energy expressions, and using Lagrange's equation [98] yields the equation of motion for the beam element. Lagrange's equation is given by

$$\frac{d}{dt}\left(\frac{\partial T}{\partial \dot{q}_i}\right) + \frac{\partial U}{\partial q_i} = F_i \tag{7.6}$$

where q_i is i -th degree of freedom, and F_i refers to the external force associated with the i -th degree of freedom. Applying Lagrange's equation with respect to each one of the four degrees of freedom yields the set of equations of motion

$$\mathbf{M}\ddot{\mathbf{q}}\,(t) + \mathbf{K}\mathbf{q}\,(t) = \mathbf{f}\,(t) \tag{7.7}$$

where the components of the mass and stiffness matrices $\mathbf{M}, \mathbf{K}$ are respectively given by

$$m_{ij} = \rho_s A \int_0^L f_i\,(z) f_j\,(z)\,dz$$

and

$$k_{ij} = EI \int_0^L f_i''\,(z) f_j''\,(z)\,dz.$$

Finally, expanding equation (7.7) yields the complete set of equations of motion for a beam element

$$\begin{aligned} &\tfrac{\rho_s AL}{420}\begin{bmatrix} 156 & 22L & 54 & -13L \\ 22L & 4L^2 & 13L & -3L^2 \\ 54 & 13L & 156 & -22L \\ -13L & -3L^2 & -22L & 4L^2 \end{bmatrix}\begin{Bmatrix} \ddot{v}_1 \\ \ddot{\theta}_1 \\ \ddot{v}_2 \\ \ddot{\theta}_1 \end{Bmatrix} \\ &+\tfrac{EI}{L^3}\begin{bmatrix} 12 & 6L & -12 & 6L \\ 6L & 4L^2 & -6L & 2L^2 \\ -12 & -6L & 12 & -6L \\ 6L & 2L^2 & -6L & 4L^2 \end{bmatrix}\begin{Bmatrix} v_1 \\ \theta_1 \\ v_2 \\ \theta_1 \end{Bmatrix} = \begin{Bmatrix} Y_1 \\ M_1 \\ Y_2 \\ M_2 \end{Bmatrix} \end{aligned} \tag{7.8}$$

7.3 Nondimensionalization of the equation of motion

Any equation dimensionally homogeneous can be nondimensionalized by normalizing every term with respect to the reference quantities. Using the following relations of nondimensional length and time scales

$$v^* = \frac{v}{D}, \quad L^* = \frac{L}{D}, \quad t^* = \frac{t}{D/U_\infty}$$

the system of the equations of motion (7.7) becomes

$$\mathbf{M}^* \ddot{\mathbf{q}}^* (t^*) + \frac{1}{L^4} \frac{EI}{\rho_s A} \left(\frac{D}{U_\infty} \right)^2 \mathbf{K}^* \mathbf{q}^* (t^*) = \frac{\rho D^2}{\rho_s A} \frac{D}{L} \mathbf{f}^* (t^*) \tag{7.9}$$

where the nondimensionalized mass and stiffness matrices are the same with the dimensional ones expressed in Eq. (7.8), but with the dimensional length L replaced by the nondimensional length scale L^*, that is

$$\mathbf{M}^* = \frac{1}{420} \begin{bmatrix} 156 & 22L^* & 54 & -13L^* \\ 22L^* & 4L^{*2} & 13L^* & -3L^{*2} \\ 54 & 13L^* & 156 & -22L^* \\ -13L^* & -3L^{*2} & -22L^* & 4L^{*2} \end{bmatrix}$$

,

$$\mathbf{K}^* = \begin{bmatrix} 12 & 6L^* & -12 & 6L^* \\ 6L^* & 4L^{*2} & -6L^* & 2L^{*2} \\ -12 & -6L^* & 12 & -6L^* \\ 6L^* & 2L^{*2} & -6L^* & 4L^{*2} \end{bmatrix}$$

The fluid forces acting on the cylinder need to be transferred to a set of equivalent nodal forces and moments at the structural nodes. This hydrodynamic force can be regarded as an arbitrarily distributed load, and is composed of a pressure force and a friction force due to viscous effects. For example, at $Re = 150$, the friction force is about 10% of the total hydrodynamic load, and the pressure force

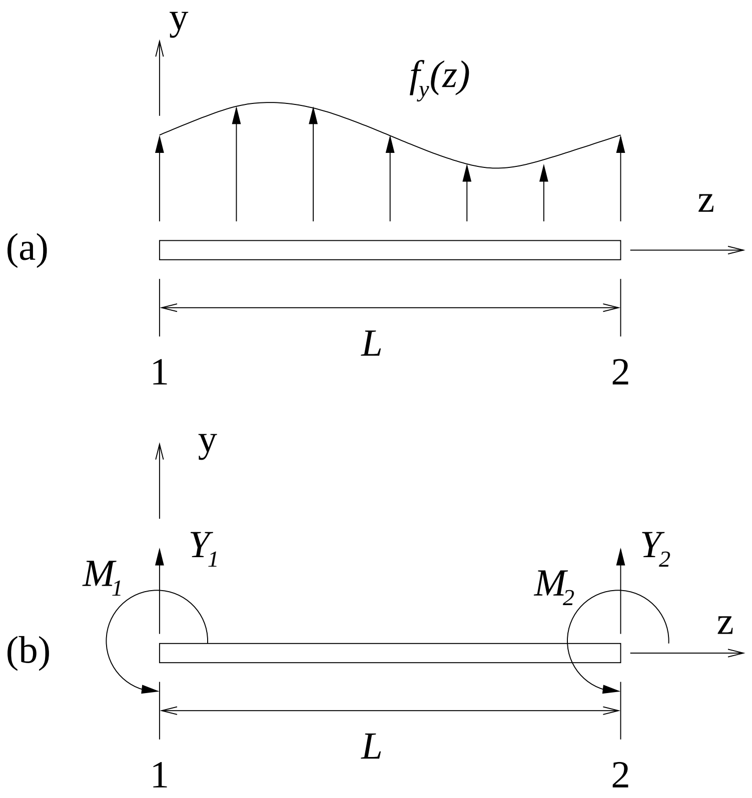

Figure 7.2: Beam element subjected to (a) an arbitrarily distributed load and (b) equivalent nodal forces and moments of the uniformly distributed load

accounts for the rest. As Reynolds number increases, typically the pressure force becomes the dominant source of hydrodynamic load.

Once the pressure and velocity fields around the cylinder are obtained, the work equivalence method is used to compute the discrete nodal load from the arbitrarily distributed load induced by the fluid. The method is based on the concept that the work done by the distributed load is equal to the work done by the nodal load replacement for arbitrary nodal displacements. The two equivalent load systems are delineated in Fig. 7.2.

The work-equivalent nodal load due to the distributed hydrodynamic force can be computed as

$$\mathbf{f}^*\left(t^*\right)=\left\{\begin{array}{c} Y_1^*\left(t^*\right) \\ M_1^*\left(t^*\right) \\ Y_2^*\left(t^*\right) \\ M_2^*\left(t^*\right) \end{array}\right\}=\left\{\begin{array}{c} \int_o^{L^*} f_y\left(z,t^*\right) f_1\left(z\right) dz \\ \int_o^{L^*} f_y\left(z,t^*\right) f_2\left(z\right) dz \\ \int_o^{L^*} f_y\left(z,t^*\right) f_3\left(z\right) dz \\ \int_o^{L^*} f_y\left(z,t^*\right) f_4\left(z\right) dz \end{array}\right\}$$

where $f_y(z,t^*)$ is the distributed hydrodynamic force due to the pressure and viscous friction in the cross-flow direction, and f_1, f_2, f_3, and f_4 are the cubic Hermite polynomial functions defined in Eq. (7.3).

The solution vector of the nondimensionalized degrees of freedom is given by

$$\mathbf{q}^*\left(t^*\right)=\left\{\begin{array}{c} v_1^*\left(t^*\right) \\ \theta_1^*\left(t^*\right) \\ v_2^*\left(t^*\right) \\ \theta_1^*\left(t^*\right) \end{array}\right\}$$

The system of equations of motion in non-dimensional form can be further simplified as

$$\mathbf{M}^*\ddot{\mathbf{q}}^*\left(t^*\right)+\left(\frac{4\pi^2}{U_{red}^2}\right)\left(\frac{1}{L^{*4}}\right)\mathbf{K}^*\mathbf{q}^*\left(t^*\right)=\left(\frac{1}{M_{red}}\right)\left(\frac{1}{L^*}\right)\mathbf{f}^*\left(t^*\right) \tag{7.10}$$

by introducing the two non-dimensional parameters U_{red} and M_{red} as defined below. First, the reduced velocity, U_{red}, is defined as

$$U_{red} = \frac{U_\infty}{f_n D} \tag{7.11}$$

with the effective natural frequency of the structure, ω_n, given by

$$\omega_n = \frac{1}{D^2}\sqrt{\frac{EI}{\rho_s A}} = 2\pi f_n$$

As shown in the definition of the effective natural frequency, it does not include the length scale L but represents the natural frequency of a unit length cylinder. Hence, for a given U_{red}, if the length of the cylinder changes, the natural frequency of the cylinder also changes. In order to make a cylinder with a different length remain in the same resonant state, U_{red} also has to be changed accordingly. This is because the reduced velocity affects the bending stiffness of the structure, and the stiffness of the structure also affects the natural frequency of the bending vibration.

The main interest of this simulation is in the vortex induced vibration of the cylinder at its resonant state, namely the lock-in state. Hence U_{red} of our structural model is carefully chosen so that its natural frequency of bending vibration of interest, typically in its first or second mode, is approximately equal to the natural frequency of vortex shedding over a fixed cylinder. One simple way of checking the natural frequency of the multiple element beam model is by solving a free vibration (no forcing term in RHS) problem.

The reduced mass, M_{red},which is the ratio of the mass of the structure to the mass of the fluid displaced by the structure, is defined as,

$$M_{red} = \frac{\rho_s A}{\rho D^2}. \tag{7.12}$$

This reduced mass represents the inertia of the structural system with respect to the surrounding fluid. Hence, a smaller mass ratio implies a bigger influence from the flow with the same scale of hydrodynamic forces. The mass ratio for the VIV in air is in the order of $O(1000)$. For marine cables in water varies between $1 \sim 10$, hence we used the representative mass ratio of $M_{red} = 2$ [55, 17] for the current simulations.

7.4 Coupling strategies

If the flow and structural solvers are being solved separately, then their interaction can be implemented using either a strong coupling method or a weak coupling method depending on how the information between the two solvers is communicated.

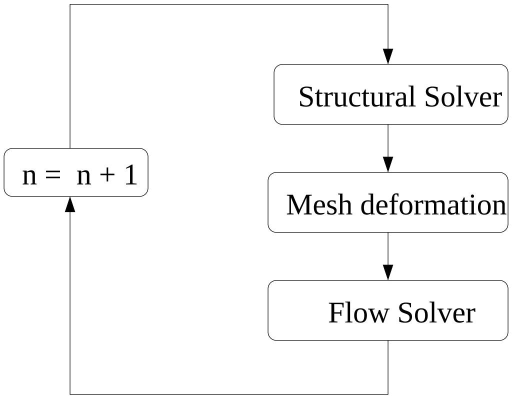

Figure 7.3: Weak coupling

In the weak coupling strategy, the solution of the flow field at the next time step is computed from the structural configuration of the previous time step. Once the solution of the flow field is converged, the new forces acting on the structure are sent to the structural solver for the new configuration of structure at the next time step. This simple loop makes both solvers advance one time step. In the weak coupling method, the external forces to the structural solver come from the solution of previous mesh configuration, hence this method is also refered as a *staggered* or *loosely* coupled scheme. When the time step is relatively small (especially when an explicit scheme is used for the flow solver), this weak coupling method can be a reasonable choice [23].

When an implicit scheme is used for the flow solver, time steps used for the flow solver is comparable to the time steps restricted by the structural solver. To make the coupling stable even with large time steps of implicit flow solvers, the structural solver also needs to be solved in an implicit manner which is called strong coupling. In order to couple the two solvers strongly, iterations between the flow and structural solvers are necessary for each time step, and this makes their coupling stable even with large time steps.

The results of two coupling methods are presented in Fig. 7.4 for flow-structure interactions with time step $\Delta t = 0.4$. For the strong coupling, the flow and structure interaction is stable, but the weak coupling starts with oscillations and eventually diverges. This comparison demonstrates the superior stability property of the strong coupling.

For the implementation of the strong coupling, a predictor-corrector (PC) method is employed. Any explicit scheme can be used for the predictor, and an implicit scheme can be used for the corrector.

The correction iteration may be performed until some criterion of convergence, such as $\left\|\mathbf{y}^{\mu+1} - \mathbf{y}^{\mu}\right\| < \varepsilon$ is achieved, where $\mathbf{y}$ is the vector of unknowns for the structural solver, and ε is the tolerance of the convergence. This strategy is called *iterating to convergence*. In this mode, the accuracy and stability properties are irrespective of the predictor and highly dependent on the corrector alone. What makes this mode unattractive in practice is that we cannot tell in advance how many iterations of the corrector (i.e. how many evaluations of the flow field) will be involved at each time step. In general this is to be avoided, and especially for the real-time systems [40].

A more acceptable procedure is to fix the number of corrector interations in advance. The number of corrector iterations (μ) is small and normally chosen to 1 or 2, with the assumption that the predictor formula is of sufficiently high order q for $p - 1 \leq q \leq p$, where p is the order of the corrector formula. For current study, central different scheme is used for the predictor step and trapezodial scheme is used for the corrector iterations. Both of the schemes are second order accurate, and only one corrector step improves the stability considerably, as shown in Fig. 7.4.

The predictor step is followed by a new evaluation of the flow field and each corrector step is also followed by a new evaluation of the flow field. This precedure can be represented as

$$PE \quad \underbrace{CE \cdots CE}_{corrector\, iteration}$$

where P represents the predictor step, C represents the corrector step, and E represents the evaluation of flow field. When the corrector iteration is fixed to μ, the predictor-corrector method can be expressed more conveniently as $PE\,(CE)^{\mu}$. The evaluation of the flow field following the last corrector step may be omitted, but finishing the PC method with the last evaluation gives better stability. Hence, we always solve the flow field whenever a new structural configuration is obtained. For the PC method with μ corrector iterations, the total number of evaluations of the flow field is $\mu + 1$. The strong coupling using the PC method is restored to the weak coupling when the corrector iteration loop is omitted.

7.5 Strong coupling by using the PC method

For the current study, the central difference scheme in time is used for the predictor, and the trapezoidal scheme is used for the corrector. Both schemes are second order accurate in time, hence this pair (central-trapezoidal) of the PC method is expected to be second order accurate. Since the time integration scheme of the flow solver is also second order (second order backward difference formula), the current choice of PC pair should not deteriorate the temporal accuracy when it is coupled with the flow solver.

When the structure is modeled with multiple elements, the complete system of equations can be assembled by using the equations of motion for a single master element as shown in Eq. (7.10). Once global mass and stiffness matrices are assembled and proper boundary conditions are applied, the governing equations of the bending vibration can be rewritten in a set of coupled second order ordinary differential equations with a given set of initial conditions as below.

$$\mathbf{M}\ddot{\mathbf{y}}\left(t\right) + \mathbf{K}\mathbf{y}\left(t\right) = \mathbf{f}\left(t\right), \quad t > 0, \quad \mathbf{y}\left(0\right) = \mathbf{y}_0 \quad \dot{\mathbf{y}}\left(0\right) = \dot{\mathbf{y}}_0 \tag{7.13}$$

where $\mathbf{M}$ and $\mathbf{K}$ are the global mass and stiffness matrices, $\mathbf{y}$ and $\ddot{\mathbf{y}}$ are the vectors containing unknown degrees of freedom and their accleration, $\mathbf{y}$ and $\dot{\mathbf{y}}$ are the initial conditions, and $\mathbf{f}$ is external load vector from the flow around the cylinder. The equation of motion in Eq. (7.13) is in nondimensional form, and all the $*$'s representing the nondimensional quantities are ommitted for simplicity.

Any explicit/implicit pair can be used for the predictor/corrector method. For the predictor of the current simulation, the central difference scheme with lagged approximation of the first derivative is used because of its popularity in structural dynamics. For the corrector step, the unconditionally stable trapezoidal scheme is used. This trapezoidal method can be considered a special case of the Newmark method with average acceleration.

The central difference scheme used for the predictor can be derived by using the central differenced acceleration

$$\ddot{\mathbf{y}}_n = \frac{1}{\Delta t^2}\left(\mathbf{y}_{n+1} - 2\mathbf{y}_n + \mathbf{y}_{n-1}\right) \tag{7.14}$$

and velocity which is lagging half a time step as below.

$$\dot{\mathbf{y}}_n \approx \dot{\mathbf{y}}_{n-\frac{1}{2}} = \frac{1}{\Delta t}\left(\mathbf{y}_n - \mathbf{y}_{n-1}\right) \tag{7.15}$$

Even with the lagged approximation of the velocity, the central difference scheme is reported to be second order accurate for the system of small damping [14].

Hence, the central difference scheme for the current structural model with no damping can be expected to be second order accurate.

By using the central differenced accleration and velocity as expressed in Eq. (7.14) and Eq. (7.15) respectively, and the equation of motion in Eq. (7.10), the predictor scheme can be expressed as below.

Predictor

$$\begin{aligned}
\mathbf{y}_{n+1}^{(\mu=0)} &= \Delta t^2 \mathbf{M}^{-1}\left(\mathbf{f}_n - \mathbf{K}\mathbf{y}_n\right) + \mathbf{y}_n + \Delta t \dot{\mathbf{y}}_{n-\frac{1}{2}} \\
\dot{\mathbf{y}}_{n+1}^{(\mu=0)} &\approx \dot{\mathbf{y}}_{n+\frac{1}{2}}^{(\mu=0)} = \tfrac{1}{\Delta t}\left(\dot{\mathbf{y}}_{n+1}^{(\mu=0)} - \mathbf{y}_n\right)
\end{aligned}$$

By using the trapezoidal rule, the displacement and velocity can be expressed as.

$$\mathbf{y}_{n+1} = \mathbf{y}_n + \frac{\Delta t}{2}\left(\dot{\mathbf{y}}_n + \dot{\mathbf{y}}_{n+1}\right)$$

$$\dot{\mathbf{y}}_{n+1} = \dot{\mathbf{y}}_n + \frac{\Delta t}{2}\left(\ddot{\mathbf{y}}_n + \ddot{\mathbf{y}}_{n+1}\right)$$

The velocity and acceleration for the next time step can be derived from the above relation.

$$\dot{\mathbf{y}}_{n+1} = \frac{2}{\Delta t}\left(\mathbf{y}_{n+1} - \mathbf{y}_n\right) - \dot{\mathbf{y}}_n$$

$$\ddot{\mathbf{y}}_{n+1} = \frac{4}{\Delta t^2}\left(\mathbf{y}_{n+1} - \mathbf{y}_n\right) - \frac{4}{\Delta t}\dot{\mathbf{y}}_n - \ddot{\mathbf{y}}_n$$

Using the equation of motion Eq. (7.10) and the above relations, the corrector scheme can be expressed as.

Corrector

for $i = 1, \cdots, \mu_{max}$

```
    $\mathbf{y}_{n+1}^{(\mu)} = \left(\frac{4}{\Delta t^2}\mathbf{M} + \mathbf{K}\right)^{-1} \left(\mathbf{f}_{n+1}^{(\mu-1)} + \mathbf{M}\left(\frac{4}{\Delta t^2}\mathbf{y}_n + \frac{4}{\Delta t}\dot{\mathbf{y}}_n + \ddot{\mathbf{y}}_n\right)\right)$
    $\dot{\mathbf{y}}_{n+1}^{(\mu)} = \frac{2}{\Delta t}\left(\mathbf{y}_{n+1}^{(\mu)} - \mathbf{y}_n\right) - \dot{\mathbf{y}}_n$
end
```

The corrector iteration is performed until it meets the maximum number of iterations (μ_{max}). For the current study, only one corrector iteration ($\mu_{max} = 1$) is performed, and this makes the coupling stable for all time steps used in this study.

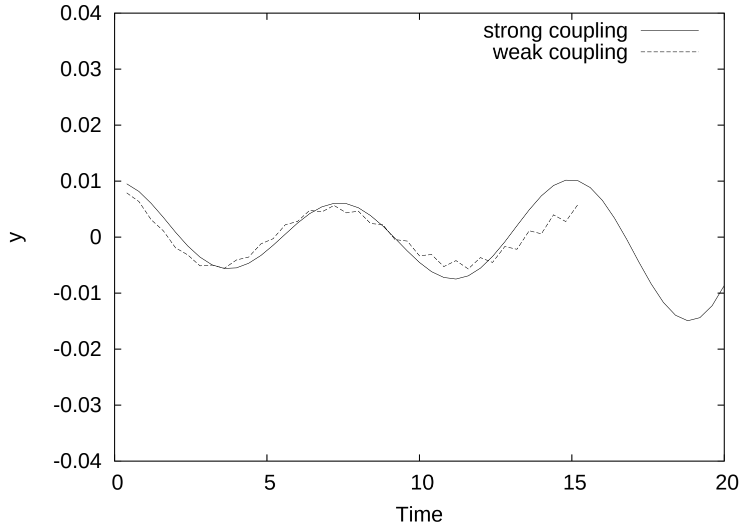

(a) vertical displacement at the center of the cylinder

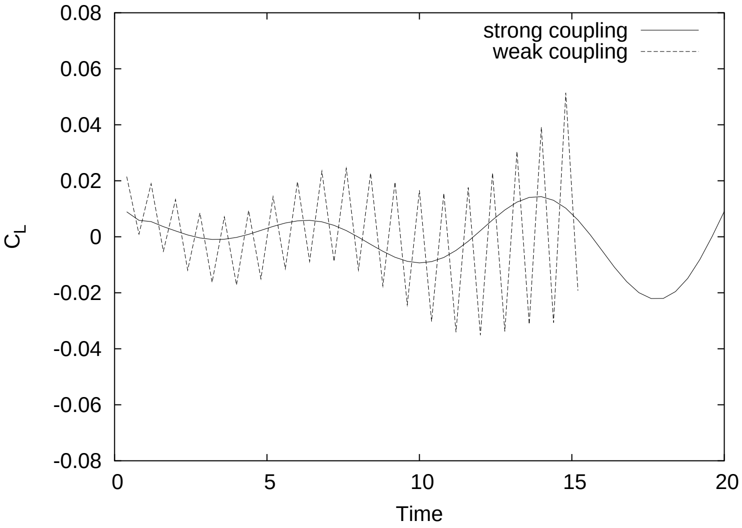

(b) span-averaged C_L of the clyinder

Figure 7.4: Comparison of strong and weak couplings with $\Delta t = 0.4$. Clamped boundary conditions at both ends of the cylinder ($L/D = 5.0$, $U_{red} = 5.0$). Explicit central difference scheme is used for the weak coupling, and predictor-corrector method, driven by central difference and trapezodial schemes, is used for the strong coupling. Only one corrector iteration is performed for the corrector iteration of strong coupling.

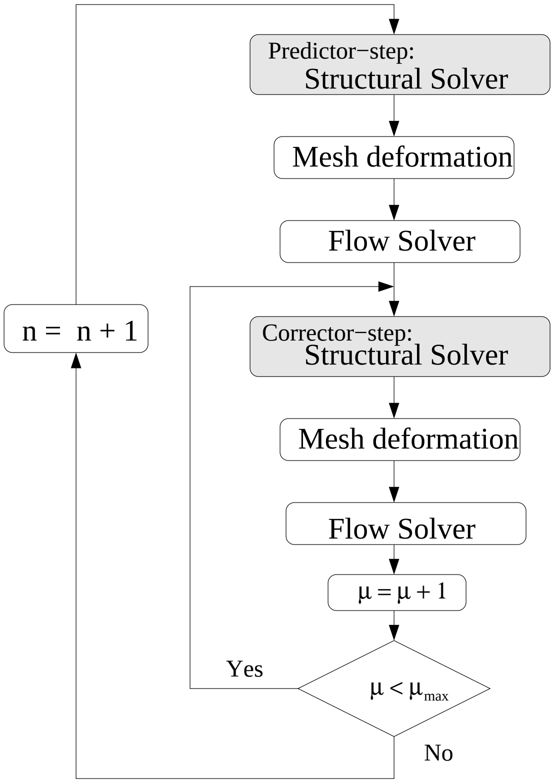

Figure 7.5: Strong coupling using Predictor-Corrector scheme in a fixed number of iteration mode

Chapter 8

Verification of the Solution Algorithm for Fluid and Structure Interactions

In this chapter, a verification study of the ALE scheme is presented, and then it is applied to fluid and structure interaction problems. In the first part of the chapter, the proposed ALE scheme with moving mesh source term is verified with forced excitation of the cylinder. The significance of the moving mesh source term is demonstrated in terms of the uniform flow preserving capability. Temporal accuracy of the current time integration scheme is demonstrated by a time step refinement study. In the second part, the ALE scheme is applied to the vortex-induced vibration (VIV) of the cylinder. A VIV initiation technique is introduced, and a time step refinement study is presented. Different end conditions are applied to the vibrating cylinder, and finally the current numerical result is compared with others in literature.

8.1 Verification of the proposed ALE scheme by forced excitation

The proposed finite-volume ALE scheme is validated by simulating flows around a deforming cylinder. The cylinder is modeled with beam structural elements, and then excited harmonically at one of its ends in the cross flow direction. The uniform flow preserving capability of the proposed ALE scheme is demonstrated with the deforming mesh simulations, and the temporal accuracy of the backward difference formula is also presented.

8.1.1 Truncation error analysis of the temporal discretization

The proposed ALE formulation with a moving mesh source term can be expressed as follows

$$\frac{d\mathbf{U}_i}{dt}V_i + \mathbf{F}_i\left(\mathbf{Q}, \mathbf{x}_f, \dot{\mathbf{x}}_f\right) = \mathbf{G}_i\left(\mathbf{Q}, \mathbf{x}_g\right) + \mathbf{S}_i\left(\mathbf{Q}, \mathbf{x}_s, \dot{\mathbf{x}}_s\right) \tag{8.1}$$

where $\mathbf{F_i}$, $\mathbf{G_i}$ and $\mathbf{S_i}$ are the convective, viscous fluxes and moving mesh source for control volume i, and $\mathbf{x}$ and $\dot{\mathbf{x}}$ are the instantaneous mesh configuration and velocity for the flux or source evaluations.

The temporal discretization of the proposed ALE scheme with second order backward difference formula can be expressed as follows

$$\begin{aligned}&\left(\tfrac{3}{2}\mathbf{U}_i^{n+1} - 2\mathbf{U}_i^n + \tfrac{1}{2}\mathbf{U}_i^{n-1}\right)V_i^{n+1} + \Delta t \sum_{k=1}^{K_f} \alpha_k \mathbf{F}_i\left(\mathbf{Q}^{n+1}, \mathbf{x}_f^{(k)}, \dot{\mathbf{x}}_f^{(k)}\right)\\ &= \Delta t \sum_{k=1}^{K_g} \beta_k \mathbf{G}_i\left(\mathbf{Q}^{n+1}, \mathbf{x}_g^{(k)}\right) + \Delta t \sum_{k=1}^{K_s} \gamma_k \mathbf{S}_i\left(\mathbf{Q}^{n+1}, \mathbf{x}_s^{(k)}, \dot{\mathbf{x}}_s^{(k)}\right)\end{aligned} \tag{8.2}$$

The mesh configurations and velocities for the numerical fluxes and moving mesh source term computation at fictitious time (k) is parameterized as follows

$$\mathbf{x}_f^{(k)} = \varsigma_k^{n+1}\mathbf{x}^{n+1} + \varsigma_k^n \mathbf{x}^n + \varsigma_k^{n-1}\mathbf{x}^{n-1} \tag{8.3}$$

$$\dot{\mathbf{x}}_f^{(k)} = \frac{\theta_k^{n+1}\mathbf{x}^{n+1} + \theta_k^n\mathbf{x}^n + \theta_k^{n-1}\mathbf{x}^{n-1}}{\Delta t} \tag{8.4}$$

$$\mathbf{x}_g^{(k)} = \eta_k^{n+1}\mathbf{x}^{n+1} + \eta_k^n\mathbf{x}^n + \eta_k^{n-1}\mathbf{x}^{n-1} \tag{8.5}$$

$$\mathbf{x}_s^{(k)} = \xi_k^{n+1}\mathbf{x}^{n+1} + \xi_k^n\mathbf{x}^n + \xi_k^{n-1}\mathbf{x}^{n-1} \tag{8.6}$$

$$\dot{\mathbf{x}}_s^{(k)} = \frac{\upsilon_k^{n+1}\mathbf{x}^{n+1} + \upsilon_k^n\mathbf{x}^n + \upsilon_k^{n-1}\mathbf{x}^{n-1}}{\Delta t} \tag{8.7}$$

Proposition 1.

If the parameterization (8.3) to (8.7) satisfies

$$\varsigma_k^{n+1} + \varsigma_k^n + \varsigma_k^{n-1} = 1 \ \ \forall k, \tag{8.8}$$

$$\theta_k^{n+1} + \theta_k^n + \theta_k^{n-1} = 0 \ \ \forall k, \tag{8.9}$$

$$\theta_k^n + 2\theta_k^{n-1} = -1 \ \ \forall k, \tag{8.10}$$

$$\sum_{k=1}^{K_f} \alpha_k = 1, \tag{8.11}$$

$$\sum_{k=1}^{K_f} \alpha_k \left(\varsigma_k^n + 2\varsigma_k^{n-1}\right) = 0, \tag{8.12}$$

$$\sum_{k=1}^{K_f} \alpha_k \left(\theta_k^n + 4\theta_k^{n-1}\right) = 0, \tag{8.13}$$

$$\eta_k^{n+1} + \eta_k^n + \eta_k^{n-1} = 1 \ \ \forall k, \tag{8.14}$$

$$\sum_{k=1}^{K_g} \beta_k = 1, \tag{8.15}$$

$$\sum_{k=1}^{K_g} \beta_k \left(\eta_k^n + 2\eta_k^{n-1}\right) = 0, \tag{8.16}$$

$$\xi_k^{n+1} + \xi_k^n + \xi_k^{n-1} = 1 \ \ \forall k, \tag{8.17}$$

$$\upsilon_k^{n+1} + \upsilon_k^n + \upsilon_k^{n-1} = 0 \ \ \forall k, \tag{8.18}$$

$$\upsilon_k^n + 2\upsilon_k^{n-1} = -1 \ \ \forall k, \tag{8.19}$$

$$\sum_{k=1}^{K_s} \gamma_k = 1, \tag{8.20}$$

$$\sum_{k=1}^{K_s} \gamma_k \left(\xi_k^n + 2\xi_k^{n-1}\right) = 0, \tag{8.21}$$

$$\sum_{k=1}^{K_s} \gamma_k \left(\upsilon_k^n + 4\upsilon_k^{n-1}\right) = 0, \tag{8.22}$$

and the flux and source terms $\mathbf{F}$, $\mathbf{G}$, $\mathbf{S}$ are continuous and sufficiently smooth, then the temporal discretization scheme of the ALE formulation in time is second order accurate.

Proof.

Let

$$\begin{aligned}\Psi_i &= \left(\tfrac{3}{2}\mathbf{U}_i^{n+1} - 2\mathbf{U}_i^{n} + \tfrac{1}{2}\mathbf{U}_i^{n-1}\right) V_i^{n+1} + \Delta t \sum_{k=1}^{K_f} \alpha_k \mathbf{F}_i\left(\mathbf{Q}^{n+1}, \mathbf{x}_f^{(k)}, \dot{\mathbf{x}}_f^{(k)}\right) \\ &-\Delta t \sum_{k=1}^{K_g} \beta_k \mathbf{G}_i\left(\mathbf{Q}^{n+1}, \mathbf{x}_g^{(k)}\right) - \Delta t \sum_{k=1}^{K_s} \gamma_k \mathbf{S}_i\left(\mathbf{Q}^{n+1}, \mathbf{x}_s^{(k)}, \dot{\mathbf{x}}_s^{(k)}\right)\end{aligned} \tag{8.23}$$

denotes the local truncation error where (k) indicates the fictitious time associated with the kth mesh configuration.

If the continuous function $\mathbf{U}$ is sufficiently smooth, $\mathbf{U}$ can be expanded about true time t^{n+1} as follows

$$\mathbf{U}_i^n = \mathbf{U}_i^{n+1} - (\Delta t)\left.\frac{d\mathbf{U}_i}{dt}\right|^{n+1} + \frac{(\Delta t)^2}{2}\left.\frac{d^2\mathbf{U}_i}{dt^2}\right|^{n+1} + O\left(\Delta t^3\right)$$

$$\mathbf{U}_i^{n-1} = \mathbf{U}_i^{n+1} - (2\Delta t)\left.\frac{d\mathbf{U}}{dt}\right|^{n+1} + \frac{(2\Delta t)^2}{2}\left.\frac{d^2\mathbf{U}}{dt^2}\right|^{n+1} + O\left(\Delta t^3\right)$$

An algebraic manipulation of the two Taylor series expansions above yields

$$\begin{aligned}&\left(\tfrac{3}{2}\mathbf{U}_i^{n+1} - 2\mathbf{U}_i^{n} + \tfrac{1}{2}\mathbf{U}_i^{n-1}\right) V_i^{n+1} \\ &= \Delta t \left.\tfrac{d\mathbf{U}_i}{dt}\right|^{n+1} V^{n+1} + O\left(\Delta t^3\right) \\ &= -\Delta t \mathbf{F}_i\left(\mathbf{Q}^{n+1}, \mathbf{x}^{n+1}, \dot{\mathbf{x}}^{n+1}\right) + \Delta t \mathbf{G}_i\left(\mathbf{Q}^{n+1}, \mathbf{x}^{n+1}\right) + \Delta t \mathbf{S}_i\left(\mathbf{Q}^{n+1}, \mathbf{x}^{n+1}, \dot{\mathbf{x}}^{n+1}\right) + O\left(\Delta t^3\right)\end{aligned} \tag{8.24}$$

Local truncation error can be rewritten as follows

$$\begin{aligned}\Psi_i &= \Delta t\left(-\mathbf{F}_i^{n+1} + \mathbf{G}_i^{n+1} + \mathbf{S}_i^{n+1}\right) + O\left(\Delta t^3\right) \\ &+\Delta t \sum_{k=1}^{K_f} \alpha_k \mathbf{F}_i\left(\mathbf{Q}^{n+1}, \mathbf{x}_f^{(k)}, \dot{\mathbf{x}}_f^{(k)}\right) \\ &-\Delta t \sum_{k=1}^{K_g} \beta_k \mathbf{G}_i\left(\mathbf{Q}^{n+1}, \mathbf{x}_g^{(k)}\right) \\ &-\Delta t \sum_{k=1}^{K_s} \gamma_k \mathbf{S}_i\left(\mathbf{Q}^{n+1}, \mathbf{x}_s^{(k)}, \dot{\mathbf{x}}_s^{(k)}\right)\end{aligned} \tag{8.25}$$

where the numerical fluxes and moving mesh source term evaluated at ficticious time (k) are expressed as follows

$$\begin{aligned}&\mathbf{F}_i\left(\mathbf{Q}^{n+1},\mathbf{x}_f^{(k)},\dot{\mathbf{x}}_f^{(k)}\right)\\&=\mathbf{F}_i^{n+1}+\nabla_{\mathbf{x}}\mathbf{F}_i^{n+1}\left(\mathbf{x}_f^{(k)}-\mathbf{x}^{n+1}\right)+\nabla_{\dot{\mathbf{x}}}\mathbf{F}_i^{n+1}\left(\dot{\mathbf{x}}_f^{(k)}-\dot{\mathbf{x}}^{n+1}\right)\\&+O\left(\left\|\mathbf{x}_f^{(k)}-\mathbf{x}^{n+1}\right\|^2\right)+O\left(\left\|\dot{\mathbf{x}}_f^{(k)}-\dot{\mathbf{x}}^{n+1}\right\|^2\right)\end{aligned}$$

$$\mathbf{G}_i\left(\mathbf{Q}^{n+1},\mathbf{x}_g^{(k)}\right)=\mathbf{G}_i^{n+1}+\nabla_{\mathbf{x}}\mathbf{G}_i^{n+1}\left(\mathbf{x}_g^{(k)}-\mathbf{x}^{n+1}\right)+O\left(\left\|\mathbf{x}_g^{(k)}-\mathbf{x}^{n+1}\right\|^2\right)$$

$$\begin{aligned}&\mathbf{S}_i\left(\mathbf{Q}^{n+1},\mathbf{x}_s^{(k)},\dot{\mathbf{x}}_s^{(k)}\right)\\&=\mathbf{S}_i^{n+1}+\nabla_{\mathbf{x}}\mathbf{S}_i^{n+1}\left(\mathbf{x}_s^{(k)}-\mathbf{x}^{n+1}\right)+\nabla_{\dot{\mathbf{x}}}\mathbf{S}_i^{n+1}\left(\dot{\mathbf{x}}_s^{(k)}-\dot{\mathbf{x}}^{n+1}\right)\\&+O\left(\left\|\mathbf{x}_s^{(k)}-\mathbf{x}^{n+1}\right\|^2\right)+O\left(\left\|\dot{\mathbf{x}}_s^{(k)}-\dot{\mathbf{x}}^{n+1}\right\|^2\right)\end{aligned}$$

Substituting the above relations to equation (8.25) yields

$$
\begin{aligned}
&\Psi_i = \Delta t \left\{ \left(\sum_{k=1}^{K_f} \alpha_k \right) - 1 \right\} \mathbf{F}_i^{n+1} \\
&+\Delta t \nabla_{\mathbf{x}} \mathbf{F}_i^{n+1} \left\{ \sum_{k=1}^{K_f} \alpha_k \left(\mathbf{x}_f^{(k)} - \mathbf{x}^{n+1} \right) \right\} \\
&+\Delta t \nabla_{\dot{\mathbf{x}}} \mathbf{F}_i^{n+1} \left\{ \sum_{k=1}^{K_f} \alpha_k \left(\dot{\mathbf{x}}_f^{(k)} - \dot{\mathbf{x}}^{n+1} \right) \right\} \\
&-\Delta t \left\{ \left(\sum_{k=1}^{K_g} \beta_k \right) - 1 \right\} \mathbf{G}_i^{n+1} \\
&-\Delta t \nabla_{\mathbf{x}} \mathbf{G}_i^{n+1} \left\{ \sum_{k=1}^{K_g} \beta_k \left(\mathbf{x}_g^{(k)} - \mathbf{x}^{n+1} \right) \right\} \\
&-\Delta t \left\{ \left(\sum_{k=1}^{K_s} \gamma_k \right) - 1 \right\} \mathbf{S}_i^{n+1} \\
&-\Delta t \nabla_{\mathbf{x}} \mathbf{S}_i^{n+1} \left\{ \sum_{k=1}^{K_s} \gamma_k \left(\mathbf{x}_s^{(k)} - \mathbf{x}^{n+1} \right) \right\} \\
&-\Delta t \nabla_{\dot{\mathbf{x}}} \mathbf{S}_i^{n+1} \left\{ \sum_{k=1}^{K_s} \gamma_k \left(\dot{\mathbf{x}}_s^{(k)} - \dot{\mathbf{x}}^{n+1} \right) \right\} \\
&+\Delta t \left\{ \sum_{k=1}^{K_f} \alpha_k O \left(\left\| \mathbf{x}_f^{(k)} - \mathbf{x}^{n+1} \right\|^2 + \left\| \dot{\mathbf{x}}_f^{(k)} - \dot{\mathbf{x}}^{n+1} \right\|^2 \right) \right\} \\
&-\Delta t \left\{ \sum_{k=1}^{K_g} \beta_k O \left(\left\| \mathbf{x}_g^{(k)} - \mathbf{x}^{n+1} \right\|^2 \right) \right\} \\
&-\Delta t \left\{ \sum_{k=1}^{K_g} \gamma_k O \left(\left\| \mathbf{x}_s^{(k)} - \mathbf{x}^{n+1} \right\|^2 + \left\| \dot{\mathbf{x}}_s^{(k)} - \dot{\mathbf{x}}^{n+1} \right\|^2 \right) \right\} \\
&+O\left(\Delta t^3\right)
\end{aligned}
\tag{8.26}
$$

By using Taylor series expansions of the mesh configurations at time n and $n-1$ about time $n+1$,

$$\mathbf{x}^n = \mathbf{x}^{n+1} - (\Delta t)\, \dot{\mathbf{x}}^{n+1} + O\left(\Delta t^2\right)$$

$$\mathbf{x}^{n-1} = \mathbf{x}^{n+1} - (2\Delta t)\, \dot{\mathbf{x}}^{n+1} + O\left(\Delta t^2\right)$$

The relations of the mesh configurations and velocity between fictitious time (k) and true time $n+1$ can be expressed as

$$\mathbf{x}_f^{(k)} - \mathbf{x}^{n+1} = \left(\varsigma_k^{n+1} + \varsigma_k^{n} + \varsigma_k^{n-1} - 1 \right) \mathbf{x}^{n+1} - \Delta t \left(\varsigma_k^{n} - 2\varsigma_k^{n-1} \right) \dot{\mathbf{x}}^{n+1} + O\left(\Delta t^2\right)$$

$$\begin{aligned}&\dot{\mathbf{x}}_f^{(k)} - \dot{\mathbf{x}}^{n+1} = \tfrac{\left(\theta_k^{n+1}+\theta_k^{n}+\theta_k^{n-1}\right)}{\Delta t}\mathbf{x}^{n+1} - \left(\theta_k^{n} + 2\theta_k^{n-1} + 1\right)\dot{\mathbf{x}}^{n+1} \\ &+\tfrac{\Delta t}{2}\left(\theta_k^{n} + 4\theta_k^{n-1}\right)\ddot{\mathbf{x}}^{n+1} + O\left(\Delta t^2\right)\end{aligned}$$

$$\mathbf{x}_g^{(k)} - \mathbf{x}^{n+1} = \left(\eta_k^{n+1} + \eta_k^{n} + \eta_k^{n-1} - 1\right)\mathbf{x}^{n+1} - \Delta t\left(\eta_k^{n} + 2\eta_k^{n-1}\right)\dot{\mathbf{x}}^{n+1} + O\left(\Delta t^2\right)$$

$$\mathbf{x}_s^{(k)} - \mathbf{x}^{n+1} = \left(\xi_k^{n+1} + \xi_k^{n} + \xi_k^{n-1} - 1\right)\mathbf{x}^{n+1} - \Delta t\left(\xi_k^{n} + 2\xi_k^{n-1}\right)\dot{\mathbf{x}}^{n+1} + O\left(\Delta t^2\right)$$

$$\begin{aligned}&\dot{\mathbf{x}}_s^{(k)} - \dot{\mathbf{x}}^{n+1} = \tfrac{\left(\upsilon_k^{n+1}+\upsilon_k^{n}+\upsilon_k^{n-1}\right)}{\Delta t}\mathbf{x}^{n+1} - \left(\upsilon_k^{n} + 2\upsilon_k^{n-1} - 1\right)\dot{\mathbf{x}}^{n+1} \\ &+\tfrac{\Delta t}{2}\left(\upsilon_k^{n} + 4\upsilon_k^{n-1}\right)\ddot{\mathbf{x}}^{n+1} + O\left(\Delta t^2\right)\end{aligned}$$

Finally the local truncation error can be expressed as follows

$$\begin{aligned}&\Psi_i = \Delta t\left\{\left(\sum_{k=1}^{K_f}\alpha_k\right) - 1\right\}\mathbf{F}_i^{n+1} \\ &+\Delta t^2\left\{\sum_{k=1}^{K_f}\alpha_k\left(\varsigma_k^{n} - 2\varsigma_k^{n-1}\right)\right\}\left(\nabla_{\mathbf{x}}\mathbf{F}_i^{n+1}\right)\dot{\mathbf{x}}^{n+1} \\ &+\tfrac{\Delta t^2}{2}\left\{\sum_{k=1}^{K_f}\alpha_k\left(\theta_k^{n} + 4\theta_k^{n-1}\right)\right\}\left(\nabla_{\dot{\mathbf{x}}}\mathbf{F}_i^{n+1}\right)\ddot{\mathbf{x}}^{n+1} \\ &-\Delta t\left\{\left(\sum_{k=1}^{K_g}\beta_k\right) - 1\right\}\mathbf{G}_i^{n+1} \\ &-\Delta t^2\left\{\sum_{k=1}^{K_g}\beta_k\left(\eta_k^{n} + 2\eta_k^{n-1}\right)\right\}\left(\nabla_{\mathbf{x}}\mathbf{G}_i^{n+1}\right)\dot{\mathbf{x}}^{n+1} \\ &-\Delta t\left\{\left(\sum_{k=1}^{K_s}\gamma_k\right) - 1\right\}\mathbf{S}_i^{n+1} \\ &-\Delta t^2\left\{\sum_{k=1}^{K_s}\gamma_k\left(\xi_k^{n} + 2\xi_k^{n-1}\right)\right\}\left(\nabla_{\mathbf{x}}\mathbf{S}_i^{n+1}\right)\dot{\mathbf{x}}^{n+1} \\ &-\tfrac{\Delta t^2}{2}\left\{\sum_{k=1}^{K_s}\gamma_k\left(\upsilon_k^{n} + 4\upsilon_k^{n-1}\right)\right\}\left(\nabla_{\dot{\mathbf{x}}}\mathbf{S}_i^{n+1}\right)\ddot{\mathbf{x}}^{n+1} + O\left(\Delta t^3\right)\end{aligned} \tag{8.27}$$

and all terms vanish except the third order term by the Proposition 1. Hence the any temporal discretization satisfying the Proposition 1 preserves second order accuracy on moving meshes.

8.1.2 Effect of the moving mesh source term on the uniform flow preserving capability

In order to show the uniform flow preserving capability *via* the moving mesh source term, three cases are compared; namely fixed boundary, moving boundary with source term, and moving boundary without source term, and all under uniform flow with no viscous wall boundary conditions.

A three dimensional cylinder modeled with a beam element is excited harmonically by the following relations.

$$\begin{aligned}
y\left(t\right)_{z=0} &= 0 \\
\theta\left(t\right)_{z=0} &= 0 \\
y\left(t\right)_{z=L} &= \cos\left(t\right) \\
\theta\left(t\right)_{z=L} &= 0
\end{aligned}$$

As the cylinder deforms, the mesh also deformes accordingly by using a deformation weight function, $w\left(r\right)$, defined as

$$w\left(r\right) = \max\left(\frac{r_{\max} - r}{r_{\max} - r_o}, 0\right)$$

where r is the distance from the origin on the plane normal to the spanwise direction, r_o is the radius of the cylinder, and r_{max} is the radius of the zone of the mesh deformation which can be chosen as the shortest distance to the farfield boundary. The weight function is one on the cylinder wall and decreases linearly to zero as we move away from the wall. By using the deformation weight function the mesh points on the cylinder follow exactly its curvature. Fig. 8.1 shows the moving meshes around the structure under deformation.

In Fig. 8.2, we present a comparison of the divergence of the velocity field of the three cases; fixed mesh, moving mesh with the source term, and moving mesh without the source term. It is clear that, with the moving mesh source term, divergence of the velociy field remains zero and the uniform flow is preserved regardless of mesh motion. Without the moving mesh source term, divergence of the velocity field jumps as the mesh deforms, and uniform flow is also not preserved as the mesh starts to deform. Hence, it can be concluded that the proposed ALE scheme is geometrically conservative *via* the moving mesh source term .

8.1.3 Temporal accuracy of the ALE scheme

Temporal accuracy of the presented ALE scheme is verified by using a time step refinement study. The temporal accuracy of the backward difference formula on a fixed mesh configuration is verified, but there is no such result reported for the backward difference formulas applied to the ALE formulation with the moving mesh source term.

In this section, a time step refinement study is presented for the first and second order backward difference formulas applied to the current ALE scheme. The temporal order of accuracy is presented by comparing the solutions with finite time steps to a reference solution obtained with an extremely small time step in lieu of the exact solution.

The comparison of the first and second order backward difference formulae is presented in Fig. 8.3. The C_L responses to the harmonically excited cylinder with uniform inflow is presented with a series of successively refined time steps. For the first order backward difference formula (BDF1), a relatively wide deviation of the C_L response from the reference solution is observed. For the second order scheme (BDF2), the C_L histories are more clustered to the reference solution, which indicates better convergence. The overshoots of the second order scheme at the initial stage of the simulation are attributed to the starting problem of requiring initial conditions one more time step back.

In order to estimate the order of accuracy of the backward difference formulas of the current ALE scheme, a series of successively refined time-steps ($\Delta t =$

$0.4, 0.2, 0.1, 0.05$) are used for the forced excitation problem of the cylinder. Since there is no exact solution for this problem, a reference solution is obtained with extremely small time step ($\Delta t = 0.001$) in lieu of the exact solution. Solution with each finite time step is compared with the reference solution at the nondimensional time $t = 10.0$. As shown in Eq. (8.28), the error is measured in the L^2 sense by computing the difference between the reference and the numerical solutions of finite time steps at every nodal point.

$$Error_{\Delta t} = \sqrt{\frac{\sum\limits_{i=1}^{NI} \left\| \mathbf{Q}_{exact} - \mathbf{Q}_{\Delta t} \right\|^2}{NI}} \tag{8.28}$$

,where NI is total number of nodes and $\mathbf{Q}_{exact}$ is the reference solution obtained with $\Delta t = 0.001$.

Fig. 8.4 shows the decay of error as the time step is refined. The first and second order backward difference formulas show first and second order accuracy respectively. Hence, the time integration schemes used for the current ALE scheme have the same order of accuracy with their fixed mesh counterparts.

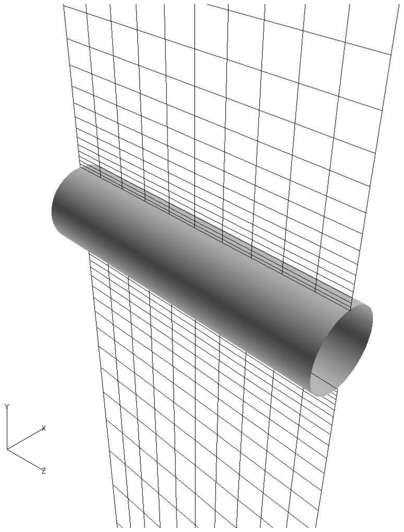

(a) undeformed ($y_{z=L} = 0.0$)

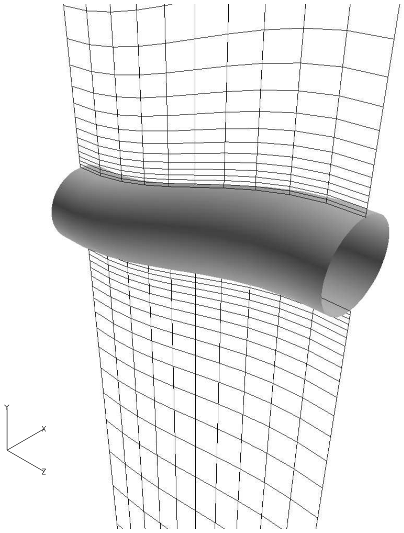

(b) deformed ($y_{z=L} = 1.0$)

Figure 8.1: Forced excitation of the cylinder along the cross flow direction, $L/D = 4.0$ and $Re = 150$.

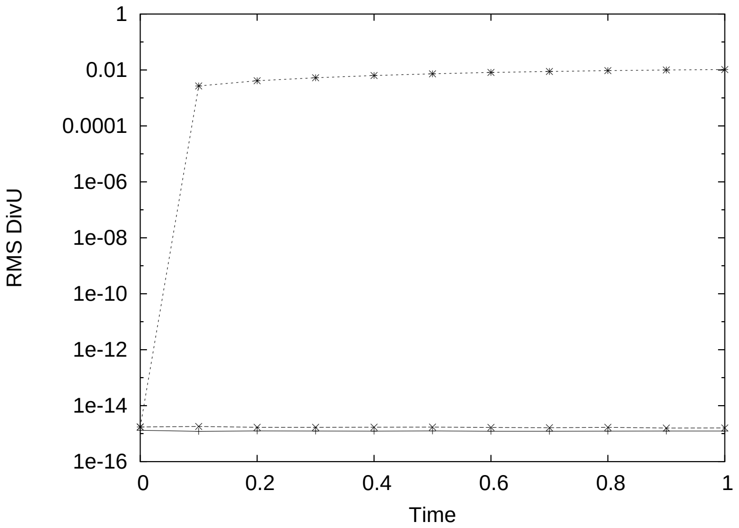

Figure 8.2: Moving mesh source term effect on the uniform flow preserving capability. Solid lines are for fixed mesh, and dashed lines are for the deforming mesh with moving mesh source term, and dotted lines are for deforming mesh without moving mesh source term. Uniform flow boundary (no viscous wall) conditions are applied for all three cases.

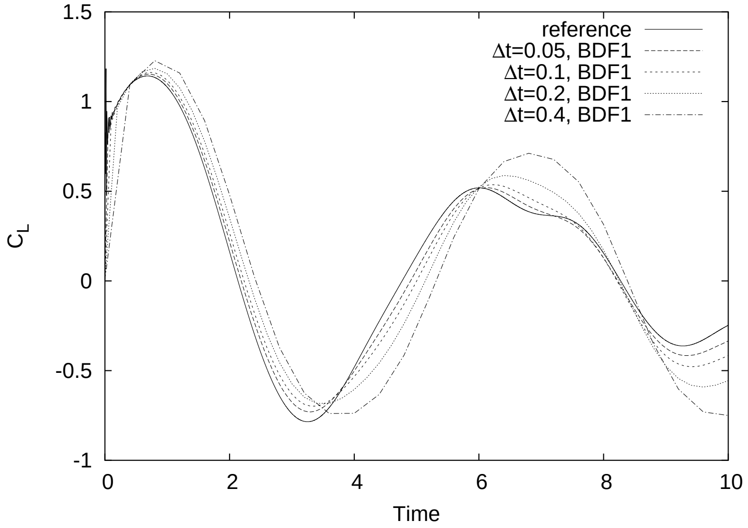

(a) first order backward difference formula (BDF1)

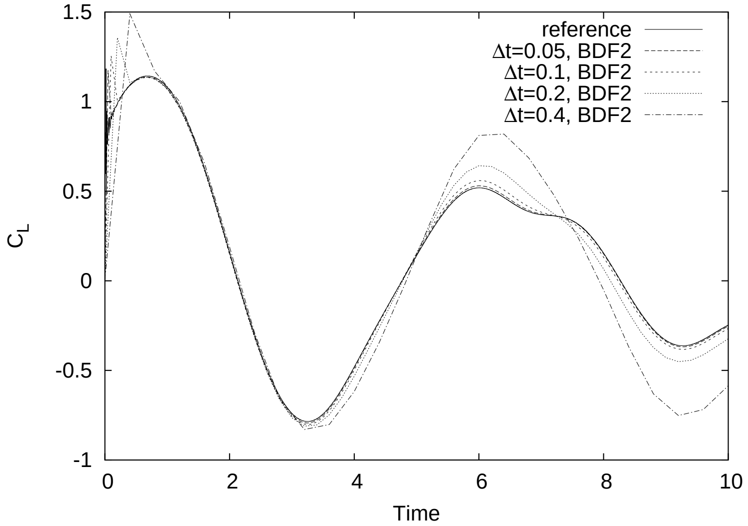

(b) second order backward difference formula (BDF2)

Figure 8.3: C_L responses to the forced excitation

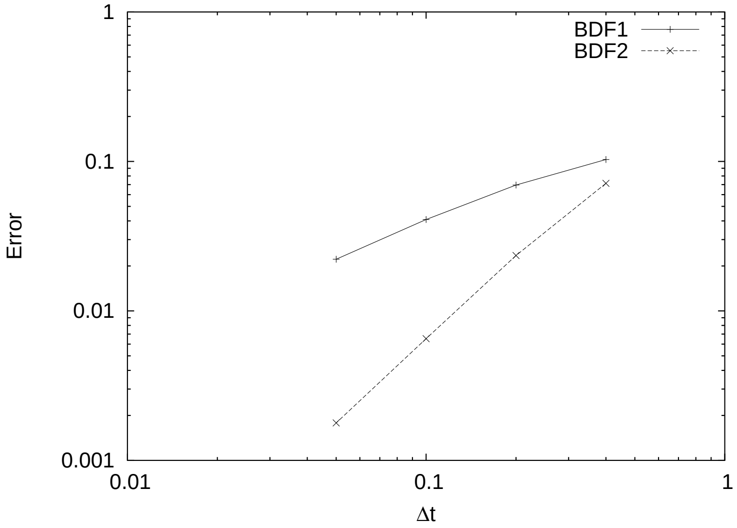

Figure 8.4: Temporal accuracy of the backward difference formulas (BDF) for the proposed ALE scheme. The error is decaying in the order of one for the first order backward difference formula (BDF1) and two for the second order backward difference formula (BDF2).

8.2 Vortex induced vibration of the cylinder

8.2.1 Initial imperfection effect on the initiation of VIV

The development of VIV depends directly on the development of vortex shedding, and the start of vortex shedding typically requires considerable computation time until the assymmetry in the flow field develops and initiates shedding. The initiation of the VIV can be accelerated by applying imperfection on the initial configuration of the cylinder.

As shown in Fig. 8.5, the initial disturbance only accelerates the VIV and results in exactly the same periodic state of VIV when it reaches the lock-in resonant state. As the VIV develops, the displacement at the mid-point of the pinned cylinder is increasing to the maximum amplitude monotonically, while the span averaged lift coefficient shows an overshoot and then settles down to the periodic state, which is attributed to the inertia effect of the cylinder.

8.2.2 Time step refinement study

To be sure about the temporal accuracy of the current VIV simulation, a time step refinement study is presented with the time steps $\Delta t = 0.2, 0.1$, and 0.05. For each one of the time steps, shedding period averaged over the last three shedding cycles are listed in Table 8.1. The order of convergence of the VIV period, T, is estimated by using Richardson's extrapolation, as shown below

$$\log_2\left(\frac{(T)_{\Delta t=0.2} - (T)_{\Delta t=0.1}}{(T)_{\Delta t=0.1} - (T)_{\Delta t=0.05}}\right) = 2.807 \tag{8.29}$$

and this agrees well with the formal accuracy of the three point backward difference formula, which is second order.

The result of the current simulation is compared to other computational results [55], and is in relatively good agreement although a different approach is

Δt	VIV period, T
0.2	6.200
0.1	6.025
0.05	6.000

Table 8.1: VIV periods averaged over the last four cycles.

used. The small difference between the two results seems to be attributed to the differences in structural models, Reynolds number, and the length of the cylinder. For modelling of a high aspect ratio cylinder, a cable model with no bending rigidity can be a reasonable choice, but for a relatively short cylinder, bending rigidity has to be considered. Since the current cylinder model is relatively short ($L/D = 5.0$), the beam elements are chosen in the present study.

structural model	Re	L/D	$max\ y$	$max\ C_L$
beam	150	5.0	0.61	0.27
cable	100	12.6	0.67	0.35

Table 8.2: Comparison of VIV of beam modeled cylinder (current simulation) and cable modeled cylinder (Newman and Karniadakis [55])

8.2.3 VIV with different end conditions

The strong coupling method introduced in the previous section is applied to the flow and structure interaction of a vibrating cylinder. The bending stiffness of the cylinder is modulated such that the natural frequency of the free vibration is approximately equal to the shedding frequency of the fixed cylinder.

We note that, since the element stiffness matrix is also a function of the length of the cylinder, the stiffness of the cylinder will change as its length changes even if the same U_{red} is used. Hence, in order to obtain the lock-in state simulation, the U_{red} has to be chosen accordingly as the length (L/D) of the cylinder changes. One simple way of modulating structural stiffness for the *lock-in* regime VIV simulation is choosing the U_{red} which produces free-vibration (vibration with no hydrodynamic force) at the shedding frequency. For the current model of cylinder ($L/D = 5.0$), $U_{red} = 2.5$ is used for the first mode of pinned-end vibration, and $U_{red} = 5.0$ is chosen for the first mode of clamped-end vibration.

The development of the VIV is presented with the spatio-temporal plots in Fig. 8.7. It is evident that the different end condition produces different patterns in the development of VIV. The maximum amplitude of the clamped-end vibration is a bit higher than the pinned vibration, which is anti-intuitive. The reason is that the bending stiffness modulated by the U_{red} is different, so the cylinder of the clamped-end case becomes more flexible than that of the pinned-end case.

The iso-surfaces of spanwise vorticity and mesh configurations over the vibrating cylinder are displayed in Fig. 8.8 for the pinned-end case and in Fig. 8.9 for the clamped-end condition.

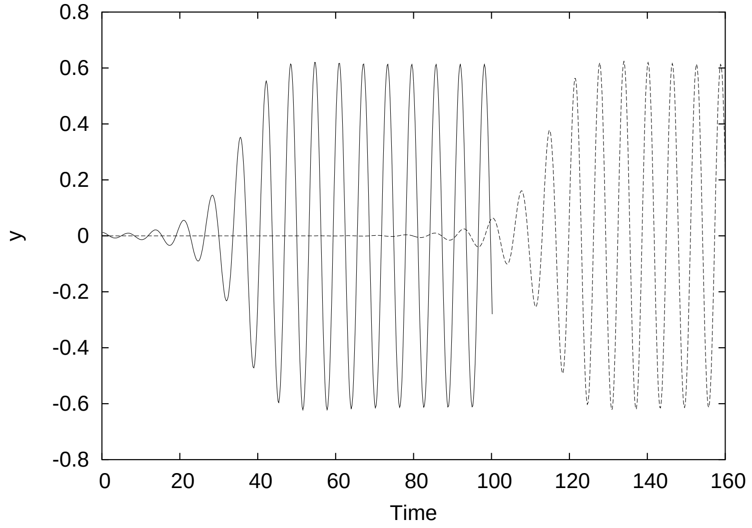

(a) vertical displacement at the midpoint of the cylinder

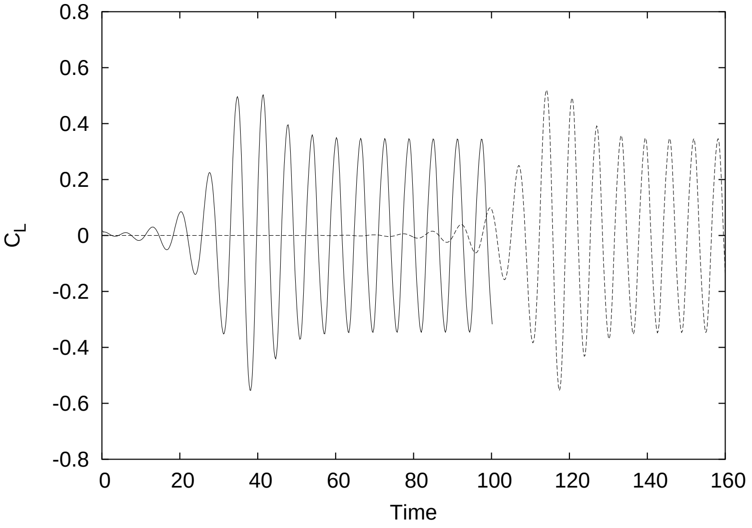

(b) span-averaged lift coefficient of the cylinder

Figure 8.5: Initial disturbance effect on the VIV initiation. Solid lines are with disturbance in the initial cylinder configuration, and the dashed lines are without disturbance. Pinned boundary conditions are applied at both ends and $L/D = 5.0$.

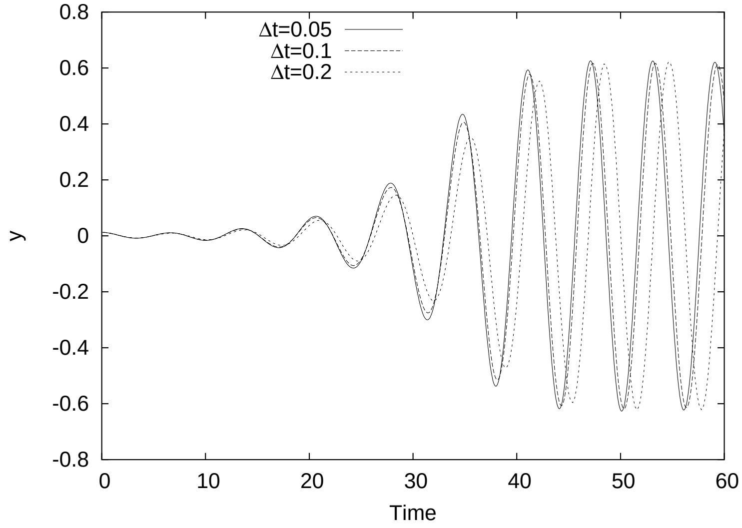

(a) vertical displacement at the midpoint of the cylinder

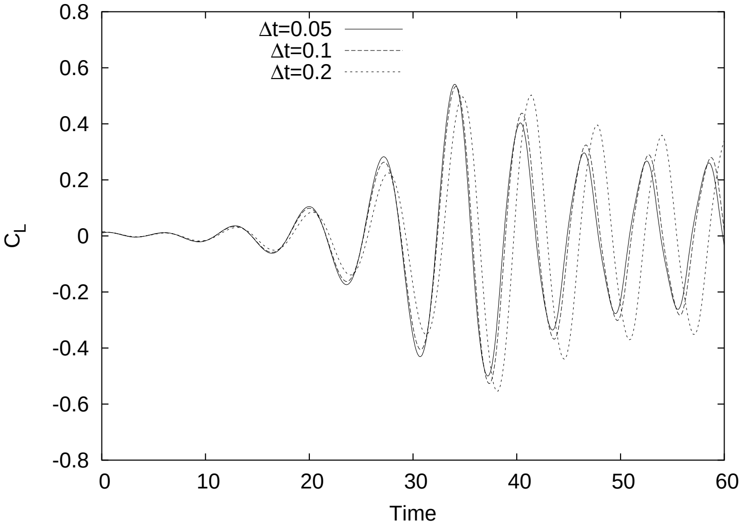

(b) span-averaged lift coefficient of the clyinder

Figure 8.6: Timestep refinement study. Pinned boundary condition is used for both ends of the cylinder, and the same initial disturbance is applied for all three cases. $L/D = 5.0$ and $Re = 150$.

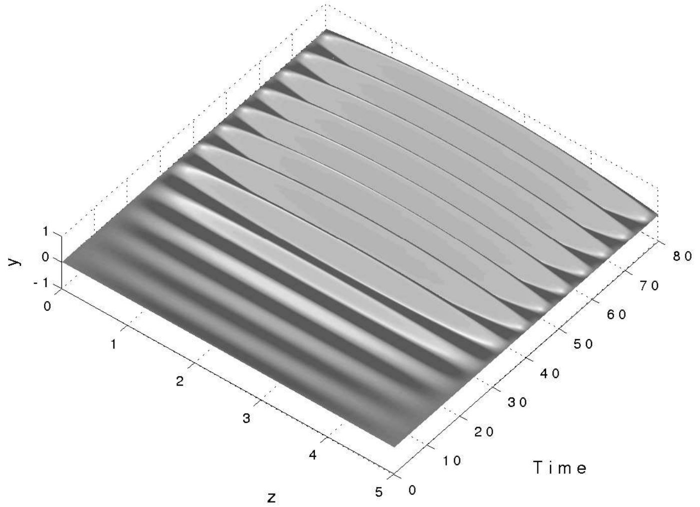

(a) pinned end condition (no translation, free rotation) ($U_{red} = 2.5$)

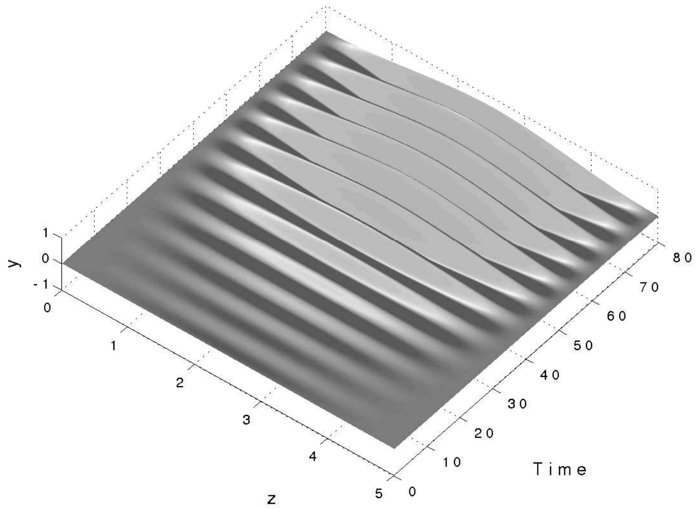

(b) clamped end condition (no translation, no rotation)($U_{red} = 5.0$)

Figure 8.7: Development of VIV with different end conditions. z indicates the spanwise direction of the cylinder, y the amplitude of vibration, and $Time$ the nondimensional time. Both cases started with imperfection in the initial configuration of the cylinder. $L/D = 5.0$ and $Re = 150$.

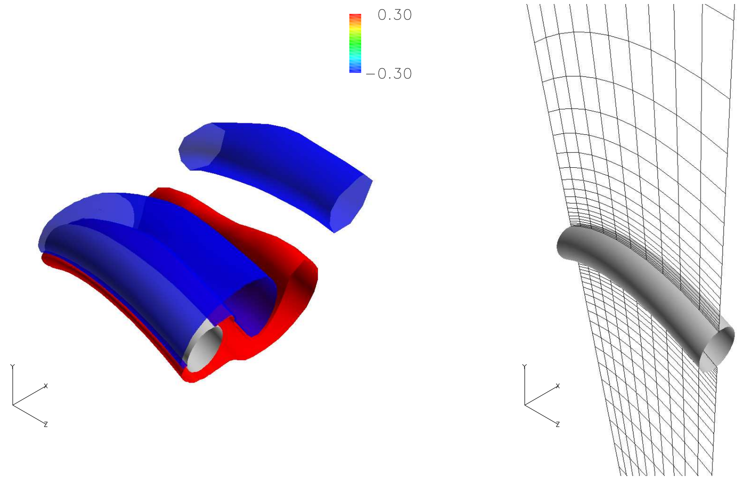

(a) vortex shedding at up-stroke (b) deformed mesh at up-stroke

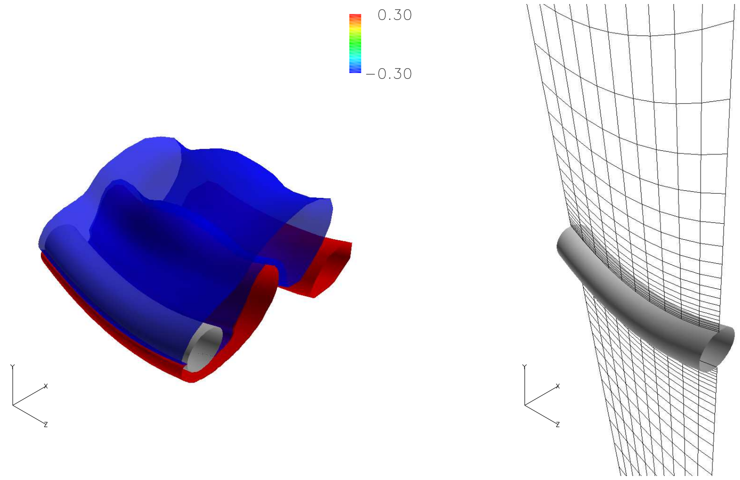

(c) vortex shedding at down-stroke (d) deformed mesh at down-stroke

Figure 8.8: VIV with pinned ends ($U_{red} = 2.5$, $L/D = 5$ and $Re = 150$).

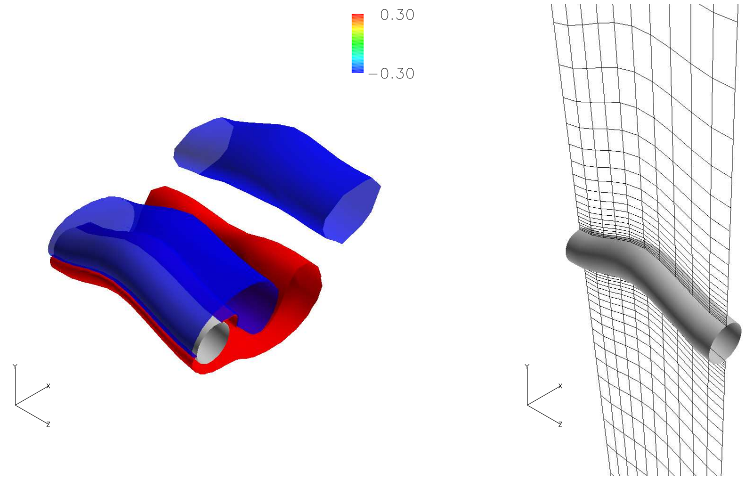

(a) vortex shedding at up-stroke (b) deformed mesh at up-stroke

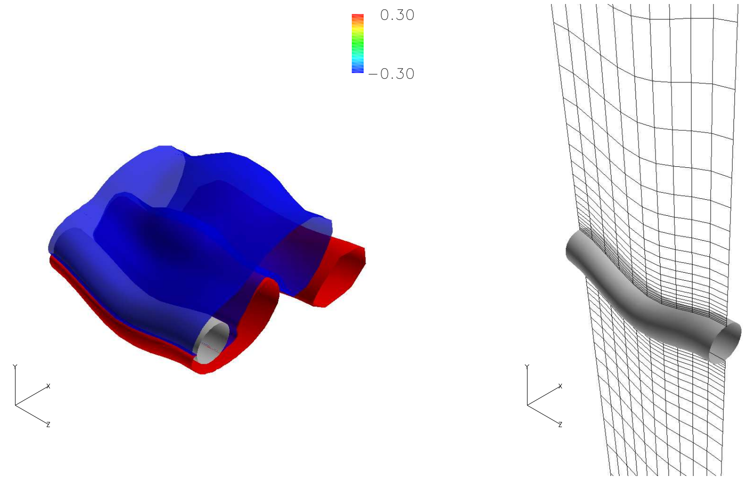

(c) vortex shedding at down-stroke (d) deformed mesh at down-stroke

Figure 8.9: VIV with clamped ends ($U_{red} = 5.0$, $L/D = 5$, and $Re = 150$).

8.3 Comparison between structured and unstructured meshes

A mesh comparison study is presented by using two levels of structured polar meshes and a general hybrid mesh. First, a coarse polar mesh is generated and it is uniformly refined in each coordinate direction in order to get the medium polar mesh. The general hybrid mesh is an unstructured mesh which contains all four types of elements in three dimensions, namely tetrahedra, pyramids, prisms, and hexahedra. The boundary of the circular cylinder from the three meshes are displayed in Fig. 8.10 and characteristics of the meshes are listed in Table 8.3.

Vortex induced vibration with clamped-sliding end condition is simulated with the three meshes, and the results are compared.

structural model	coarse polar	medium polar	hybrid
E_{total}	11,520	92,160	509,269
N_{total}	13,024	98,112	148,719
N_{circum}	32	64	74
Δr_0	0.004	0.002	0.0009
R_{ffd}	15.5	15.5	6.0

Table 8.3: Characteristics of the two levels of structured polar meshes and the general hybrid mesh. E_{total} refers to the total number of elements, N_{total} to the total number of nodes, N_{circum} to the number of nodes on the cylinder along the circumferential direction, Δr_0 is for the initial spacing on viscous wall, R_{ffd} is far field distance from the center of the cylinder. All length units are non-dimensionalized with respect to the cylinder diameter.

The vortex shedding over the vibrating cylinder is displayed in Fig. 8.11 for three meshes. Iso-vorticity surfaces near the vibrating cylinder is similar for all three meshes. The difference in iso-vorticity surface downstram seems attribute to several factors, for example mesh resolution, domain size and shape, and etc. The development of VIV is displayed in Fig. 8.12. In generally, as mesh becomes fine, the amplitude of cylinder displacement converges.

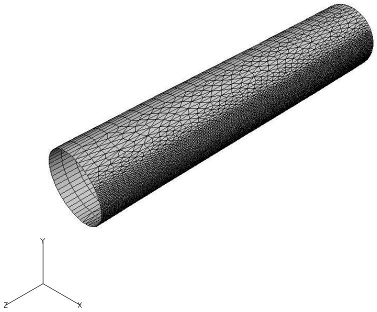

(a) hybrid mesh

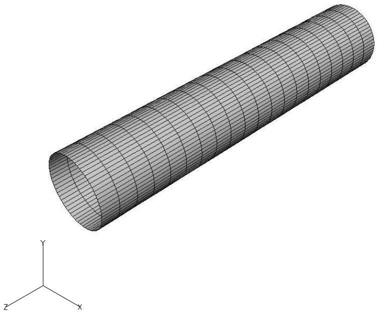

(c) medium polar mesh

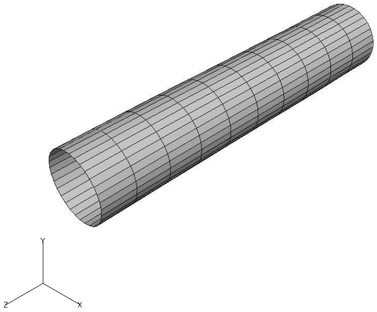

(c) coarse polar mesh

Figure 8.10: Three meshes used for mesh convergence study, $L/D = 5$.

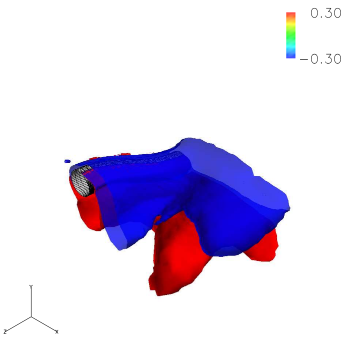

(a) hybrid mesh

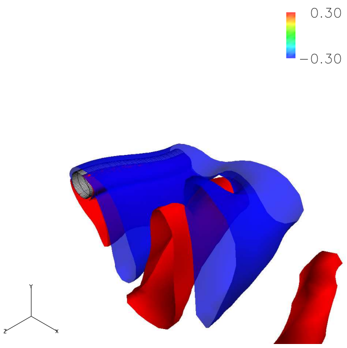

(c) medium polar mesh

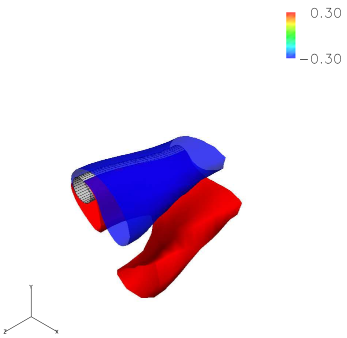

(c) coarse polar mesh

Figure 8.11: Vortex shedding patterns over vibrating cylinder, $U_{red} = 1.2$, $L/D = 5$, and $Re = 150$. clamped-sliding end conditions applied for all cases. Iso-surfaces of span-wise vorticity are displayed over the cylinder at up-stroke.

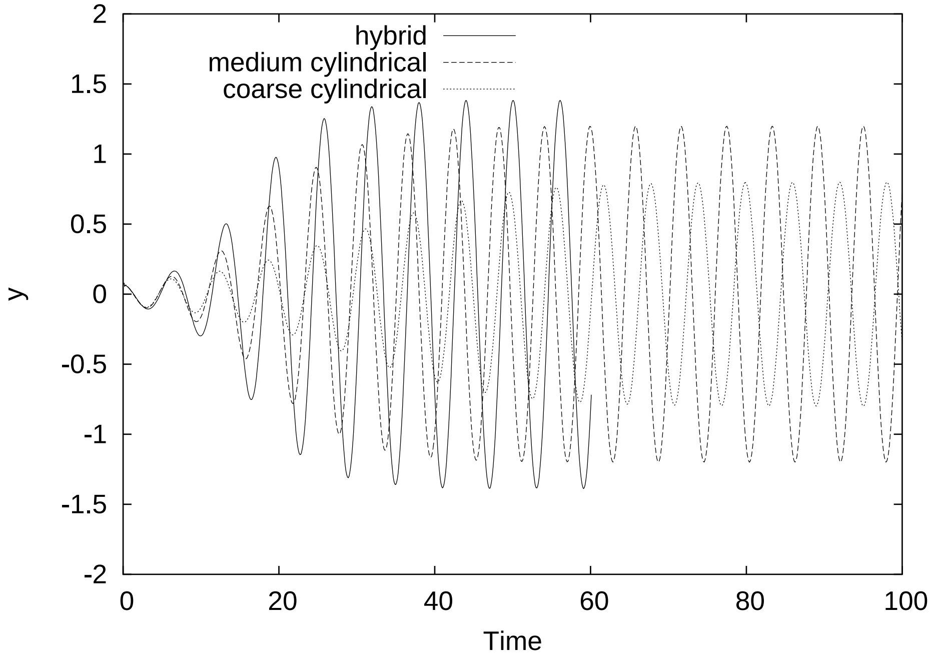

Figure 8.12: Displacement of the cylinder at right end ($L/D = 5.0$) with different mesh resolutions. Clamped-sliding end conditions are applied. $U_{red} = 1.2$ and $Re = 150$.

Chapter 9

Parallelization

A parallel implementation of the presented solution algorithms for general hybrid meshes is presented for a distributed memory machine by using the message passing interface (MPI) library. Two different partitioning methods are introduced; namely graph partitioning and mesh partitioning. An overlapping interface cell strategy is employed in order to reduce the inter-processor communication phases. A single loop interprocessor communication algorithm is introduced and the associated pseudo-code is given. Scalability of the proposed parallel algorithm is presented.

9.1 Partitioning methods

Quality of partitioning a computational domain is critical for optimal load balancing of the parallel computation. Two strategies can be used to partition a given mesh; graph partitioning and mesh partitioning. Graph partitioning is a partitioning method that distributes nodes as evenly as possible (assuming all nodes have the same weight) with the minimum possible number of edge-cuts. Since graph partitioning is assigning a unique part number to each node, it can also be called as node partitioning. On the other hand, in mesh partitioning, elements are distributed as evenly as possible with the minimun number of interface nodes. The two partitioning methods are delineated in Figure 9.1. For both methods, the common objective is equi-distribution of the computational load (nodes,edges,faces, and cells) with the minimum amount of interface identities (nodes, edges, faces, or cells on interface) which is the indicator of inter-partition communication load.

If a mesh is composed of only a single type of elements, then mesh partitioning can be a choice for domain decomposition. However, if a mesh includes multiple types of elements, mesh partitioning is not an obvious task and no mesh partitioner is available yet which can handle general hybrid meshes.

In graph partitioning, general hybrid meshes can be handled without extra complexity. A graph, by definition, is *a finite set of vertices (or nodes) connected by edges* [16], and does not include any information about element-wise connectivity. In the current node-based scheme, all unknowns are stored at nodes and the conservation laws are solved about the finite control volume around a node. Hence, graph partitioning (distributing nodes evenly) can be the optimal choice for equi-distribution of the computational load at least from the memory requirement point of view. Therefore, graph partitioning is chosen as the partitioning method for general hybrid meshes in the present parallel simulations. A graph partitioned general hybrid mesh is shown in Figure 9.2.

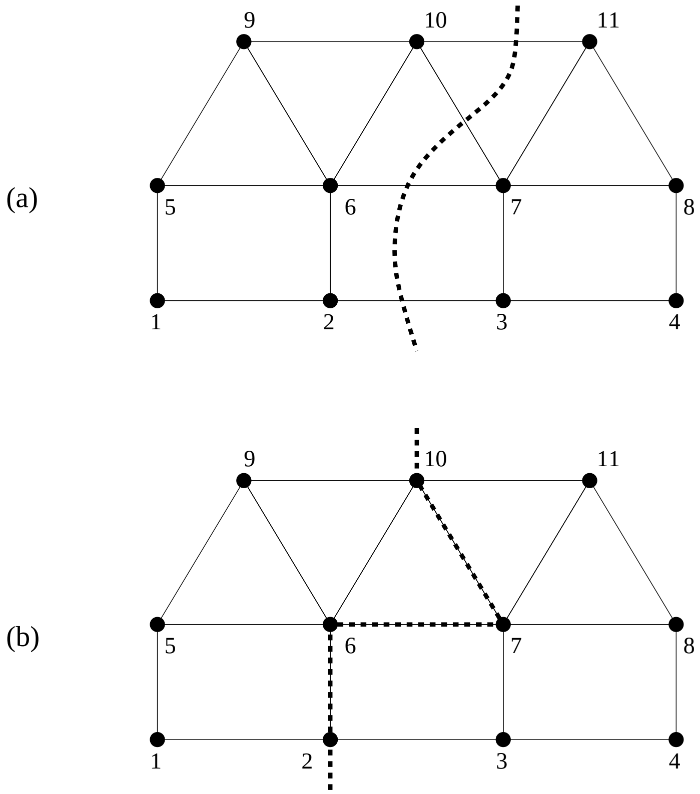

Figure 9.1: Partitioning strategies; (a) Graph partitioning (distribution of nodes) and (b) Mesh partitioning (distribution of elements).

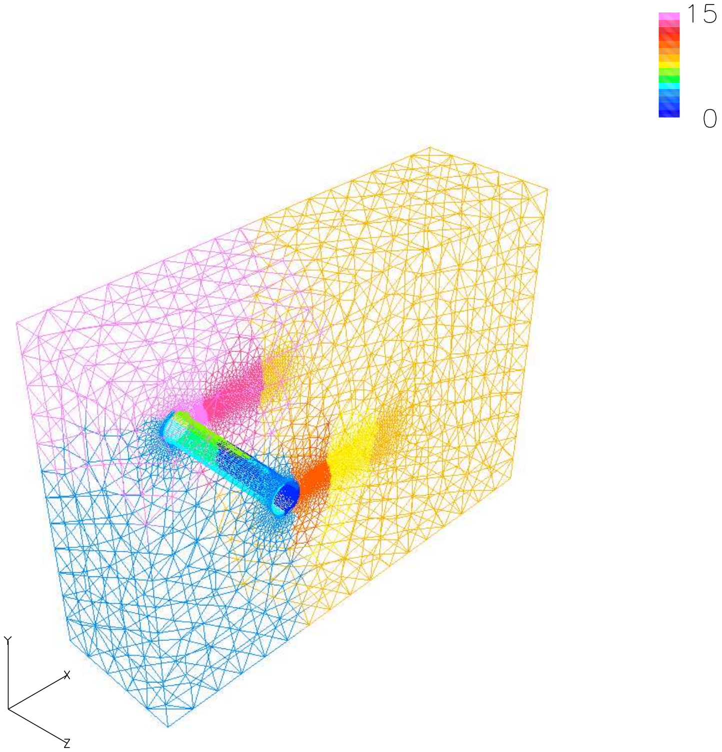

Figure 9.2: Graph partitioned general hybrid mesh-1 into 16 partitions. Each color represents a separate partition.

9.2 Hybrid mesh data structure for parallel execution

A parallel implementation of the current solution algorithms for general hybrid meshes is presented for a distributed memory machine by using MPI (message passing interface) library functions [58]. The original mesh is partitioned by the METIS graph partitioning strategy, an open source graph/mesh partitioner [37]. As mentioned before, graph partitioning is the strategy of distributing nodes as evenly as possible with the minimum number of possible edge-cuts. The interface elements, whose nodes are assigned to multiple parts, are stored redundantly in the neighbor parts in order to reduce the communication phases. The hybrid mesh data structure for parallel execution is presented for the inter-processor communication. A pseudo-code for a single loop inter-processor communication algorithm is presented. Finally, the scalability of the parallel implementation is measured on a distributed memory machine. The communication overhead is estimated by counting the number of nodes participating in the inter-processor communication among all nodes.

9.2.1 Inter-processor communication strategy

The current flow solver is parallelized using the graph partitioning strategy of METIS [37]. A given mesh can be partitioned either by graph partitioning [48, 84] or by mesh partitioning [52, 51]. Graph partitioning distributes nodes to each part, and mesh partitioning distributes elements to each part. Since graph partitioning distributes nodes to parts, it can be called node partitioning in contrast to mesh partitioning. In mesh partitioning strategy, equi-distribution of elements is not an obvious task especially if the mesh includes multiple element types. In graph (node) partitioning, the algorithm is transparent to cell topologies and node-connectivity is the only information required by the partitioner. Hence, the graph (node) partitioning strategy can be directly applied to general hybrid meshes. Furthermore, since the current node-based scheme stores unknowns at the nodes, distributing nodes

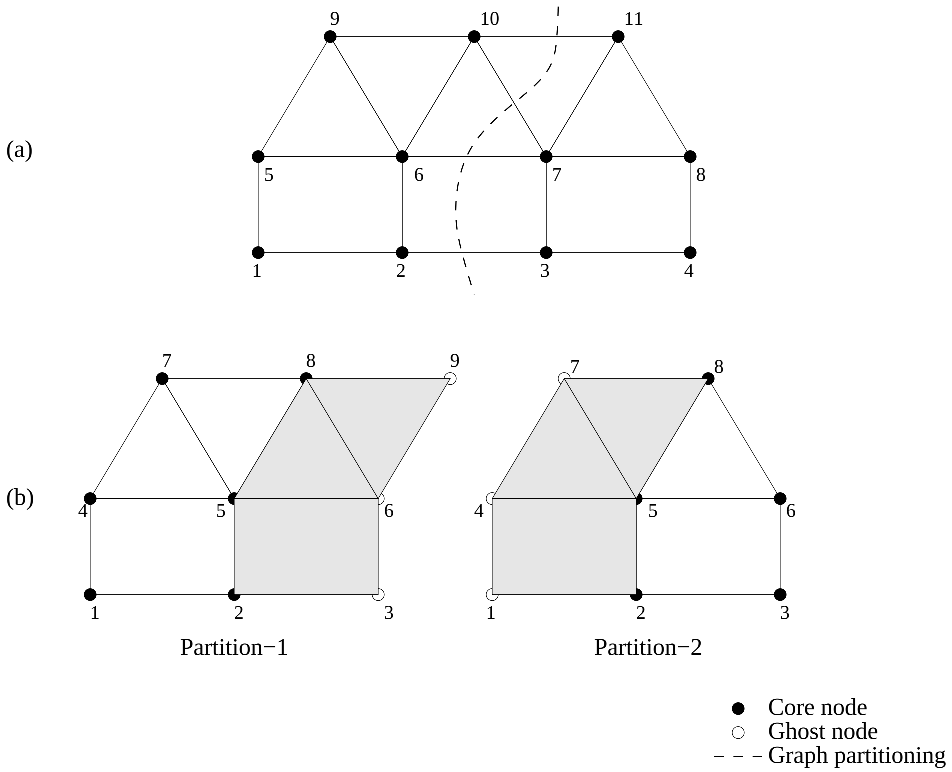

Figure 9.3: Graph partitioning of a two-dimensional hybrid mesh with overlapping interface cells (cells in gray color). (a) original hybrid mesh with global node numbering, and (b) partitioned hybrid meshes with local node numbering.

send to	*local(global)*	recv from	*local(global)*
2	2(2) 5(6) 8(10)	2	3(3) 6(7) 9(11)

(a) communication for the partition-1

send to	*local(global)*	recv from	*local(global)*
1	2(3) 5(7) 8(11)	1	1(2) 4(6) 7(10)

(b) communication table for partition-2

Table 9.1: Communication tables for the node-wise inter-processor communications. the *local* is local node numbering and *global* is global node numbering.

equivalently seems the most reasonable choice. Hence, the current parallelization strategy is based on graph (node) partitioning rather than mesh partitioning.

The parallel implementation of the current study basically follows the strategy of Tai and Zhao [84]. The main idea of their implementation is overlapping the interface cells, whose nodes are assigned to multiple parts. This may look as an overhead of memory space. However, once an explicit scheme is parallelized on a distributed memory machine, the amount of memory required for each processor is no longer the critical issue, but the amount of communication is.

By overlapping the interface cells, the communication amount can be reduced considerably. For the current scheme, only two phases (times) of node-wise inter-processor communication can be achieved per solution update. The first communication is for exchanging the nodal gradients of the state, which is required for the solution reconstructions for the artificial dissipation or the high order upwind scheme. The second communication phase is at the boundary condition application routine which is called after an intra-processor solution update. Once all the nodal solutions are updated, the solutions at the ghost nodes, which reside at the inter-processor boundaries, are updated by node-wise inter-processor communication. This overlapping strategy of general hybrid mesh partitioning is delineated in Fig. 9.3 in two dimensions. An example of the information required for the inter-processor communication is listed in Table 9.1.

On the other hand, without overlapping the interface cells, the inter-processor communication may introduce more phases of communication as well as extra complexity of the communication routines. For example, in the overlapping strategy no extra communication is needed for the viscous flux computation, while in the non-overlapping strategy there should be extra communication regarding the computation using edge-duals which lie on the inter-processor boundaries.

According to the partitioning strategy presented in Fig. 9.3, there is no such assumption that each part has to be contiguous. A completely separate part of the original mesh can be assigned to the same processor. This is also a big flexibility for the graph partitioner, which may produce a non-contiguous partitioning, even though very rarely.

Each part has its own local node numbering, and the translation table of the local node number to the global node number (and *vice versa*) is required for the communications with its neighbors. Once the communication table is built for all processors (parts), the inter-processor communication can be implemented by a single loop that runs through the processors. The pseudo-code of the proposed inter-processor communication is shown below.

```
for $i = 1, \cdots, N_{procs}$
  if $i$ is equal to $my\_id$
    for $j = 1, \cdots, N_{my\ neighbors}$
```

```
      send nodal values to my $j_{th}$ neighbor
    end
  else
    for $j = 1, \cdots, N_{my\ neighbors}$
      if $i$ is equal to my $j_{th}$ neighbor
        receive nodal values from $i$
    end
end
```

When an inter-processor communication is needed, the loop as presented in the above pseudo-code runs on all processors. This strategy follows exactly the SPMD (single-program multiple-data) paradigm. All processors simultaneously get involved in the communication with their neighbors, and this enables the parallel data-exchange. This single-loop parallel data-exchange does not require any *a priori* optimal scheduling of communication order, and results in a simpler algorithm.

9.2.2 Scalability

The scalability of a given algorithm (program) on a specific machine can be different depending on the problem size, that is, the total number of nodes in the original mesh. Typically the larger the problem size, the higher scalability. For the performance check of the current parallel implementation scheme, a general hybrid mesh of 148,719 nodes is used.

The performance of the parallel implementation was measured on a Linux cluster. As shown in Fig. 9.4, the speed-up of the current parallel execution is almost linear up to 16 processors and then it starts to deviate from the ideal and becomes sub-linear. This deviation of the actual computation from the ideal is due to the increase of communication load.

According to the current parallel implementation strategy, there are core

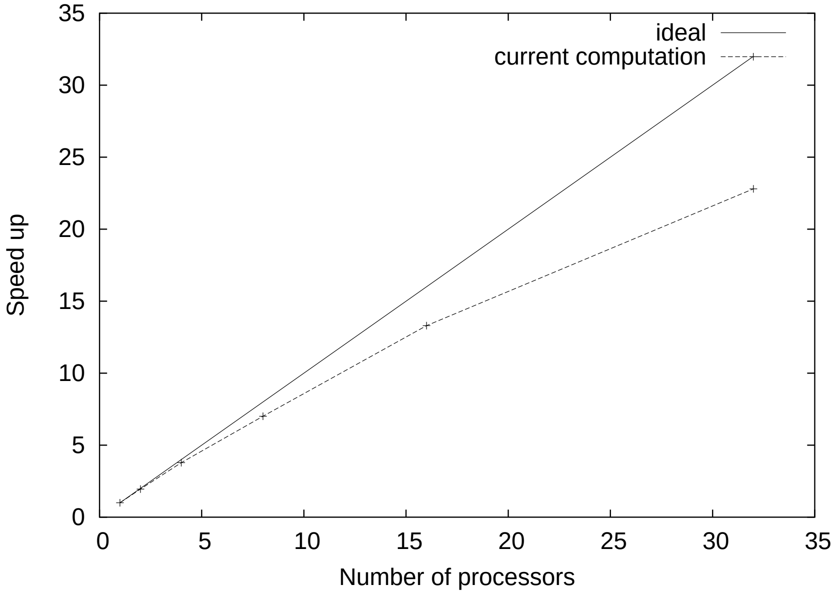

Figure 9.4: Scalability of the parallel implementation. Measurd on a Linux cluster by using the general hybrid mesh-1 containing 148,719 nodes.

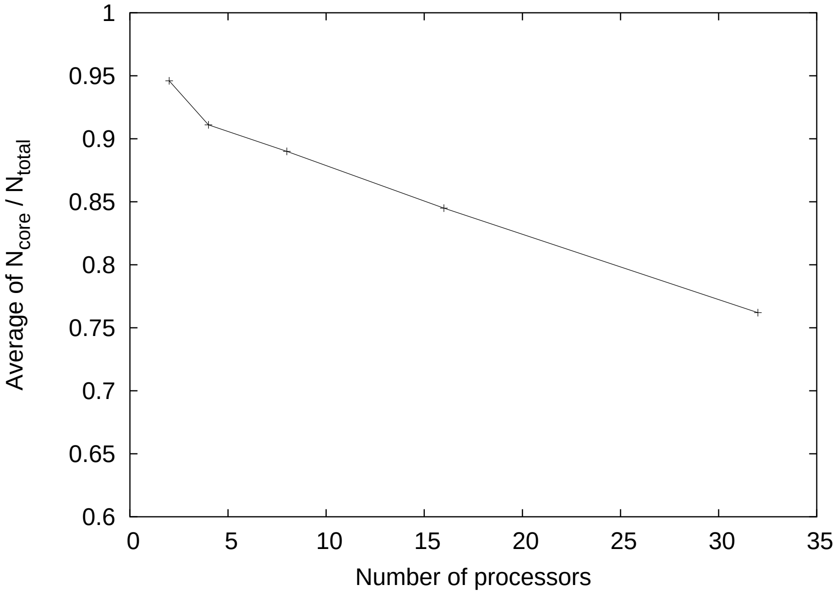

Figure 9.5: Portion of core nodes with respect to the total number of nodes assigned to the part. The ratio is averaged from all parts. The total number of nodes for each part is the sum of core nodes and ghost nodes, and the solutions at the ghost nodes are to be received from other parts having the ghost nodes as core nodes. Measured with a general hybrid mesh of 148,719 nodes.

nodes and ghost nodes at each processor. The total number of nodes at each part is composed of the core nodes and ghost nodes. Solutions at the core nodes can be updated without inter-processor communications, but the solution at a ghost node needs to be received from its neighbor processor which contains the ghost as the core. Hence, as the number of partitions increases, the number of ghost nodes also increases as shown in Fig. 9.5. This becomes directly a communication overhead, and is also one of the major reasons for the deviation of speed-up from the ideal. Even with the rapid increase of the ghost nodes among the total nodes at each part, the parallel performance is fairly ideal, and this is because of the smaller number of communications required by the current parallel algorithm.

Chapter 10

Conclusions

In this last chapter, first the major contributions made in this research are summarized, and then conclusions are drawn from the presented results. Finally, recommendations are presented for future research efforts.

10.1 Contributions

The contributions made in this research can be categorized as follows

1. development of an incompressible Navier-Stokes method for the general hybrid meshes
2. application of the method to inflow turbulence study
3. extension of the method to arbitrary Lagrangian-Eulerian (ALE) formulations
4. application of the ALE scheme to the fluid and structure interaction problems

First, a new grid transparent algorithm for the incompressible Navier-Stokes equations has been presented on the general hybrid meshes with hexahedra, prisms, pyramids, and tetrahedra. A computationally efficient edge-based algorithm is used for the numerical flux computations. Especially for the viscous flux evaluations, a new computationally efficient two-step *face-and-edge* algorithm has been presented. The computational efficiency and solution accuracy of the general hybrid meshes with local hexahedra are investigated. The local hexahedra are introduced into the viscous layers and also into the wake regions. For both of the cases, the general hybrid meshes with local hexahedra are shown to be giving as accurate result as the meshes with prisms/tetrahedra with less computational cost. The proposed scheme is parallelized for distributed memory machines. Hybrid mesh data structure for parallel execution was illustrated, and a single-loop inter-processor communication algorithm was presented. The scalability of the proposed parallelization method is also presented. The communication overhead is estimated by presenting the growth of the number of interface nodes among the total nodes as the number of processor increases.

Second, by using the developed and validated flow solution algorithm, the effect of inflow turbulence is studies. Local mesh refinement is also performed to identify the effect of mesh resolution capturing the inflow turbulent eddies. The effect of the inflow turbulence is more emphasized by comparisons with uniform inflow cases.

Third, a geometrically conservative finite-volume ALE scheme is presented with moving mesh source term. The moving mesh source term is derived from the physical conservation laws for an arbitrarily moving control volume and the geometric conservation law. The significance of the moving mesh source term is demonstrated by presenting the uniform flow preserving capability on arbitrarily deforming meshes. The temporal accuracy of the time-integrators, the backward difference formulas, used for the ALE scheme is verified by time step refinement study.

Lastly, the presented ALE scheme is applied to the fluid structure interaction problem. The vortex induced vibration of cylinder is simulated by using the presented ALE scheme. Different coupling strategies, namely weak and strong, are presented and the superior stability of the strong coupling method is emphasized. By using beam structural elements for modeling of the cylinder, the applicability of the proposed scheme for the different types of end-condition are demonstrated.

10.2 Conclusions

The following conclusions can be drawn from the present work:

First, *general hybrid meshes can be utilized for accurate simulations of incompressible viscous flows with less computational cost compared to conventional meshes.* The general hybrid meshes, containing tetrahedra, pyramids, prisms, and hexahedra in a single computational domain, was successfully applied for incompressible viscous flow simulations. Local hexahedra are introduced into various regions of computational domain, and its effectiveness was demonstrated.

Second, *the developed incompressible Navier-Stokes method can be applied to the various types of flow physics study.* Through the extensive verification and validation study, the accuracy and robustness of the solution method is presented. By applying the method successfully to the inflow turbulence effect study, it has been shown that the method can be utilized for various types of flow physics investigational study.

Third, *moving mesh simulations can be performed accurately by using the presented ALE scheme.* A geometrically conservative property of the proposed finite volume ALE scheme was presented. The significance of the moving mesh source term was emphasized (as shown in Figure 8.2) for accurate simulation of moving mesh simulations. Second order temporal accuracy was also verified (as shown in Figure 8.4) for the proposed ALE time-integration scheme on moving meshes. By applying the present ALE scheme, it was shown that moving mesh simulations can be performed more accurately.

Finally, *By using strong coupling method, the developed flow simulation algorithm can be coupled with simulations in different physical regimes.* Strong coupling method of fluid and structure interaction was presented. The improved stability of the strong coupling is emphasized by comparison with that of weak coupling (shown in Figure 7.4). By coupling the fluidic and structural fields strongly, a stable and accurate coupling method was presented for multi-physical system simulations.

10.3 Recommendations for future research

The following recommendations can be given for future research based on the current work. As the first category, convergence acceleration techniques are suggested for further developed. Even though the current scheme is accelerated with point-implicit (diagonal-implicit) local pseudo time stepping scheme, the convergence is still critical to the convergence rate in pseudo transient state. Hence, more sophisticated convergence acceleration scheme is encouraged to be applied, for examples multi grid scheme and full matrix preconditioning scheme.

As the second category, the developed method can be applied to multidisciplinary research. For examples, the flow solution method can be applied coupled with flow control problems, and the moving mesh capability could be used with shape optimization research.

As the last category, further investigation of moving mesh method is encouraged. Since various approaches are in the fields, for examples, space-time method, fictitious domain method and immersed boundary method, a comparison study also can be made between those different methods, and further improvement can be made.

Bibliography

[1] E. Achenbach. Influence of surface roughness on the cross-flow around a circular cylinder. *Journal of Fluid Mechanics*, 46:321–335, 1971.

[2] E. Achenbach. Experiments on flow past spheres at very high reynolds numbers. *Journal of Fluid Mechanics*, 54:565–575, 1972.

[3] W. K. Anderson and D. L. Bonhaus. Algorithm for computing turbulent flows on unstructured grids. *Computers & Fluids*, 23:1–21, 1994.

[4] W. K. Anderson, R. D. Rausch, and D. L. Bonhaus. Implicit/multigrid algorithms for incompressible turbulent flows on unstructured grids. *Journal of Computational Physics*, 128:391–408, 1996.

[5] G. A. Ashford. *An Unstructured Grid Generation and Adaptive Solution Technique For High-Reynolds-Number Compressible Flows.* PhD thesis, University of Michigan, 1996.

[6] A. Belov, A. Jameson, and L. Martinelli. A new implicit algorithm with multigrid for unsteady incompressible flow calculations. *AIAA Paper 95-0049*, 1995.

[7] Andrey A. Belov. *A new implicit multigrid-driven algorithm for unsteady incompressible flow calcuations on parallel computers.* PhD thesis, Princeton University, 1997.

[8] M. E. Braaten and S. D. Connell. Three-dimensional unstructured adaptive multigrid scheme for the Navier-Stokes equations. *AIAA Journal*, 34:281–290, 1996.

[9] K.S. Chang and J.Y. Sa. Patterns of vortex shedding from an oscillating circular cylinder. *AIAA Journal*, 30:1331–1336, 1992.

[10] A. J. Chen and Y. Kallinderis. Adaptive hybrid (prismatic-tetrahedral) grids for incompressible flows. *International Journal for Numerical Methods in Fluids*, 26:1085–1105, 1998.

[11] X. Chen, G. Zha, and Z. Hu. Numerical simulation of flow induced vibration based on fully coupled fluid-structural interactions. *AIAA Paper 2004-2240*, 2004.

[12] Y.H. Choi and C.L. Merkle. The application of preconditioning in viscous flows. *Journal of computational physics*, 105:207–223, 1993.

[13] A. J. Chorin. A numerical method for solving incompressible viscous flow problems. *Journal of Computational Physics*, 2:12–26, 1967.

[14] Robert D. Cook, David S. Malkus, and Michael E. Plesha. *Concepts and Applications of Finite Element Analysis*. John Wiley & Sons, 1989.

[15] G. Dahlquist. *Numerical Methods*. Prentice-Hall, 1974.

[16] Reinhard Diestel. *Graph Theory (Graduate Texts in Mathematics, 173)*. Springer-Verlag, 2000.

[17] C. Evangelinos and G.E. Karniadakis. Dynamics and flow structures in the turbulent wake of rigid and flexible cylinders subject to vortex-induced vibrations. *Journal of Fluid Mechanics*, 400:91–124, 1999.

[18] C. Farhat, P. Geuzaine, and G. Brown. Application of a three-field nonlinear fluid-structure formulation to the prediction of the aeroelastic parameters of an f-16 figher. *Computer & Fluids*, 32:3–29, 2003.

[19] C. Farhat, P. Geuzaine, and C. Grandmont. The discrete geometric conservation law and the nonlinear stability of ale schemes for the solution of flow problems on moving grids. *Journal of computational physics*, 174:669–694, 2001.

[20] P. Geuzaine, C. Grandmont, and C. Farhat. Design and analysis of ale schemes with provable second-order time-accuracy for inviscid and viscous flow simulations. *Journal of computational physics*, 191:106–227, 2003.

[21] M.B. Giles. Nonreflecting boundary conditions for euler equation calculations. *AIAA Journal*, 28:2050–2058, 1990.

[22] M.B. Giles. Preconditioned multigrid methods for compressible flow calculations on stretched meshes. *Journal of Computational Physics*, 136:425–445, 1997.

[23] M.B. Giles. Stability and accuracy of numerical boundary conditions in aeroelastic analysis. *International Journal for Numerical Methods in Fluids*, 24:739–757, 1997.

[24] P. Godin, D. W. Zingg, and T. E. Nelson. High-lift aerodynamic computations with one and two- equation turbulence models. *AIAA Journal*, 35:237–243, 1997.

[25] P. M. Gresho. Incompressible fluid dynamics: Some fundamental formulation issues. *Annual Review of Fluid Mechanics*, 23:413–53, 1991.

[26] P. M. Gresho. Some current CFD issues relevant to the incompressible Navier-Stokes equations. *Computer Methods in Applied Mechanics and Engineering*, 87:201–252, 1991.

[27] F. H. Harlow and J. E. Welch. Numerical calculation of time-dependent viscous incompressible flow of fluid with free surface. *Physics of Fluids*, 8:2182, 1965.

[28] A. Haselbacher and J. Blazek. On the accurate and efficient discretization of the Navier-Stokes equations on mixed grids. *AIAA Journal*, 38:2094–2102, 2000.

[29] C.W. Hirt, A.A. Amsden, and J. L. Cook. An arbitrary lagrangian-eulerian computing method for all flow speeds. *Journal of Computational Physics*, 14:227–253, 1974.

[30] Daniel J. Inman. *Engineering Vibrations*. Prentice Hall, 2000.

[31] A. Jameson. Time-dependent calculations using with applications to unsteady flows past airfoils and wings. *AIAA Paper 91-1596*, 1991.

[32] A. Jameson, W. Schmidt, and E. Turkel. Numerical solution of the euler equations by finite volume methods using runge-kutta time stepping schemes. *AIAA Paper 81-1259*, 1981.

[33] P. Justesen. A numerical study of oscillating flow around a circular cylinder. *Journal of Fluid Mechanics*, 222:157–196, 1991.

[34] Y. Kallinderis. A 3-D Finite-Volume method for the Navier-Stokes equations with adaptive hybrid grids. *Applied Numerical Mathematics*, 20:387–406, 1996.

[35] Y. Kallinderis, A. Khawaja, and H. McMorris. Hybrid prismatic/tetrahedral grid generation for viscous flows around complex geometries. *AIAA Journal*, 34:291–298, 1996.

[36] Y. Kallinderis and S. Ward. Prismatic grid generation for 3-d complex geometries. *AIAA Journal*, 31:1850–1856, 1993.

[37] G. Karypis and V. Kumar. *METIS: A software Package for Partitioning Unstructured Graphs, Partitioning Meshes, and Computing Fill-Reducing Orderings of Sparse Matrices, Version 4.0.* Department of Computer Science, University of Minnesota, 1998.

[38] S. Kim. *Reynolds-Averaged Navier-Stokes Computation of Tip Clearabce Flow in a Compressor Cascade Using an Unstructured Grid.* PhD thesis, Virginia Polytechnic Institute and State University, 2001.

[39] B. Koobus and C. Farhat. Second-order time-accurate and geometrically conservative implicit schemes for flow computations on unstructured dynamic meshes. *Computer Methods in Applied Mechanics and Engineering*, 170:103–129, 1999.

[40] J. D. Lambert. *Numerical Methods for Ordinary Differential Systems : The Initial Value Problem.* John Wiley & Sons, 1991.

[41] M. Lesoinne and C. Farhat. Geometric conservation laws for flow problems with moving boundaries and deformable meshes, and their impact on aeroelastic computations. *Computer Methods in Applied Mechanics and Engineering*, 134:71–90, 1996.

[42] P.T. Lin. *Two-dimensional implicit time dependent calculation for incompressilbe flows on adaptive unstructured meshes.* PhD thesis, Princeton University, 2001.

[43] Rainald Löhner. *Applied CFD Techniques: An Introduction Based on Finite Element Methods.* John Wiley & Sons, 2001.

[44] A. G. Malan, R. W. Lewis, and P. Nithiarasu. An improved unsteady, unstructured, artificial compressibility, finite volume scheme for viscous incompressbile flows: Part i. theory and implementation. *Internal Journal for Numerical Methods in Engineering*, 54:697–714, 2002.

[45] A. G. Malan, R. W. Lewis, and P. Nithiarasu. An improved unsteady, unstructured, artificial compressibility, finite volume scheme for viscous incompressbile flows: Part ii. application. *Internal Journal for Numerical Methods in Engineering*, 54:715–729, 2002.

[46] L. Martinelli. *Calculation of Viscous Flows with a Multigrid Method.* PhD thesis, Princeton University, 1987.

[47] D. J. Mavriplis. Unstructured grid techniques. *Annual Review of Fluid Mechanics*, 29:473–514, 1997.

[48] D. J. Mavriplis. Viscous flow analysis using a parallel unstructured multigrid solver. *AIAA Journal*, 38:2067–2076, 2000.

[49] N. D. Melson, M. D. Sanetrik, and H. L. Atkins. Time-accurate Navier-Stokes calculations with multigrid acceleration. In *6th Copper Mountain Conference on Multigrid Methods*, page 423, 1981.

[50] Richard Mercier. Ocean turbulence loads and effects on offshore structures. Technical report, Offshore Technology Research Center, Texas A&M University and the University of Texas at Austin, 2004.

[51] T. Minyard and Y. Kallinderis. Octree partitioning of hybrid grids for parallel adaptive viscous flow simulations. *Internaltional Journal for Numerical Methods in Fluids*, 26:57–78, 1998.

[52] T. Minyard and Y. Kallinderis. Parallel load balancing for dynamic execution environments. *Comput. Methods Appl. Mech. Engrg.*, 189:1295–1309, 2000.

[53] T. K. Minyard. *A parallel adaptive Navier-Stokes method for hybrid grids with dynamic load balancing.* PhD thesis, The University of Texas at Austin, 1999.

[54] Y. Nakamura and Y. Tomonari. The effects of surface roughness on the flow past circular cylinders at high reynolds numbers. *Journal of Fluid Mechanics*, 123:363–378, 1982.

[55] David J. Newman and George Em Karniadakis. A direct numerical simulation study of flow past a freely vibrating cable. *Journal of Fluid Mechanics*, 344:95–136, 1997.

[56] P. Nithiarasu. An efficient artificial compressibility (ac) scheme based on the characteristic based split (cbs) method for incompressible flows. *Internal Journal for Numerical Methods in Engineering*, 56:1815–1845, 2003.

[57] G.A. Osswald, K.N. Ghia, and U. Ghia. A direct algorithm for solution of incompressible three-dimensional unsteady Navier-Stokes equaitons. *AIAA Paper 87-1139*, 1987.

[58] Peter Pacheco. *Parallel Programming with MPI.* Morgan Kaufmann, 1996.

[59] V. Parthasarathy. *Finite volume, adaptive-multigrid methods for Euler and Navier-Stokes equations on three-dimensional unstructured grids.* PhD thesis, The University of Texas at Austin, 1999.

[60] S.V. Patankar and D.B. Spalding. A calculation procedure for heat, mass and momentum transfer in three-dimensional parabolic flows. *Internal journal of heat and mass transfer*, 15:1787–1806, 1972.

[61] Charles S. Peskin. The immersed boundary method. *Acta Numerica*, 11:479–517, 2002.

[62] C.S. Peskin. Numerical analysis of blood flow in the heart. *Journal of Computational Physics*, 25:220–252, 1977.

[63] R. Peyret. Unsteady evolution of a horizontal jet in a stratified fluid. *Journal of Fluid Mechanics*, 78:49–63, 1976.

[64] S. Pirzadeh. Three-dimensional unstructured viscous grid by the advancing-layers method. *AIAA Journal*, 34:43–49, 1996.

[65] Stephen B. Pope. *Turbulent Flows.* Cambridge University Press, 2000.

[66] William H. Press, Brian P. Flannery, Saul A. Teukolsky, and William T. Vetterling. *Numerical Recipes in C : The Art of Scientific Computing.* Cambridge University Press, 1992.

[67] E.F. Relf. Discussion of results of measurements of the resistance of wires,with some additional tests on the resistance of wires of small diameter. Technical Report 102, The advisory committee for aeronautics, 1915.

[68] A. Rizzi and L.-E. Eriksson. Computation of inviscid incompressible flow with rotation. *Journal of Fluid Mechanics*, 153:275–312, 1985.

[69] P. L. Roe. Approximate riemann solvers, parameter vectors and difference schemes. *Journal of Computational Physics*, 43:357–372, 1981.

[70] P. L. Roe. Characteristic-based schemes for the euler equations. *Annual Review of Fluid Mechanics*, 18:337–365, 1986.

[71] S. E. Rogers and D. Kwak. An upwind differencing scheme for the incompressible Navier-Stokes equations. *Applied Numerical Mathematics*, 8:43–64, 1988.

[72] S. E. Rogers and D. Kwak. Upwind differencing scheme for the time-accurate incompressible Navier-Stokes equations. *AIAA Journal*, 28:253–262, 1990.

[73] S. E. Rogers, D. Kwak, and C. Kiris. Steady and unsteady solutions of the incompressible Navier-Stokes equations. *AIAA Journal*, 29:603–610, 1991.

[74] A. Roshko. Experiments on the flow past a circular cylinder at very high reynolds number. *Journal of Fluid Mechanics*, 10:345–356, 1961.

[75] A. Rubel and G. Volpe. Biharmonic vector stream function formulation and multigrid solution for a three-dimensional driven-cavity stokes flow. *AIAA Paper 89-1968-CP*, 1989.

[76] D. Kwak S. E. Rogers and U. Kaul. On the accuracy of the pseudocompressibility method in solving the incompressible Navier-Stokes equations. *Applied Mathematics and Modelling*, 11:35–44, 1991.

[77] Rolf H. Sabersky, Allan J. Acousta, and Edward Hauptman. *Fluid Flow: A First Course in Fluid Mechanics.* Prentice Hall, 1998.

[78] K. W. Schulz. *Numerical prediction of the hydrodynamic loads and motions of offshore structures.* PhD thesis, The University of Texas at Austin, 1999.

[79] K. W. Schulz and Y. Kallinderis. Unsteady flow structure interaction for incompressible flows using deformable hybrid grids. *Journal of Computational Physics*, 143:569–597, 1998.

[80] D. Sharov and K. Nakahashi. Hybrid prismatic/tetrahedral grid generation for viscous flow applications. *AIAA Journal*, 36:157–162, 1998.

[81] P. R. Spalart and S. R. Allmaras. A one-equation turbulence model for aerodynamic flows. *AIAA Paper 92-0439*, 1992.

[82] R. C. Swanson, R. Radespiel, and E. Turkel. On some numerical dissipation schemes. *Journal of computational physics*, 147:518–544, 1998.

[83] R. C. Swanson and E. Turkel. On central-difference and upwind schemes. *Journal of computational physics*, 101:292–306, 1992.

[84] C. H. Tai and Y. Zhao. Parallel unsteady incompressible viscous flow computations using an unstructured multigrid method. *Journal of Computational Physics*, 192:277–311, 2003.

[85] L. K. Taylor and D. L. Whitfield. Unsteady three-dimensional incompressible euler and Navier-Stokes solver for stationay and dynamic grids. *AIAA*, 92:–1650, 1991.

[86] T.E. Tezduyar, M. Behr, and J. Liou. A new strategy for finite element computations involving moving boundaries and interfaces - the deforming-spatial-domain/space-time procedure: I. the concept and the preliminary numerical tests. *Computer Methods in Applied Mechanics and Engineering*, 94:339–351, 1992.

[87] T.E. Tezduyar, M. Behr, S. Mittal, and J. Liou. A new strategy for finite element computations involving moving boundaries and interfaces - the deforming-spatial-domain/space-time procedure: Ii. computation of free-surface flows, two-liquid flows, and flows with drifiting cylinders. *Computer Methods in Applied Mechanics and Engineering*, 94:353–371, 1992.

[88] P.D. Thomas and K. Lombard. Conservation law and its application to flow computations on moving grids. *AIAA Journal*, 17:1030–1037, 1979.

[89] Joe F. Thompson, B. K. Soni, and N. P. Weatherill. *Handbook of Grid Generation*. CRC Press, Boca Raton, Florida, 1999.

[90] H. Tokunaga, K. Yoyeda, and N. Satofuka. Direct simulations of three dimensional flows using generalized vector potentional method. *AIAA Paper 91-1610-CP*, 1991.

[91] E. Turkel. Preconditioned method for solving the incompressible and low speed compressible equations. *Journal of Computational Physics*, 72:277–298, 1987.

[92] E. Turkel. A review of preconditioning methods for fluid dynamics. *Applied Numerical Mathematics*, 12:257–284, 1993.

[93] E. Turkel. *Chapter 13. Preconditioning and the Limit of the Compressible to the Incompresible Flow Equations for Finite Difference Schemes in the Frontiers of the Computational Fluid Dynamics 1994.* John Wiley & Sons, 1998.

[94] E. Turkel. Preconditioning techniques in computational fluid dynamics. *Annual Review of Fluid Mechanics*, 31:385–416, 1999.

[95] B. van Leer, C.-H. Tai, and K. G. Powell. Design of optimally smoothing multi-stage schemes for the euler equations. *AIAA Paper 89-1933*, 1989.

[96] J.K. Vandiver. Dimensionless parameters important to the prediction of vortex-induced vibration of long, flexible cylinders in ocean currents. journal of fluids and structures. *Journal of Fluids and Structures*, 7:423–455, 1993.

[97] C. H. K. Williamson. Defining a universal and continuous strouhalreynolds number relationship for the laminar vortex shedding of a circular cylinder. *Physics of Fluids*, 31:2742–2744, 1988.

[98] T.Y. Yang. *Finite Element Structural Analysis.* Prentice-Hall, 1986.

[99] L. T. Zhang, A. Gerstenberger, X. Wang, and W. K. Liu. Immersed finite element method, computer methods in applied mechanics and engineering. *Computer Methods in Applied Mechanics and Engineering*, 193:2051–2067, 2004.

Vita

Hyung Taek Ahn was born on December 28, 1973 in Kyungnam, Korea to Young Ok Ahn and Tae Hwa Noh. He received Bachelor of Engineering degree in mechanical engineering from Yeungnam University, Korea in February 1996, and Master of Science degree in mechanical engineering from Korea Advanced Institute of Science and Technology (KAIST), Korea in February 1999. He worked for Samsung Display Instruments in Suwon, Korea as a research engineer from January 1999 to June 1999. He started his doctoral program in aerospace engineering at the University of Texas at Austin in the fall semester of 1999. He received Rotary Foundation Ambassadorial Scholarship for the academic years of 1999-2002.

Permanent Address: Narea-maul 812-703
Dowon-dong, Dalso-gu
Daegu, Korea 704-793

This dissertation was typeset with LaTeX 2_ε[1] by the author.

---

[1] LaTeX 2_ε is an extension of LaTeX. LaTeX is a collection of macros for TeX. TeX is a trademark of the American Mathematical Society. The macros used in formatting this dissertation were written by Dinesh Das, Department of Computer Sciences, The University of Texas at Austin, and extended by Bert Kay and James A. Bednar.